Monometallic Ni and Bimetallic Pt-Ni Nanocatalysts by Supercritical Deposition

by

Ramazan Oğuz CANIAZ

A Thesis Submitted to the

Graduate School of Engineering

in Partial Fulfillment of the Requirements for

the Degree of

Master of Science

in

Chemical and Biological Engineering

Koç University

August, 2012

Koc University

Graduate School of Sciences and Engineering

This is to certify that I have examined this copy of a master's thesis by

Ramazan Oğuz CANIAZ

and have found that it is complete and satisfactory in all respects,

and that any and all revisions required by the final

examining committee have been made.

Committee Members:

Can ERKEY(Advisor)

Yaman ARKUN

Mehmet SOMER

Date: 07/08/2011

to my mother…

ABSTRACT

Monometallic nickel and bimetallic platinum-nickel nanoparticles were deposited on γ-Al_2O_3, Vulcan XC72R and carbon aerogel (CA) supports by supercritical carbon dioxide ($scCO_2$) deposition (SCD). Characterization of the samples was carried out by BET, TPD, XRD, TEM, and EDXS. Nickel acetylacetonate ($Ni(acac)_2$) was adsorbed on the supports from $scCO_2$ solutions. The adsorbed Ni precursor was reduced to nickel nanoparticles by heat treatment under hydrogen. The resulting nanoparticles had an average size of 6 nm. Bimetallic Pt-Ni nanoparticles were synthesized by a two-step procedure termed sequential deposition. First, Pt nanoparticles were deposited on the supports by adsorption of platinum cyclooctadiene dimethyl $Pt(cod)(me)_2$ from $scCO_2$ solution followed by reduction of the adsorbed precursor to Pt by heat treatment at 200 ^oC under flowing nitrogen. Subsequently, $Ni(acac)_2$ was adsorbed on Pt/support from $scCO_2$. The adsorbed Ni precursor was then reduced to Ni by heat treatment under hydrogen. Spherical nanoalloys of Pt-Ni nanoparticles with uniform sizes of ~3nm were obtained over Vulcan XC 72R, and Pt-Ni nanoparticles with uniform sizes of ~1nm were successfully synthesized over carbon aerogel. As for the alumina support, supported Pt-Ni nanoparticles of ~3 nm in size were obtained. The small composition variations in EDXS measurements indicated a uniform distribution of the bimetallic nanoparticles. The effect of the order of sequential deposition of Pt and Ni on both morphology and activity of the synthesized materials were also investigated. It was found that the formation of Ni nanoparticles occurs on the previously deposited Pt islands resulting in bimetallic spherical nanoparticles having homogeneous chemical compositions with no phase separation when Pt deposition is carried out first and this is followed by Ni deposition. Interestingly, the size of the bimetallic nanoparticles was found to be smaller than the size of the monometallic Ni. However, pure Ni agglomerates were observed on TEM images when Ni deposition is achieved first and this was followed by Pt addition. Cyclic voltammograms of the carbon supported catalysts were also determined. Bimetallic nanocatalysts showed a higher activity than the monometallic nanocatalysts. Among the bimetallic nanocatalysts, higher activity was obtained when Pt deposition was carried out first.

ÖZET

Tek başına nikel ve de çift-metalli platin-nikel nano parçacıkları γ-Al_2O_3, Vulcan XC72R ve karbon aero-jel (KA) destek malzemelerinin üzerinde süper kritik karbondioksit ($scCO_2$) depozisyonu (SCD) yöntemi ile sentezlenmiştir. Sentezlenen malzemelerin karakterizasyonu Nitrojen Fizisorpsiyon (BET), Sıcaklık Programlı Desorpsiyon (TPD), X-Işını Difraksiyon Spektroskopisi (XRD), Geçirgenli Elektron Mikraskopu (TEM) ve Enerji Dağılımlı X-Işını Spektroskopisi (EDXS) teknikleri ile yapılmıştır. Süper kritik karbon dioksit içinde çözünmüş nikel asetilasetonat ($Ni(acac)_2$) destek malzemesi üzerine adorplanmıştır. Adsorplanmış Ni öncü malzemesi olan ($Ni(acac)_2$) hidrojen akışı altında ısıl işlemler ile Ni nanoparçacıklarına dönüştürülmüştür. Elde edilen nanoparçacıkların boyutlarının ortalama 6 nm oldukları gözlenmiştir. Çift-metalli Pt-Ni nanoparçacıklarının sentezlenmesinde sıralı depozisyon adı verilen iki-adımlı bir teknik kullanılmıştır. Öncelikle, Pt metal öncü malzemesi olan platin siklo-oktadiyen-dimetil $Pt(cod)(me)_2$ çözünmüş halde bulunduğu $scCO_2$ ortamından destek malzemesi yüzeyine adsorplanır ve devamında 200 ^{o}C'de azot gazı akışı altında Pt nano parçacıklarına çevrilir. Ardından, ($Ni(acac)_2$) metal öncü malzemesi Pt/destek malzemesi üzerine adsorplanır. Adsorplanan ($Ni(acac)_2$) devamında hidrojen gazı altındaki ısıl işlemler ile Ni metaline indirgenir. Bu işlemler sonrası, Vulcan XC72R üzerinde ~3 nm büyüklüğünde küresel Pt-Ni nanoparçacıkları; KA üzerinde parçacık boyut dağılımı ~1nm civarında Pt-Ni nanoparçacıkları; γ-Al_2O_3 üzerinde ise parçacık dağılımı gene ~3nm civarında çift-metalli Pt-Ni nanoparçacıkları elde edilmiştir. EDXS ölçümlerinde gözlemlenen kompozisyonların bölgelere göre sadece küçük değişimler göstermesi çift-metalli nano parçacıkların düzenli ve homojen bir dağılıma sahip olduğuna işaret etmektedir. İki-adımlı depozisyon tekniğinde metal yüklenmesi sırasının sentezlenen malzemelerin morfoloji ve aktivitesine olan etkileri de çalışılmıştır. Bulgular göstermektedir ki, daha sonra yüklenen Ni metalinin nanoparçacıkları, önceden depozit edilmiş Pt adacıklarının üzerinde oluşmuştur. Böylece kimyasal kompozisyonu değişiklik göstermeyen, faz ayrımı sergilemeyen çift-metalli Pt-Ni nanoparçacıkları sentezlenmiştir. İlgi çekici bir şekilde, çift-metalli nanoparçacıkların boyutlarının tek metalli nikelden daha küçük olduğu gözlenmiştir. Ancak, depozisyon sırası Ni öncelikli olarak değiştirildiğinde, çift-metalli Pt-Ni nanoparçacıkları yerine saf Ni topaklanmaları TEM resimlerinde gözlenmiştir. Karbon destek malzemesi ile sentezlenen katalizörlerin döngüsel voltametre (Cyclic Voltammetry - CV) ölçümleri yapılmıştır. Çift-metalli katalizörlerin tekli olanlara göre daha yüksek aktivite gösterdiği gözlenmiştir.

Çiftmetalli katalizörler arasında ise, Pt depozisyonunun önce yapılmasının aktiviteyi arttırdığı saptanmıştır.

ACKNOWLEDGEMENTS

With all respect and gratitude, I would like to express my sincere thanks to my advisor, Prof. Dr. Can ERKEY whose guidance, encouraging support and patience throughout my graduate study helped me to complete this thesis. Certainly, it was a great pleasure to be a part of his research group. He has invaluable contributions to my both educational and working career. I will always remember him with his honesty and kindness. I would like to extend my grateful thanks to Prof. Dr. Yaman ARKUN and Prof. Dr. Mehmet SOMER for their participation in my thesis committee.

Also, I would like to thank my colleague Selmi Erim Bozbağ for his quidance throughout my studies, and also to my other colleagues Zeynep Ülker, Deniz Şanlı, Sezin Nargül, İbrahim Şahin, Metin Karayılan and to my former colleagues Seda Giray, Nil Ezgi Dinçer, Erdal Uzunlar. I would like to give my special thanks to my housemates İhsan Ozan Yıldırım and Ömer An, without their endless friendship the graduate study years could not be this much enjoyable.

I would like to thank Turkish Petroleum Refineries Corporation (TÜPRAŞ) Directorship support, especially to Murat YILDIRIM, the manager of R&D Department. I owe a great many thanks to Yeşim Köprülü, Ersen Ertaş and Meriç Kartal.

Last, I would like to thank my family. I always feel their support, encouragement and great love. Another special thanks goes to Betül İpek for her love and friendship from the time she is in my life. I love you so much.

TABLE OF CONTENT

LIST OF TABLES

LIST OF FIGURES

NOMENCLATURE

CA: Carbon Aerogel
$scCO_2$: Supercritical Carbon Dioxide
SCD: Supercritical Carbon Dioxide Deposition
BET: Brunauer Emmett Teller
TPD: Temperature Programmed Desorption
XRD: X-ray Diffraction
TEM: Transmisson Electron Microscopy
EDXS: Energy Dispersive X-ray Spectroscopy
$Ni(acac)_2$: Nickel Acetyl Acetonate
$Pt(cod)(me)_2$: Platinum Cyclooctadiene DiMethyl
CV: Cyclic Voltammetry
SCF: Supercritical Fluid
ORR: Oxygen Reduction Reaction
rpm: Revolution Per Minute
HOR: Hydrogen Oxidation Reactions

1. INTRODUCTION

Supported monometallic Ni and bimetallic Pt-Ni catalysts are known to catalyze a wide variety of reactions. For example, γ-alumina supported Ni nanoparticles are used extensively for reforming, γ-alumina supported bimetallic PtNi nanoparticles are used for reforming, hydrogenation and hydroisomerization, and carbon supported bimetallic PtNi are promising candidates for oxidation and reduction reactions in fuel cells.

The development of fuel cells is attracting a great deal of interest as a green energy resource during the last decades, because of the rapid depletion of fossil fuels, degradation of the environment, and the effects of the air pollution on human health. Most of the pollution is caused by the extensive use of internal combustion engines. Hydrogen, on the other hand, is an efficient fuel and emits no green house gases directly. At present, the problems encountered in the development of fuel cells are durability under operating conditions, low activity, and high cost of catalysts

The size, shape, size distribution, loading, and impregnation sequence are important to tune the durability, activity and selectivity of the synthesized catalysts and these parameters depend on the preparation techniques. As compared to the techniques such as wet / dry impregnation, co-precipitation, and sol-gel, SCD is a relatively new technique for the preparation of supported metal nanoparticles [1]. A SCF has properties intermediate between a liquid and a gas. It is capable of dissolving solutes like a liquid and exhibits almost no surface tension with low viscosity that enables the good penetration of the dissolved molecules into the small pores. The liquid solvents usually are not favorable for the wetting of very small pores which results in low utilization of the support for metal deposition Another advantage of a SCF is the sensitivity of its density to the changes in temperature and pressure which makes it possible to manipulate the solvent properties during processing

In addition to the metal pairs deposited and the deposition techniques employed, the support material also has a notable influence on the activity of the catalysts [2-4] Pore size, pore volume, surface area, acidity and conductivity are the key factors that determine the effect of the support on the activity and selectivity of the catalyst.

In this study, SCD was used to synthesize supported monometallic Ni and bimetallic Pt-Ni nanoparticles. Commercially available supports of γ-alumina and Vulcan XC72R as well as carbon aerogels prepared in our laboratory were used as supports. Bimetallic nanoparticles were synthesized by the technique called sequential deposition. The effects of support, metal loading, impregnation and reduction conditions on the particle size, particle size distribution and activity were investigated.

Primarily, in Chapter 2, brief overview about the acidic and carbon based porous supports for catalysis is given followed by the importance of bimetallic nanocatalysts as compared to the monometallic ones. The comparative literature information is provided on SCFD for supported bimetallic nanoparticles and on the characterization techniques for the morphology and activity of the nanocatalysts. Afterwards, experimental details of the study is given in Chapter 3 including the support characterization, metal impregnation, nanoparticle characterization and activity tests. The corresponding results and all possible discussion that can be extracted out of these results are presented in Chapter 4. The last chapter summarizes the work done and the achievements of this study.

2. LITERATURE REVIEW

2.1. Catalyst Supports: Carbon Supports, Solid Acidic Supports, and Aerogels

Varieties of supports are used in catalysis, since the support material has a notable influence on the activity of the catalyst. Pore size, surface area, acidity and conductivity are the key factors that determine the effect of the support on the activity of the catalyst [2-4]. Briefly, the function of the support can be explained by mainly two reasons. Firstly, they may contribute to the overall reaction mechanism and secondly, they can increase the dispersion of the metals deposited over the support surface. Most common examples for the first function are the carbon supports in fuel cell applications to conduct electrons [4] or the solid acidic supports in hydrogenation [5], reforming [6] and hydrocracking [7] reactions to crack C-C bonds. As for the second function of a support, it increases the metal dispersion by the help of its high surface area per gram value. While the supports like alumina, silica and silica-alumina has, typically, surface area values over 200 m2/g [8], the carbon aerogels on the other hand can provide surface area values ranging between 350 - 1000 m^2/g[9]. The high surface area provides more available sites for metal deposition and thereby more available sites for the reactants to adsorb on, react, and subsequently desorb from.

In fuel cell applications, the reactions happening on the anode site produce the electrons and these electrons are needed for the reactions happening on the cathode site. The transfer of the electrons is achieved by an external circuit and when certain amount of electron is passed through a wire with a certain resistivity, an electricity is produced which is the main objective in fuel cell operations [10]. If a support which cannot conduct electrons is used, then the transfer of the electrons from metal/support composite to external circuit would not be achieved. This is the reason why a carbon support should be used in fuel cell applications as a catalysts support in addition to its use as a part of the structure in the fuel cell system like gas diffusion layer [11].

Different types of carbon supports have been widely used in industry [12]. Carbon Black [13], Carbon Fiber [13], CNT [13-15], Activated Carbon [4], and Vulcan XC-72R [16-18] are only some of them.

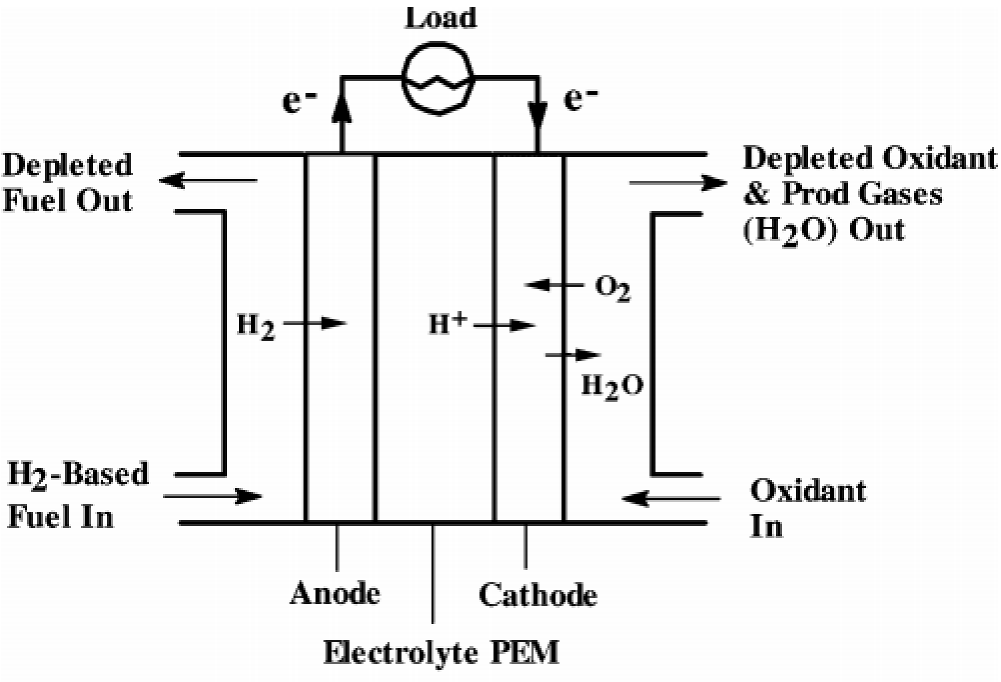

Figure 2.1: The figure shows the working principles of proton exchange membrane fuel cell, *taken from* [19].

As for the solid acidic supports used in catalysis, the important property of a support is its acidity. The acidic sites on the support are the active sites for the cleavage of C-C bonds. Therefore, the cracking strength of a catalyst is directly related with the acidity of its support and the product distribution of the reactions happening over the catalyst surface is influenced accordingly [20]. In steam methane reforming (SMR) reactions, for example, high acidity is not desired because broking C-C bonds does not require severe acidity [21]. In hydrocracking reactions, on the other hand, long-heavy polymeric chains (hydrocarbons) are the reactants and in order to crack these hydrocarbons into smaller and more valuable fractions, severe acidity is of desire. For this reason, different types of zeolites with high acidities such as Y-type, de-aluminated y-type, beta-type, ultra stable beta (USB) type are preferred [22-26]. However, if the related sites on the support are too acidic, then the desorption of the corresponding products will not be achieved and the overall reaction will be retarded. It is found in the literature that the blends of different types of zeolites together with γ-alumina can be a better support depending on the applications [22]. In addition to the acidity, another important parameter for the reactions using solid supports is the minimum size and shape of the support material depending on the geometry of the reactor. This is known as wall effect and it greatly influences the flow regime [27, 28].

One of the new classes of the supports in catalysis is the aerogels. They were discovered first around 1930s as silica aerogels [29, 30] and Pekala's group developed the sol-gel route further for the preparation of carbon aerogels [31]. The silica aerogels have been generally considered as thermally good insulative materials and later on their use as catalyst support was considered [32]. Carbon aerogels on the other hand are electro conductive materials and can be used for fuel cell applications [33-36]

There are a lot of supports with varying chemical and physical properties together with different advantages and drawbacks and more will be in the market in the near future. Therefore, the proper support is to be chosen by considering the specific application, desired product distribution and resistivity against the mild conditions of the reactions to be studied.

2.2. Importance of Bimetallic Supported Metals in Catalysis: Promotion Effect

It has been known that bimetallic catalysts possess improved catalytic activities and selectivities that are far from their corresponding monometallic ones. This ability of tuning the catalytic performance is known as promotion effect in which the second metal (the promoter) helps the first one in hindering the overall reactions. In the literature, promotion effect is related to the modifications in the electronic and chemical properties of the metals when they are coupled / alloyed. These modifications are explained by two possible mechanisms. First interpretation is the formation of new bonds resulting in a change in the electronic environment of the metal surface. Second interpretation draws the attention to the changes in the geometry of the available sites upon coupling / alloying. Both of those modifications in either electronic or geometric structure of the active sites give rise to a higher activity due to the changes in the adsorption energies of the reactant and products or due to the prevention of the side reactions [17, 37, 38]

Widely studied example in the understanding of the promotional effect is the Pt-Ru pair. In the literature, the promotion effect of Ru is explained by either electronic effect which weakens the Pt-CO bond and thereby hinders the removal of CO, or by so called bifunctional effect. According to the bifunctional mechanism, Ru provides oxygen containing species which oxidize CO to form CO_2. Then, these CO_2 molecules readily desorbs from the surface which is the rate determining step in the overall reaction [38-40].

$$Ru + H_2O \rightarrow Ru\text{-}OH + H^+ + e^- \tag{1}$$

$$Ru\text{-}OH + Pt\text{-}CO \rightarrow Ru + Pt + CO2 + H^+ + e- \tag{2}$$

The remaining question is whether alloys are required for this electronic and chemical altering or the promoter which is in proximity of the first metal is enough. And a clear explanation for being in the ‘proximity’ is needed. It might mean that the metals are deposited as separate islands and slight phase segregation is occurred with still some contact between, say, Pt and Ni islands. Or, depending on the temperature values studied and compositions of the metals, nanoalloys may occur with a certain degree of alloying. Alternatively, core-shell structures may form, as can be seen from Figure 2.2.

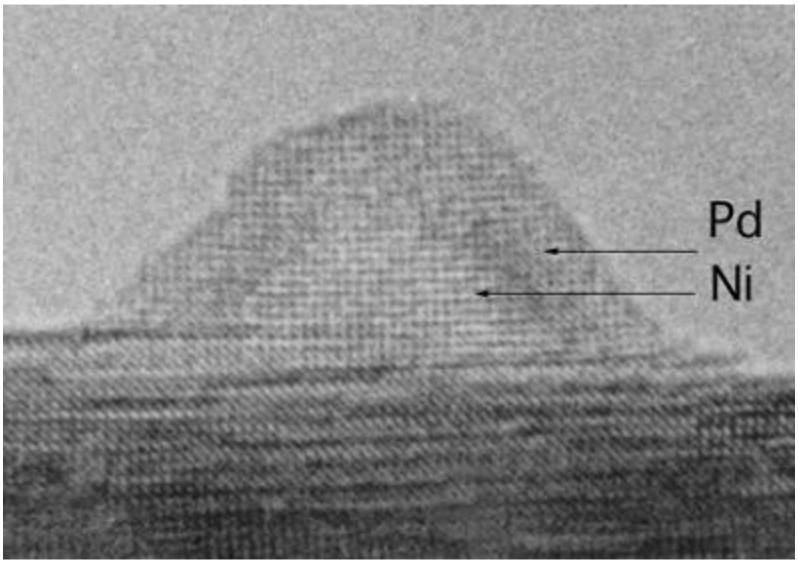

Figure 2.2: HRTEM image of a supported $Ni_{core}Pd_{shell}$ cluster, *taken from* [41].

It is also possible that this core-shell structure may cease the dissolution of the noble metal in fuel cell applications if noble metal, say platinum, is in the core and surrounded by the catalytically less active and less stable non-noble metal, say Ni. But, since shell of Ni blocks the Pt-core, the oxygen reduction reaction would be retarded severely in this configuration. Some studies, on the other hand, suggest that Pt-Ni core-shell structures with Pt-rich shell are better from an economical point of view since Pt segregates on to the surface of cheap Ni resulting in a higher ESA by using less amount of Pt.[42]. Recently, Zhong and co-workers prepared Ni subsurface layer surrounded by Pt rich surface. The Ni subsurface was reported to determine the electronic properties of the surface, leading to a reduced coverage of adsorbing species, hydrogen, and OH, on $Pt_3Ni(111)$ compared to Pt(111) electrode. Regarding the necessity of a change in the electronic properties, at another study on Pt in which Ru was used as a promoter this time, it was shown that if Pt and Ru conserve their original and element specific properties then higher activity can be obtained. So, exhibiting an electronic change is not of desire for Pt-Ru pair, as they stated [43].

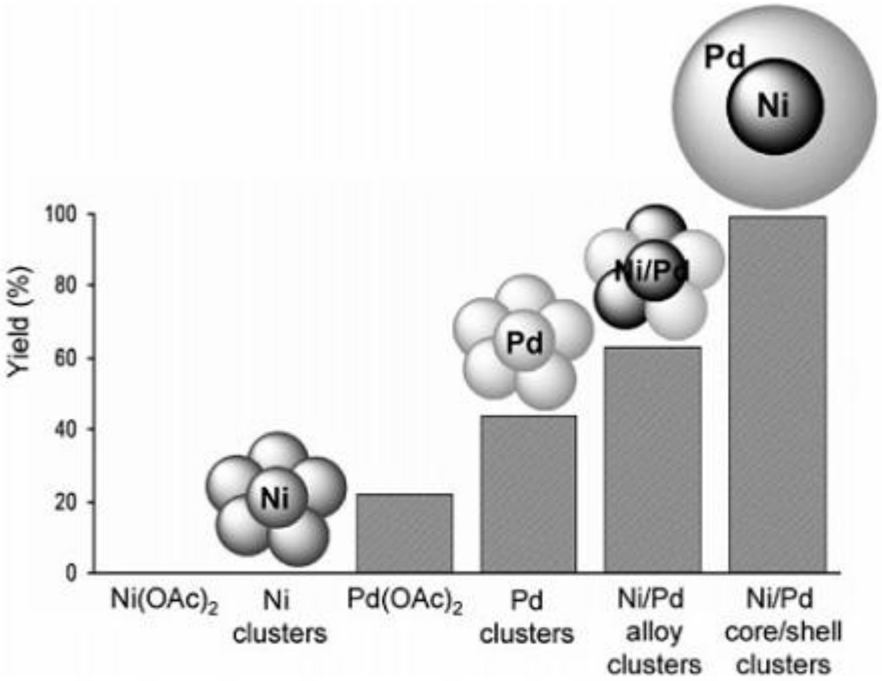

Figure 2.3: Comparison of the catalytic activity for six different systems in the Hiyama cross-coupling of iodotoluene and tri- methoxyphenylsilane: Ni(OAc)2, Ni clusters, Pd(OAc)2, NiPd alloy clusters, and NicorePdshell clusters, *taken from* [44].

As for the catalytic applications other than fuel cells, Rothenberg and co-workers studied the Hiyama cross coupling of phenyltrimethoxysilane and haloaryls reaction catalyzed by Ni clusters, Pd clusters, Ni-Pd alloys, and $Ni_{core}Pd_{shell}$ composites and they figured out that $Ni_{core}Pd_{shell}$ is the catalytically most active structure [44]. (See Figure 2.3.)

At another study, Pt-Ru bimetallic nanocomposites supported by multi-walled carbon nanotubes were synthesized together with Pt-Ni, Pt-Au, Pt-Pd, and Pt-Cu pairs. Based on the XRD diffractogram, only metal pair that does not form an alloy was Pt-Ru and it was again this pair which showed the highest activity in methanol oxidation suggesting that alloying is not a key issue in improving the activity and selectivity of the catalyst. (See Section 2.3, Figure 2.5) [15].

It can be deduced that different reactions catalyzed by varying bimetallic supported catalysts may require unique structures for the optimum activity. Therefore, more studies about understanding the dynamics of the formations of bimetallic structures and their effects in the catalytic applications are needed.

2.3. Supercritical Fluid Deposition for Supported Bimetallic Catalyst Preparation

The size distribution and the shape of the supported metal particles have a direct impact on the activity and selectivity of the synthesized catalysts. Also, minimizing the particle sizes is important from the economical point of view [45, 46]. When the size of the deposited particles decrease, the surface area of the metal particles is increased and this results in more active sites for the reaction and less amount of expensive nobel metal to be used. Therefore the catalysts preparation technique chosen is quite important both for technical and economical reasons. The techniques such as impregnation, co-precipitation, and sol-gel methods do not offer a complete control on shape, size and size distributions of the particles, on the other hand, supercritical fluid (SCF) deposition as a promising technique is more successful in controlling these key parameters. Uniform particle size distribution can be obtained by supercritical fluid deposition (SCFD) and the size of the particles can be controlled depending on the reduction conditions studied. [1, 46, 47]

During the last decades, SCF has been investigated deeply since it combines the properties of liquids and gases. It is capable of dissolving solutes like a liquid and exhibits almost no surface tension with low viscosity that enables the good penetration of the dissolved molecules via the small pores. The liquid solvents usually are not favorable for the wetting of these inaccessible pores. Another advantage of SCF is the sensitivity of its density to the changes in temperature and pressure which makes it possible to manipulate the solvent properties during processing. Among the other SCFs, supercritical carbon dioxide is found to be more attractive since it is cheap, non flammable, has low reactivity and low toxicity, and leaves no sign on the treated media [1, 47, 48].

Recently, SCFD technique has started to be used for the preparation of supported bimetallic nanoparticles. Deposition of the metal nanoparticles can be achieved by either simultaneous or sequential deposition techniques. In the simultaneous deposition technique, corresponding organometallic compounds are put together in to the vessel and after their dissolution in the supercritical fluid phase, adsorption of them over the support occurs simultaneously [14, 15]. As for the sequential deposition technique, the adsorption of single organometallic compound over the support can be carried out. After the reduction process, monometallic supported nanoparticles are used as a support for the adsorption of a second organometallic compound [49].

The reduction processes can be achieved by either thermally or chemically. Thermal reduction can be applied in SCF phase by increasing the temperature of the vessel. Another way for thermal reduction is to depressurize the vessel and expose the sample to nitrogen flow at atmospheric pressure at high temperatures. As for the chemical reduction, it can be done in SCF phase again, by injecting hydrogen to the vessel after adsorption of the organometallic compound, or alternatively the sample can be placed in a furnace and the temperature can be raised to the required level under hydrogen flow. The advantage of chemical reduction is the lower required reduction temperature that may decrease the amount of the precursor volatilized during reduction. On the other hand, particle sizes are observed to be high when chemical reduction is preferred [1, 50, 51].

The use of SCFD technique for the preparation of supported bimetallic nanoparticles is quite new. Preparation of Pt-Rh nanoparticles supported by mesoporous silica templates via multistep impregnation together with $scCO_2$ treatment was reported. Conventionally produced catalysts were treated by $scCO_2$ and higher activity and selectivity were observed for ethane production which was attributed to the central C–C bond scission [52]. At another study by Wakayama and co-workers, the technique called nanoscale casting under supercritical fluid was reported to be successful in synthesizing nano porous fibers of Pt-Ru[53]. Lin et al. [14] decorated carbon nanotubes (CNT) with platinum and ruthenium nanoparticles in $scCO_2$ with the addition of small amount of methanol as a modifier. $Pt(acac)_2$ and $Ru(acac)_2$ organometallic precursors, after simultaneous adsorption on to the supports, were converted to their metallic forms by in situ hydrogen reduction method. The PtRu nanoparticles (45:55 molar ratio) had the particle sizes in a range of 5-10 nm.

Recently, Erkey and his co-workers reported that supported PdPt bimetallic nanoparticles over Black Pearl 2000 (BP2000) have been successfully synthesized by sequential SCF deposition technique [49, 54]. It has been found that broad particle size distribution of monometallic Pd particles can be narrowed if Pt particles are deposited first and this is followed by sequential Pd deposition.

As for the Pt-Ni pair, Yen at al [15] prepared different platinum-based bimetallic nanoparticles including bimetallic Pt-Ni composites supported by multi-walled carbon nano tubes by simultaneous $scCO_2$ deposition technique. To enhance the low solubilities of the metal precursors, small amount of methanol was added as an entrainer. After binary adsorption of $Pt(acac)_2$ and $Ni(hfa)_2$, precursors were reduced to their metal form in the reaction vessel at 473 K with the addition of hydrogen. Obtained Pt-Ni particle sizes were around 6.6 nm±3.5 with an atomic ratio of 62:38 (See Figure 2.4). Based on the shift towards higher 2Θ angles in the XRD diffractogram, prepared bimetallic Pt-Ni were reported to have disordered alloy crystal structures (See Figure 2.5). The activity of the prepared catalysts was investigated by studying cyclic voltammograms of methanol oxidation. It was strange that only metal pair that was not formed an alloy was Pt-Ru pair with a mixture of both fcc and hcp. Asymmetric peaks were observed in corresponding XRD spectra. But, it was again this metal pair who showed the highest activity in the methanol oxidation. Pt-Ru pair provided the highest I_f/I_b where I_f is the forward scan peak current and I_b is the backward scan peak current.

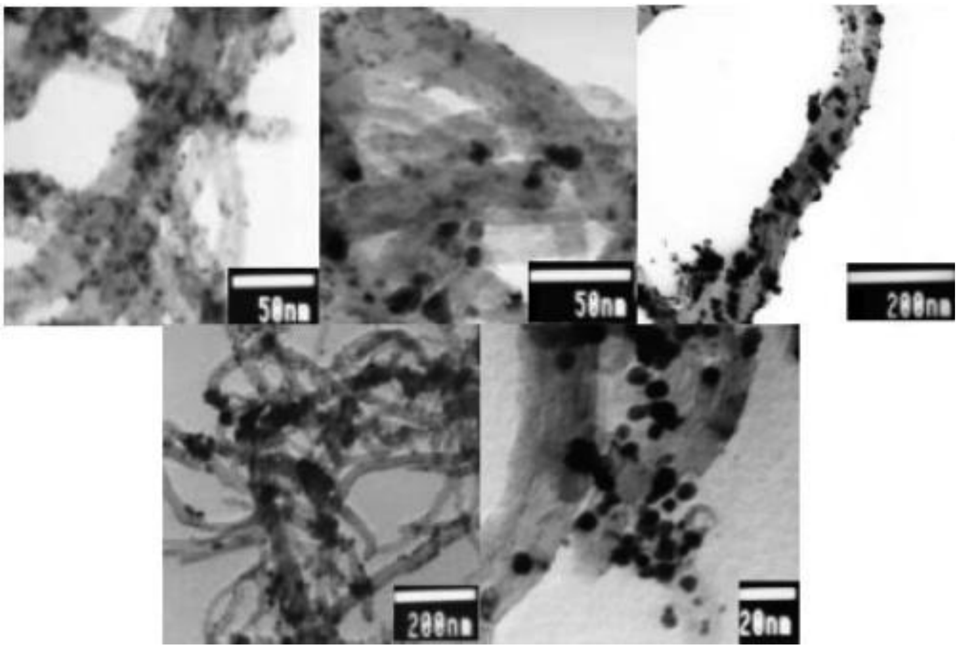

Figure 2.4: TEM of (a) Pt-Ru (top left), (b) Pt-Ni (top middle), (c)Pt-Au (top right), (d) Pt-Pd (bottom left), and (e) Pt-Cu (bottom right)[15] .

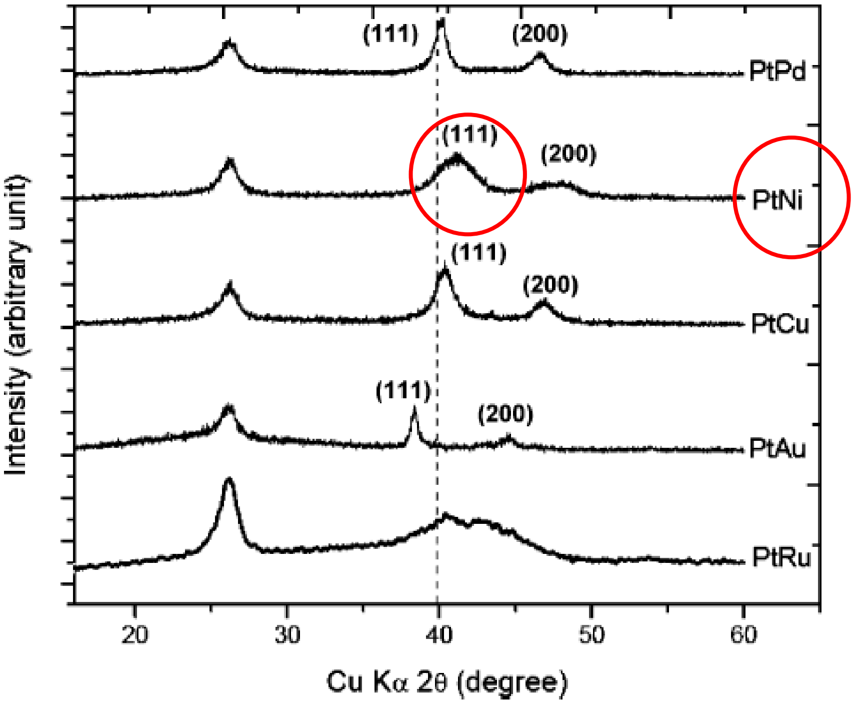

Figure 2.5: XRD patterns of the different bimetallic catalysts. The dotted line is the monometallic Pt (111) (2Θ) 39.8°) peak for reference, *taken from* [15].

However, regarding the success of SCFD, the results of the Yen's study are open to criticism. It is not clear either it is the methanol that dissolves the metal precursors before the system is charged with CO_2 or it is the $scCO_2$ whose solubility is tuned by the addition of an entrainer. If the methanol dissolves the precursor before the CO_2 is introduced to the system, then a classical impregnation would occur since there is not a filter bag or similar apparatus to separate the support material from the precursor and the methanol which is at the bottom of the deposition vessel. Also, Figure 2.4 (top middle) shows that deposition of Pt-Ni bimetallic composites did not result in a narrow particle size distribution. The reported average particle size of 6.6 nm shows a huge standard deviation of ±3.5. In this master thesis on the other hand, supported bimetallic Pt-Ni nanoparticles having quite narrow particle size distributions and with a size of 3nm, 1nm, and 3 nm were successfully synthesized over Vulcan XC 72R, CA and γ-alumina respectively.

2.4. Characterization Techniques for the Analysis of Bimetallic Nanoparticles & Nanoalloys

In the concepts of supported metals for catalysis, there are a lot of important parameters to be considered regarding the activity and selectivity of the prepared catalysts such as the chemical and physical properties of the support, size and shape of the deposited metals, introduction of the promoter(s), and the existence of the chemicals having a potential to poison the catalyst. As can be seen from Figure 2.6., when these structural parameters are combined with the kinetic effects, understanding the 'catalysis' at micro level becomes harder [55].

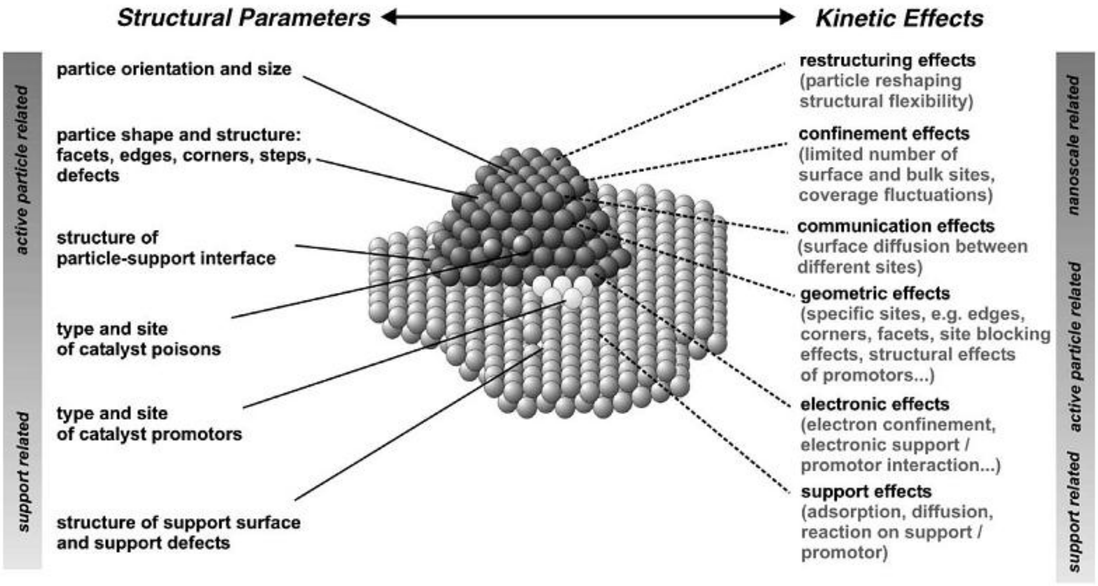

Figure 2.6: Structural parameters and kinetic effects on supported metal catalysts, *taken from* [55].

Even more complicated dynamics are found when nanoscale materials are produced. Luo and co-workers worked on AuPt system and found one of the first examples revealing the deviations of the physical and chemical properties of the nanoscale materials from the crystalline structure at bulk composition. Carbon supported AuPt composites with an average size of ~2nm were prepared by organic monolayer encapsulation. The synthesized bimetallic structures were characterized by XRD and alloy formation was confirmed by careful analysis of the Bragg peaks. The findings were contrary to the miscibility gap of bulk Au-Pt [56]. At another study, Nashner and co-workers prepared bimetallic Pt-Ru composites [57]. Characterization results showed that particles have a diameter of ~1.5 nm. The moleculer precursor with an atomic ratio of 1:5 Pt:Ru was used. For bulk alloys of Pt-Ru pair, above 0.62 Ru atomic fraction, an hexagonal-closest-packed (hcp) structure is expected. However, this nanoscale system resulted in an fcc structure, contrary to the expectations at bulk compositions. Another example illustrating the deviations from chemical and physical properties for the nanoscale materials as compared to their bulk compositions is given in Figure 2.7. These huge deviations can be explained by the properties of the surface atoms starting to dominate the properties, as the particle size gets smaller.

Melting Point → **bulk Au : 1337 K**

30 nm Au particle : 700 K

Curie Temperature → **bulk $BaTiO_3$: 403 K**

120 nm $BaTiO_3$ particle : 350 K

Figure 2.7: Physical and chemical properties of the nanoscale materials largely deviate from the properties of their bulk counterparts.

Therefore, to understand the structure and the corresponding effects of the structure on the activity and selectivity of the synthesized bimetallic nanocatalysts in varying reactions, numerous techniques have been invented and improved through the decades such as XRD, TEM, EDX, X-Ray Photoelectron Spectroscopy (XPS), X-ray Absorption Spectroscopy (XAS)-including X-ray Absorption Near Edge Structure (XANES) and Extended X-ray Absorption Fine Structure (EXAFS), and Cyclic Voltammetry (CV)[58].

How frequently the emphasized characterization techniques are used is displayed in Figure 2.8. In this section of the thesis, the basics of the catalysts characterization techniques will be discussed.

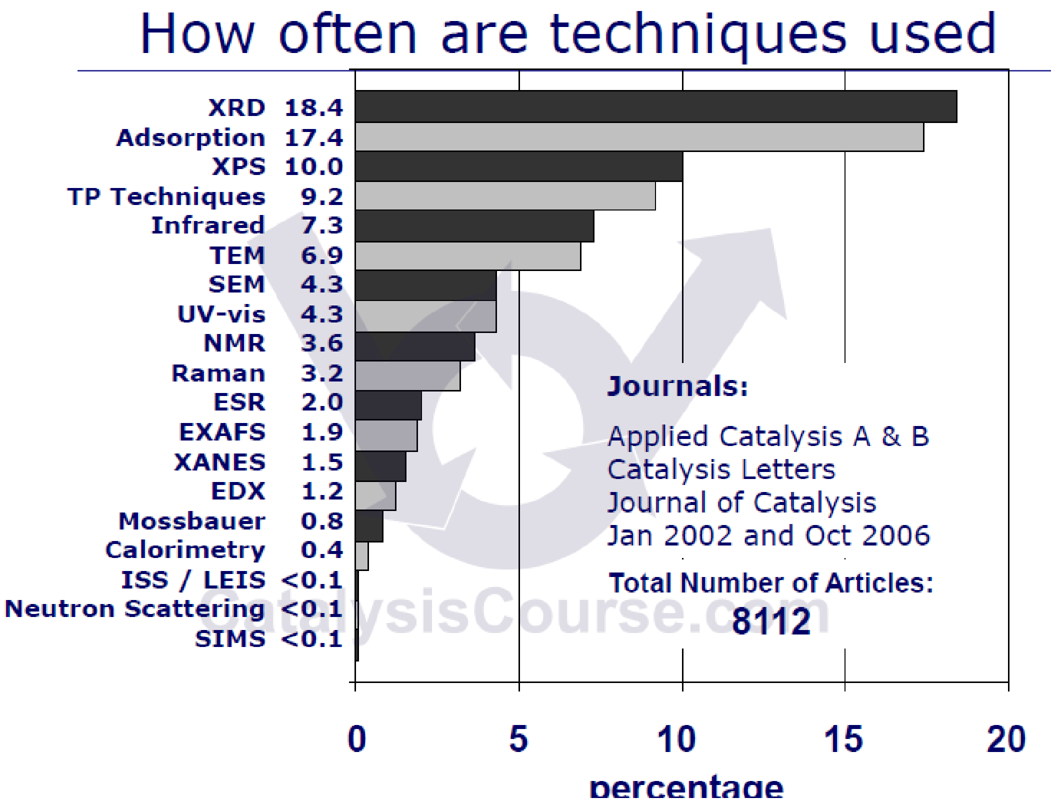

Figure 2.8: The percentage of studies in which the listed techniques were employed, out of 8112 papers published in Applied Catalysis A & B, Catalysis Letters, Journal of Catalysis during the period of Jan 2002 to Oct 2006, *taken from* [59].

One of the most widely used techniques applied for supported metals is XRD. If the metals are deposited over the porous catalyst with a certain crystalline structure, then the x-ray beam will be scattered from the surface at certain angles of incidence which can be seen in Figure 2.9. And what kind of a specific crystal metal structure occurred over the surface of the support can directly influence the activity and the selectivity of the prepared catalysts[58, 59]. By using the Bragg relation (2.1), one can estimate the lattice spacings and further analysis can be done by using Scherrer Equation (2.2) to estimate the size of the deposited metal particles.

$$n \cdot \lambda = 2 \cdot d \cdot \sin\Theta; \; n = 1,2, \ldots \qquad (2.1)$$

where λ stands for the wavelength of the X-rays, the distance between the lattice planes is expressed by *d*, Θ is the angle between the incoming X-rays and the normal to the reflecting lattice plane, and the order of reflection is designated by an integer n.

$$B = (0.9 \cdot \lambda)/(t \cdot Cos\Theta) \qquad (2.2)$$

where B is the particle size, λ is the X-ray wavelength which is 0.15406nm for CuK-alpha radiation, t stands for peak width at half maximum of the most intense peak, and Θ is the angle between the beam and the normal to the reflecting plane.

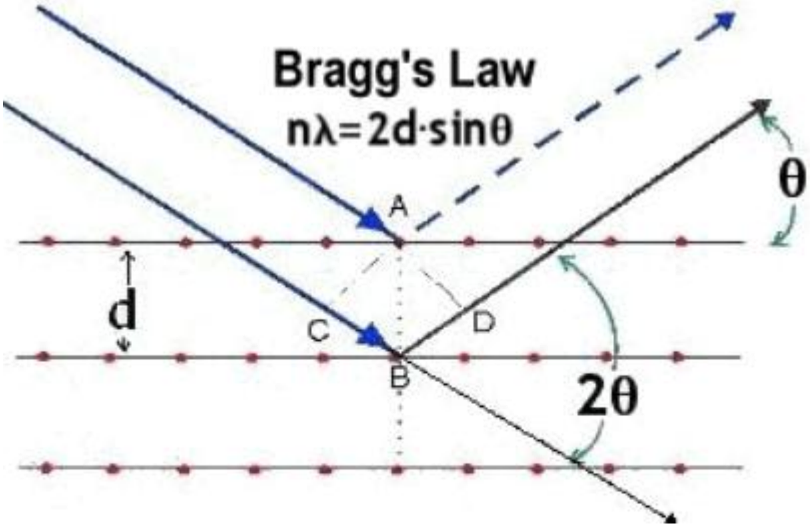

Figure 2.9: The Bragg relation and the interference of the X-rays that are scattered by atoms for an ordered crystalline structure.

The other essential information that can be acquired from XRD analysis is the alloy formation. Since the alloy is a solid solution, the process of alloying can be described by the replacement of the atoms in the lattice structure of the first metal by the second metal. Thereby, upon an introduction of the second metal, the solid solution with a certain degree of alloying occurs. Depending on the number of the atoms replaced by the second metal (the composition of the second metal in the lattice), new lattice spacing value will be obtained, according to Vegard’s Law [60]. Since the lattice spacing alters, the position of the most intense XRD peak of the first metal is shifted towards the most intense XRD peak of the second metal, according to the Bragg relation. The Figure 2.10 clearly shows the shifts in XRD diffractogram for an alloyed Pt-Ni bimetallic structure. Any peak belonging to neither metallic nickel nor its oxide is detected. The symmetric peaks are observed. The increasing nickel content was found to increase the shift. All of these are the indications of the alloy formation.

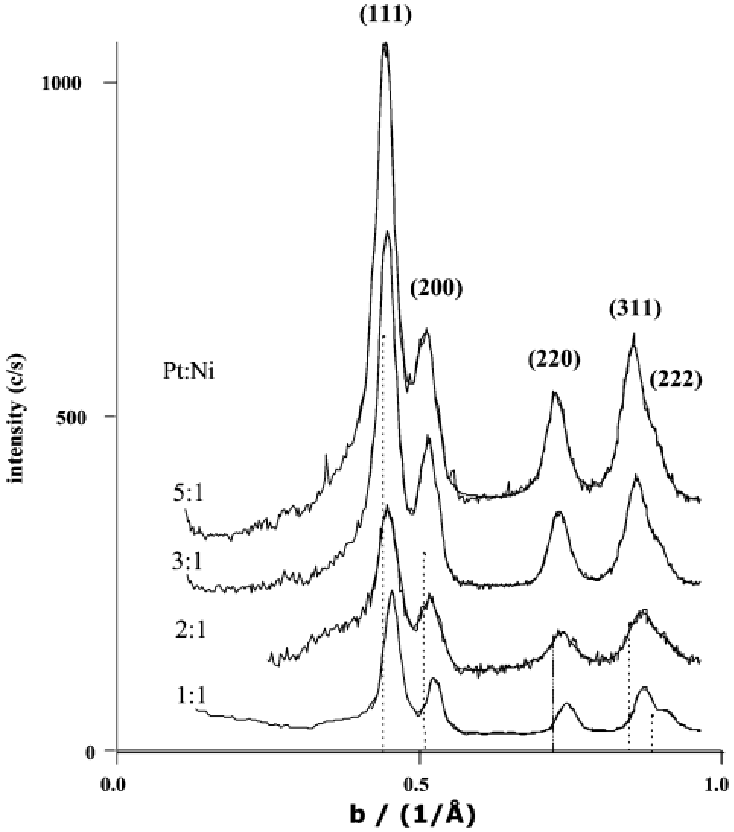

Figure 2.10: WAXS patterns shown with offsets of each by 100 (c/s) for Pt Ni(5:1), (3:1), (2:1), and (1:1) carbon-supported catalysts with 20 wt % metal loading. The patterns are corrected for the background produced by Vulcan XC-72 support, and corrected for the usual angular factors: polarization, absorption, and geometrical factor. The high intensity at the left wing of the first peak is indicative of some fractional surface oxide. Reference lines for Pt are also shown in dotted bar, *taken from* [61].

Another powerful technique used in the characterization of the supported nanoparticles is Transmission Electron Microscopy (TEM). It enables the observation of the morphological properties such as the particle size, shape, and size distribution which is beyond the capabilities of the optical microscopes. The Figure 2.11 is a good example illustrating how TEM images can be used for the analysis of particle size and size distribution over the surface of the catalysts support. It is seen that Pt nanoparticles spread over the support surface with narrow particle size distribution with an increasing size for higher metal loadings.

Another information that can be obtained from the TEM images is the comparison of the particle size with the one obtained from Scherrer's Equation from XRD analysis. Since XRD is volume average and TEM is area specific characterization techniques, if the particle sizes obtained from both analyses match each other with small deviations (i.e. particle based and overall), then this implies the homogeneous distributions of the deposited metals.

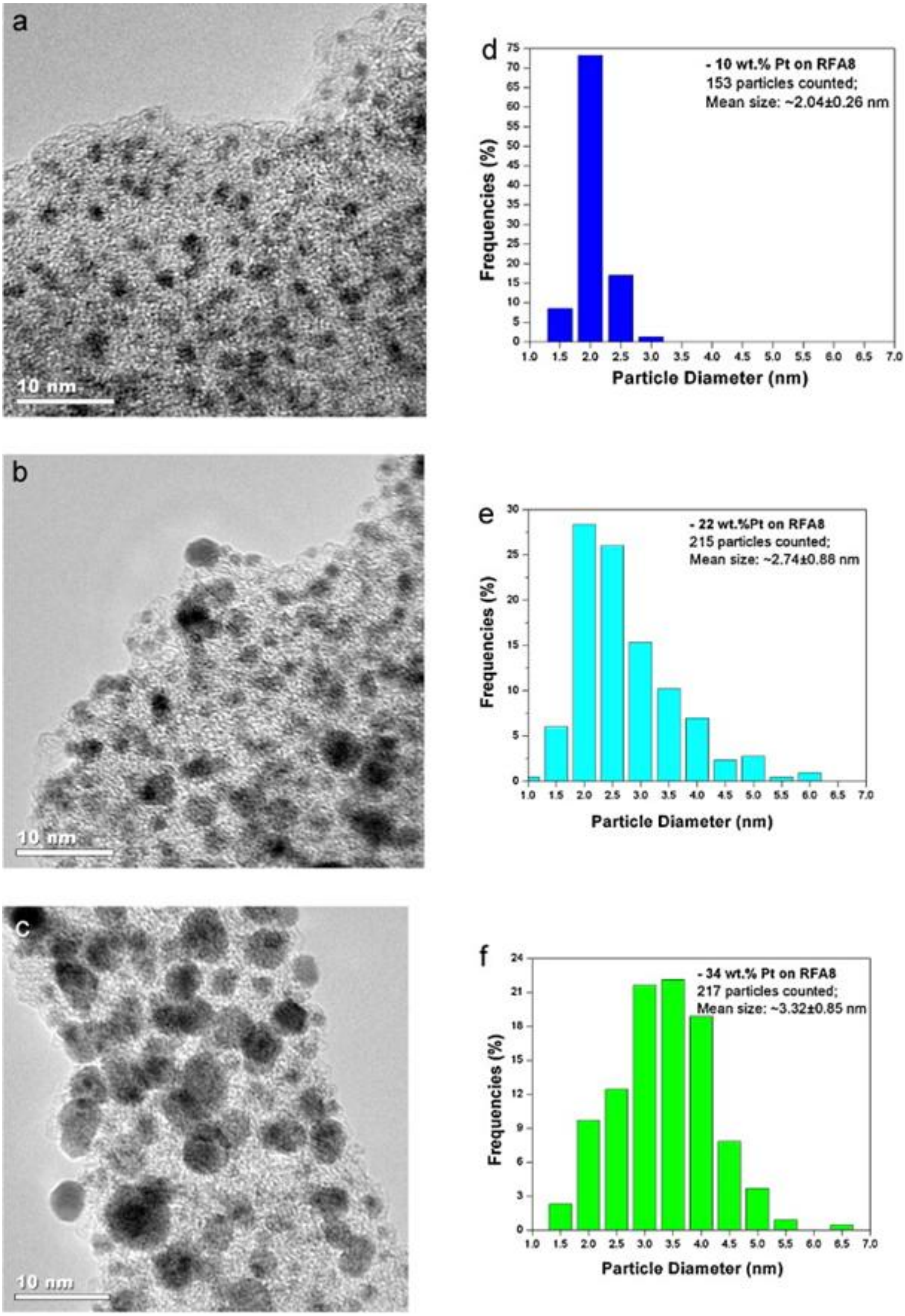

Figure 2.11: (a)–(c) BF TEM images of Pt/RFA composites with Pt loading of 10 wt.%,

22 wt.% and 34 wt.%, respectively. (d)–(e) Particle size distributions measured from images such as (a)–(c), respectively, *taken from[62]*.

TEM images, when analyzed in details, can also provide information on alloying and/or core-shell structures of the bimetallic nanoparticles, as given in Figure 2.2 above. Further analysis can also be made by obtaining High Resolution TEM (HRTEM) images and calculating the lattice constants, as given in Figure 2.12 below. If the measured lattice constant value is between the lattice constant values of the two metals (monometallic Pd and monometallic Au), then this implies an alloy formation with a certain degree of alloying that can again be calculated from this observed lattice constant value.

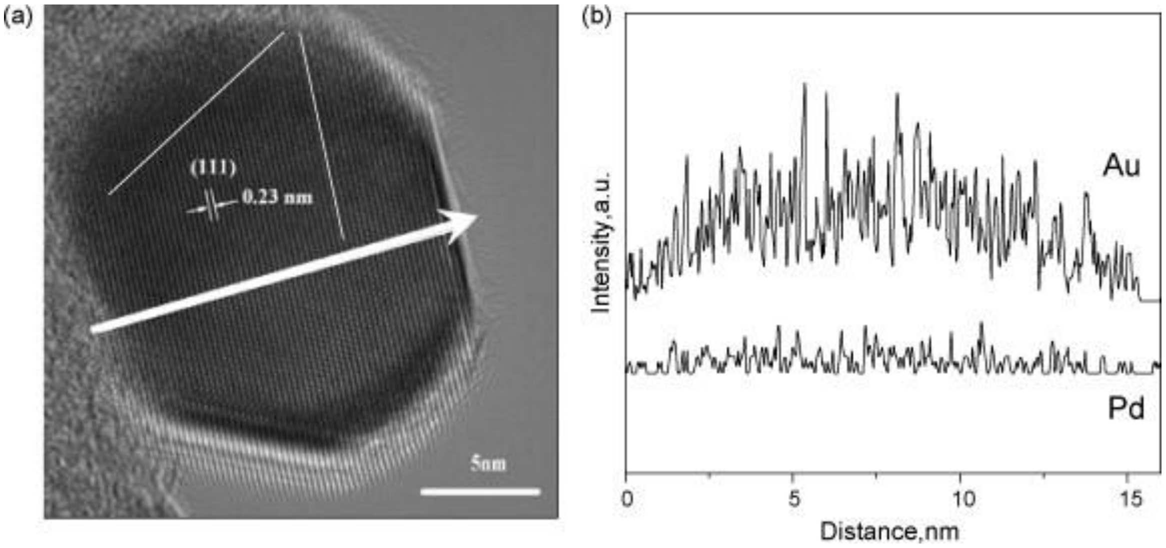

Figure 2.12: (a) HR-TEM image and (b) EDX intensity profile of a single 1Au5Pd/APS-S16 bimetallic nanoparticle *taken from[63]*.

Another characterization technique which is usually coupled with TEM analysis is EDXS which provides information about the chemistry of the deposited particles. Especially when bimetallic systems are studied, phase separations can easily be detected. The Figure 2.13 below shows the EDXS results of PtPd samples over BP2000. Huge deviations in EDXS weight compositions imply that Pd atoms segregated on some parts of the surface instead of interacting with platinum to form PtPd nanoalloys. On the other hand, if particle based and overall chemistry analysis of the bimetallic particles were close to each other, than this would suggest an homogeneous distribution of the metals, which is not the case for this sample.

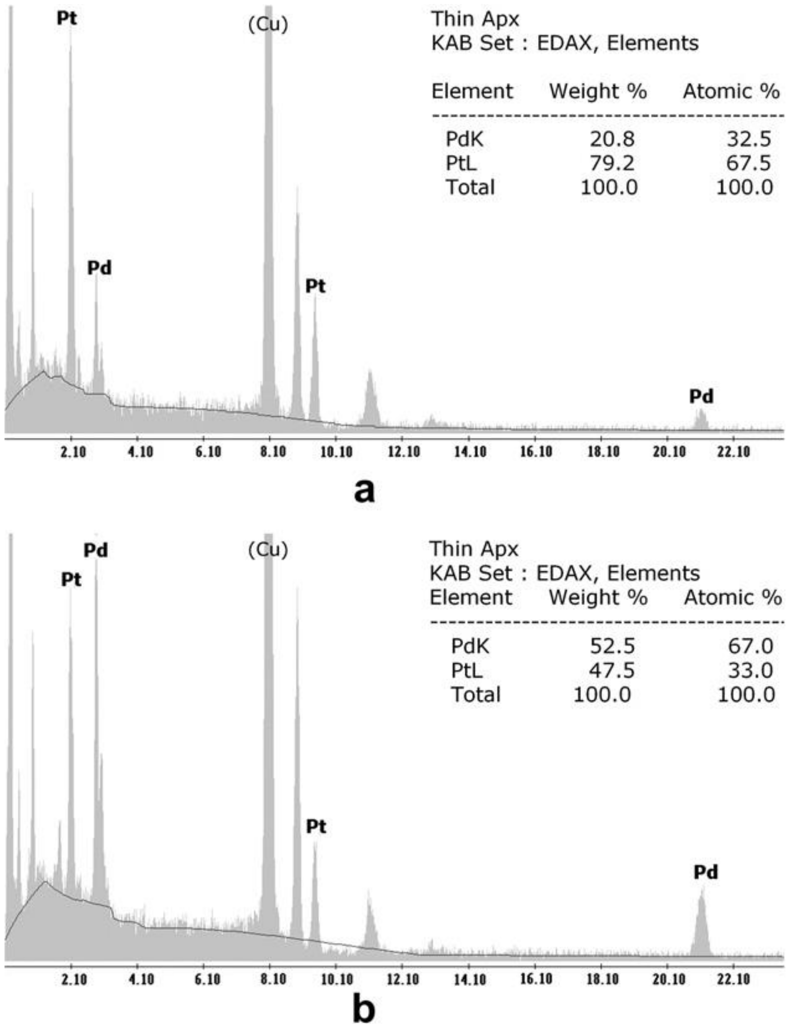

Thin Apx
KAB Set : EDAX, Elements

Element	Weight %	Atomic %
PdK	20.8	32.5
PtL	79.2	67.5
Total	100.0	100.0

Thin Apx
KAB Set : EDAX, Elements

Element	Weight %	Atomic %
PdK	52.5	67.0
PtL	47.5	33.0
Total	100.0	100.0

Figure 2.13: EDXS weight compositions of the PtPd/BP2000 (2:1) catalyst. (a) small particles between 1 and 4 nm & (b) Bigger particles (over 5 nm), *taken from[64]*.

In addition to the structural characterization techniques, Cyclic voltammetry (CV) on the other hand is a technique which provides information about the electro catalytic activity of the catalysts. In CV analysis, voltage is swept between two values from V1 to V2 (See Figure 2.14) and when a voltage value of V2 is reached the voltage is swept back to V1 during which current drawn from the system is recorded. In CV analysis, generally, two different types of reactions are studied: hydrogen oxidation reactions (HOR) occurring at the anode and oxygen reduction reactions (ORR) in which hydrogen and oxygen react and form water occurring at the cathode sites of the fuel cells.

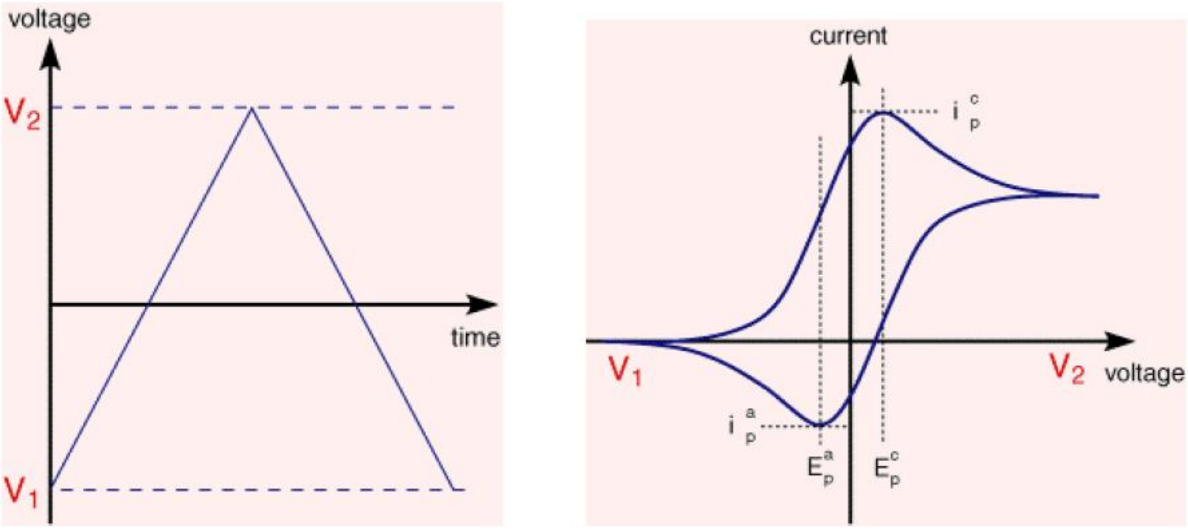

Figure 2.14: Voltage as a function of time and current as a function of voltage for CV, *taken from[65]*.

HOR reactions provides information about electrochemically active surface area of the synthesized catalysts. A sample HOR diagram for Pt is given in Figure 2.15 below.

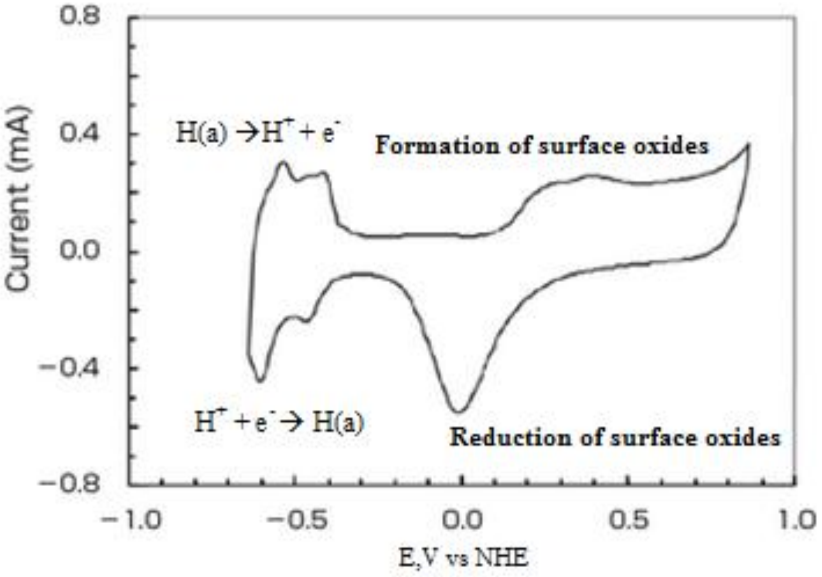

Figure 2.15: Cyclic Voltammogram of Pt

Different adsorption and desorption peaks between -0.2 V and -0.6 V are observed with mirror images which are resulted by the adsorption on different crystallographic planes on the surface of Pt. Towards positive voltage values, the peaks belonging to the formation and reduction of surface oxide are observed. The hydrogen desorption peaks on the reduction part of the curve are further used for the estimation of the electrochemically active surface area (ESA) of the catalysts. The utilization of the supported nanoparticles can also be calculated by CV analysis. By assuming the supported nanoparticles are in spherical shape and by obtaining size of the nanoparticles from TEM and/or XRD analysis, when combined with the metal loading value, total surface area of the supported nanoparticles can be calculated. If ESA is divided by this value, then utilization of the nanoparticles can be obtained.

Regarding the kinetics of fuel cell reactions, ORR measurements are carried out as well. The Figure 2.16 shows a sample ORR measurement. It is observed that at low rpm values, the range of 0-0.3V is observed to be the diffusion controlled region. As for the region between 0.3-0.7V, it is the area that mixed diffusion-kinetic control with a function of the rotation speed becomes dominant. Finally, the values between 0.7-1.0V are the kinetics controlled range with an independency on rotation speeds.

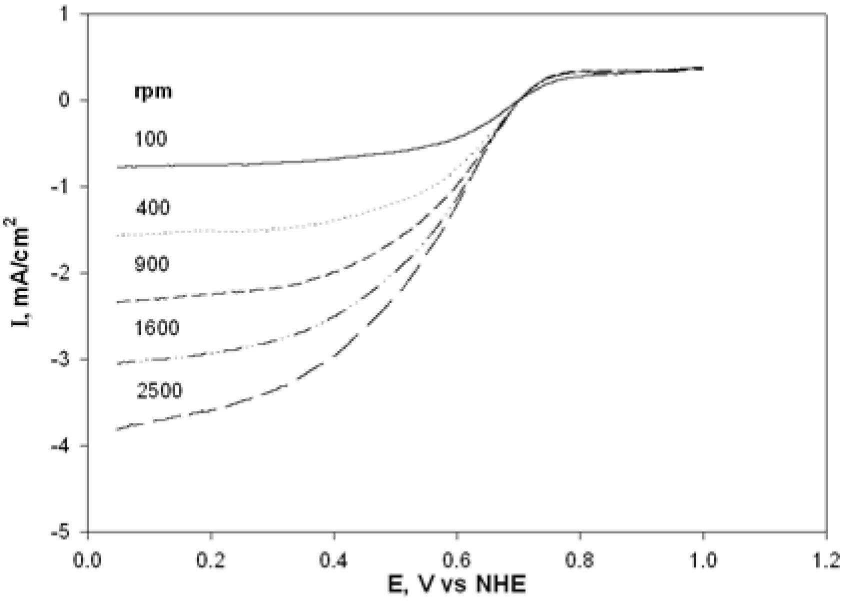

The Figure 2.16: Hydrodynamic voltammograms of positive scans of PtNi/Carbon Aerogel for O_2 reduction in O_2 saturated 0.1 M $HClO_4$.

3. EXPERIMENTAL

3.1.Materials

Dimethyl (cyclooctadiene) platinum (II) ($PtMe_2COD$) (99.9%) and Bis(2,4-pentanedionato)nickel(II) (Niacac2) were purchased from Strem Chemicals. Vulcan XC 72R carbon black powders were obtained from Cabot International. Spherical γ-alumina particles with a diameter of 1.6 mm were purchased from Saint-Gobain NorPro, Inc. For the carbon aerogel preparation, resorcinol (99%), formaldehyde (37%), and sodium carbonate (99.99%) were bought from Aldrich and used without further purification. The supports used in this study were dried in the oven at 150 ^{o}C for 4 hours in order to remove the water. Carbon dioxide (99.998%), and nitrogen (99.999%) were purchased from Airgas.

3.2.Supercritical Carbon Dioxide Deposition Setup

The supercritical fluid deposition setup is shown in the Figure 3.1. The custom manufactured stainless steel vessel with a 54 ml volume was fitted with two sapphire windows (1 in, id; Sapphire Engineering, Inc.). In order to prevent the leakage, before and after the sapphire Windows, sealing is made with poly (ether ether ketone) O-rings. In addition, a vent line, a rupture disk assembly (Autoclave Engineers) and T-type thermocouple assembly (Omega Engineering, PX300-7.5KGV) are included in the system.

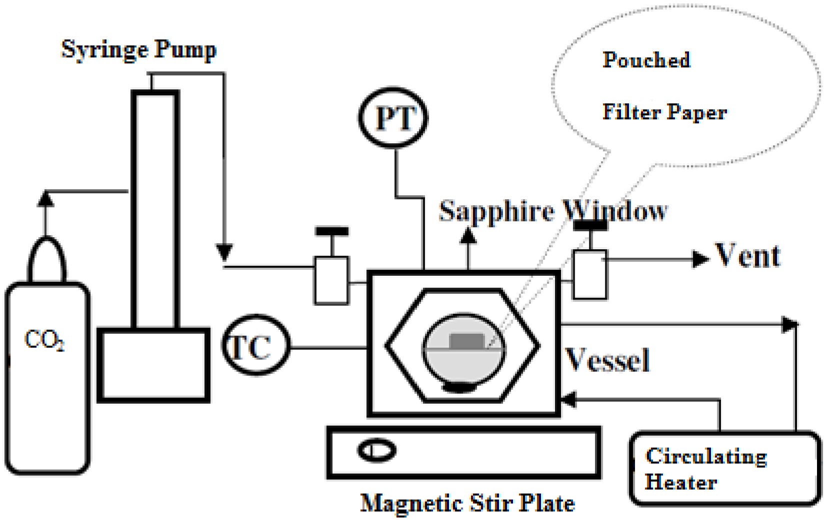

Figure 3.1: Figure shows the supercritical Carbon Dioxide Deposition Setup.

3.3.Experimental Methods

3.3.1. Preparation of Carbon Aerogels

Carbon Aerogels (CAs) were prepared by polymerization of resorcinol with formaldehyde in water solution according to Pekala's procedure [31]. Briefly, a solution containing predetermined amounts of formaldehyde (F), sodium carbonate (C), resorcinol (R) and water (W) was kept at room temperature for 24 hours. At the beginning, the molar ratios of R/F, R/C and R/W were 0.5, 100 and 0.04, respectively. Then the tube containing the prepared solution was kept at 50 °C for another 24 hours, and at 90 °C for 72 hours. Upon this polymerization process, the solvent-exchange is applied to the monolith which was achieved by immersing it into acetone for at least 12 hours. Consequently, water is exchanged with acetone. As for the extraction of acetone from the pores of the monolith, supercritical carbon dioxide extraction is applied at 50 ^{o}C and 138 bars for 8 hours. After the extraction process, Resorcinol-formaldehyde Aerogels (RFAs) were obtained. Conversion of them into carbon aerogels is done by pyrolysis in an inert nitrogen atmosphere. Those RFA monoliths are inserted in an alumina process tube (Cole Parmer) with dimensions of 25 mm (id), 28 mm (od), 1219.2 mm (length) and this tube is placed into a tube furnace (Thermolyne 21100 Tube Furnace). The oven was kept at 1000 ^{o}C for 6 hours under a nitrogen flow at approximately 100 cm^3/min. Finally, the system was let to cool room temperature.

3.3.2. Preparation of Supported Monometallic Nickel and Platinum Nanoparticles

The supported monometallic nickel and monometallic platinum nanoparticles were prepared on γ-alumina, Vulcan XC 72R, and CAs. In a typical run, predetermined amounts of support and $PtMe_2COD$ (for Pt nanoparticles synthesis) or $Ni(acac)_2$ (for Ni nanoparticles synthesis) were placed into the 54 mL deposition vessel. The required amounts of precursors and supports were weighed by using an analytical balance (Adventure Model Ar 2140) accurate to ±0.1 mg. As for the powdered support used in this study which was γ-alumina, the weighed amounts of Vulcan XC 72R was put into a bag made of filter paper. The pouched filter paper was put onto the stainless steel screen that was used to separate the stirring bar and the support composites.

Deposition process for the monometallic nickel and platinum nanoparticles were achieved by different strategies. The details of deposition and reduction processes are given in Table 3.1. Since the solubility of the nickel precursor in supercritical carbon dioxide is low, a few amounts of methanol (~5mL) as an entrainer was introduced into the system before it was charged with scCO2. After closing the vessel, it was heated by using a circulating heater/cooler (Fisher Scientific Isotemp Refrigerated Circulator Model 80). When the thermal equilibrium was reached, the system was charged slowly with carbon dioxide up to the desired pressure by using a syringe pump (ISCO, 260D) The metal loading values were obtained from the weight change of the support before and after the deposition process.

As for the reduction processes, the adsorbed precursor-support composites were loaded in an alumina process tube (Cole Parmer) with dimensions of 25 mm (id), 28 mm (od), 1219.2 mm (length) and this tube was placed into a tube furnace (Thermolyne 21100 Tube Furnace). Nickel nanoparticles were obtained by chemical reduction under hydrogen flow of ~100cm^3/min. In order to remove the adsorbed hydrogen molecules from the surface of the carbon support, the system was purged with nitrogen at a higher temperature. On the other hand, thermal reduction was applied for the synthesis of Pt nanoparticles under a nitrogen flow at ~100cm^3/min.

Table 3.1: The details of the deposition and the reduction processes for the synthesis of supported monometallic nickel and platinum nanoparticles.

Support	**Metal**	**Conditions**	**Entrainer**	**Reduced by**	**Reduced at (^{0}C)**
γ-Al2O3	Ni	30MPa, 60^{0}C and 72hours	√	H_2-120 minutes	180 ^{0}C
	Pt	24.2MPa, 70^{0}C and 24 hours	X	N2-240 minutes	200 ^{0}C
Vulcan XC 72R	Ni	30MPa, 60^{0}C and 72hours	√	H2-120 minutes + N2-30minutes	170^{0}C + 190^{0}C
	Pt	24.2MPa, 70^{0}C and 24 hours	X	N2-240 minutes	200 ^{0}C
CA	Ni	30MPa, 60^{0}C and 72hours	√	H2-120 minutes + N2-30minutes	140^{0}C + 160^{0}C
	Pt	24.2MPa, 70^{0}C and 24 hours	X	N2-240 minutes	200 ^{0}C

3.3.3. Preparation of Supported Bimetallic Pt-Ni Nanoparticles with Different Deposition Orders

For the preparation of bimetallic Pt-Ni nanoparticles, a two-step procedure termed sequential deposition was used. The details are given in Table 3.2. First, Pt nanoparticles were deposited on the supports by adsorption of $PtMe_2COD$ from scCO2 solution followed by reduction of the adsorbed precursor to Pt by heat treatment at 200 ^oC under flowing nitrogen at ~100cm^3/min. Subsequently, nickel acetylacetonate was adsorbed on Pt/support from $scCO_2$. The adsorbed Ni precursor was then reduced to Ni by heat treatment under hydrogen flow at ~100cm^3/min. In order to investigate the effect of the deposition order of the metals on both morphology and activity of the catalysts, the reverse of this procedure was also applied. First, supported monometallic nickel nanoparticles over the support were prepared and those catalysts were used as a support for the deposition of $PtMe_2COD$. The reduction of Pt precursor into Pt was achieved by thermal reduction at 200 ^oC.

Table 3.2: The details of the deposition and the reduction processes for the synthesis of supported bimetallic nickel-platinum nanoparticles with different deposition orders.

Support	**Metal**	**Conditions**	**Entrainer**	**Reduced by**	**Reduced at (^0C)**
Pt / γ-Al2O3	Ni	30MPa, 60^0C and 72hours	√	H2-120 minutes	180 ^0C
Pt / Vulcan	Ni	30MPa, 60^0C and 72hours	√	H2-120 minutes + N2-30minutes	170^0C + 190^0C
Pt / CA	Ni	30MPa, 60^0C and 72hours	√	H2-120 minutes + N2-30minutes	140^0C + 160^0C
Ni/CA	Pt	24.2MPa, 70^0C and 24 hours	X	N2-240 minutes	200 ^0C

The table 3.3 below separately shows the use of entrainer throughout the preparation of the supported monometallic and bimetallic nanocatalysts.

Table 3.3: The use of entrainer for the preparation of the nanocatalysts is given below.

	γ-Alumina	**Vulcan XC 72R**	**CA**
Ni on support	√	√	√
Pt on support	X	X	X
Ni on Pt/support	√	√	X
Pt on Ni/support	not carried out	not carried out	X

√: used X : not used

The use of methanol as an entrainer for the deposition of nickel nanoparticles over Pt/CA support was avoided since during the experiments, it was observed that the synthesized nanoparticles of platinum on carbon aerogel were highly active and when they were contacted with even the vapor of methanol at room temperature, the catalysts and the pounced filter paper got burned.

3.3.4. Preparation of Electrodes for Cyclic Voltammetry Measurements

Cyclic Voltammetry was used in order to characterize the electrochemical activity of the prepared catalysts (Pine Instrument). A standard three-electrode electrochemical cell was benefited for the measurements. The reference electrode was a silver-silver chloride electrode (Ag/AgCl, Cl^-). A salt bridge filled with 0.1 M KCI solution was used to connect the reference electrode to the cell in which CV measurements were done. A glassy carbon (GC) electrode (5 mm in diameter) and Pt wire were used as the working and counter electrodes, respectively. The catalyst ink solutions were prepared by mixing predetermined amounts of the prepared catalysts with 0.5 ml deionized water, 0.5 ml 1,2-propandiol and 220 μL % 5 wt Nafion solution (Ion Solutions Inc.). For all of the CV measurements, the loading of the catalysts on the GC electrode was 10 $\mu gPt/cm^2$. The catalysts solution was homogenized for 1 hour by a homogenizer (Ultra-Turrax® T25). In order to achieve the desired meal loading, 5.8 μL of the catalyst solution is poured on GC electrode. Then, the GC electrode was left to overnight drying.

3.4. Characterization

In the concepts of supported metals for catalysis, the characterization of both the naked supports and the prepared supported metals are important. In this study, the surface area and pore size distributions were analyzed by Brunauer, Emmett and Teller (BET) and the acidity measurements were handled by Temperature Programmed Desorption (TPD) measurements. In order to identify the crystalline structure of the deposited metals, X-ray Diffraction (XRD) was used. Also, volume average particle size calculations were done based on the most intense peak of XRD spectra. The size distribution of the deposited particles was revealed by Transmission Electron Microscopy (TEM) together with the chemical analysis of the particles achieved by Energy Dispersive Spectroscopy (EDS). TEM pictures were also used for the particle size calculations if the metal/support system is dilute and particle sizes are small that prevents the use of XRD for the calculation of particle sizes.

3.4.1. Characterization of Supports: BET and TPD Analysis

For the BET analysis, N_2 physisorption measurements were done in order to find the surface area, total pore volume and pore size distribution of γ-alumina, Vulcan XC72R and prepared CAs by using a Micromeritics ASAP 2020 instrument. Prior to the experiments, to remove the gases trapped in the pores of the supports, the support sample was degassed for 3 hours at 300 °C. The surface area calculations were done by using the linear portion of the BET equation. The estimation of the total pore volume was done by converting the volume of adsorbed nitrogen to the volume of bulk liquid, at the relative pressure value (P/P_0) of 0.99. Total pore size distribution and average pore diameter were determined by using the Barrett, Joyner and Halenda (BJH) method.

For the TPD analysis, Micromeritics Chemisorb 2750 system was used. The predetermined amount of the γ-alumina sample was placed into U shape quartz tube. Firstly, to remove the air from the U-tube, the system was purged with helium for minutes which was long enough to observe the base line again. Then, the surface cleaning was achieved by heating the system up to 500 ^{o}C with a rate of 20 ^{o}C/min under a helium flow at 20 sccm. Afterwards, the system was let to cool room temperature. Later on, the surface was saturated with ammonia by purging with 10% ammonia in helium gas mixture. In order not to use the physically adsorbed ammonia in the acidity calculations, before starting the desorption part of the experiment, the system was heated up to 120 ^{o}C and physisorbed ammonia was removed. Finally, the system was heated till 500oC with a rate of 20oC/min and the corresponding ammonia desorption peak was recorded. The details of the heat treatment procedure can be seen in the Figure 3.2.

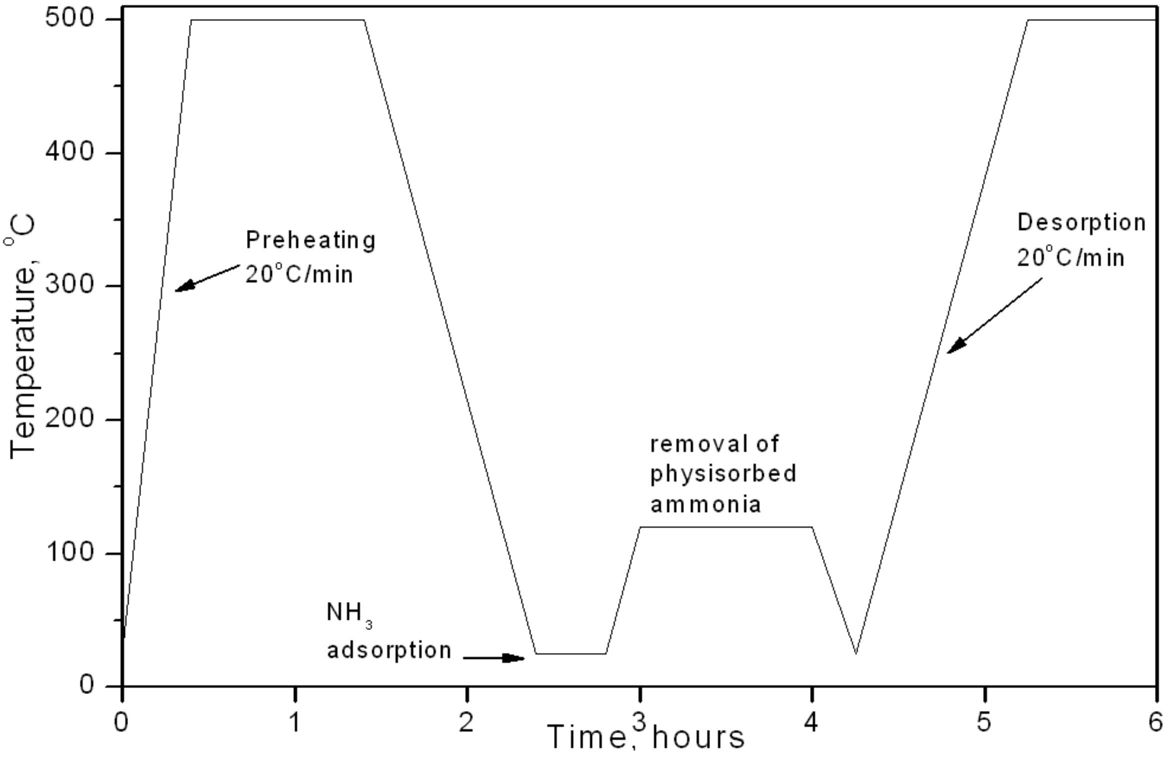

Figure 3.2: The heat treatment procedure for acidity measurements by TPD analysis is given in the figure.

3.4.2. X-ray Diffraction

The investigation of the crystalline structure of the supported monometallic and bimetallic nanoparticles was done by XRD. Huber G670 Imaging Plate diffractometer equipped with a Cu Kα radiation source was used for the measurements. The scanning range of 2θ was set between 10° to 85° with a step size of 0.01°. For a better accuracy, the overnight measurements were done for a period of 12 hours.

3.4.3. Transmission Electron Microscopy

The size distributions and morphology of the supported nanoparticles were analyzed by TEM images. TEM samples were prepared by crushing the catalysts with a mortar and pestle set. The resulting powders were suspended in a volatile solvent and ultrasonicated to obtain a uniform suspension. A few drops of the suspension were deposited on a copper mesh grid coated with a holey carbon film (Quantifoil Micro Tools GmbH). The TEM specimens were allowed to dry completely before examination in a JEOL 2010 FasTEM operating at 200 kV. This instrument is equipped with a high-resolution objective lens pole-piece (spherical aberration coefficient Cs ¼ 0.5 mm) giving a point- to-point resolution of <0.19 nm in phase contrast images.

3.4.4. Energy Dispersive Spectroscopy

The chemical analysis of the deposited particles was achieved by EDS. The measurements were done in situ using an EDAX Phoenix atmospheric thin window energy-dispersive X-ray spectrometer (EDXS).

3.4.5. Cyclic Voltammetry: HOR and ORR

CV measurements were done in 0.1 M HClO4 electrolyte solution. For the hydrogen oxidation reaction (HOR) measurements, the electrolyte was saturated with hydrogen for 30 minutes in order to remove the oxygen. The hydrogen supply tube was placed just on the top of the electrolyte solution before the experiments. The CV data were collected with respect to normal hydrogen electrode (NHE) at a scan rate of 50mV/s. As for the oxygen reduction reaction (ORR) experiments, the surface of the electrode was cleaned by 50 HOR cycles which is the number found to be most suitable based on different trials. Then, the flow gas was changed from hydrogen to oxygen and the electrolyte solution was saturated with oxygen for 30 minutes. Before starting the ORR measurements, the oxygen supply tube was placed to fluid phase at the top of the electrolyte solution. The rotation speeds of this study were 100, 400, 900, 1600 and 2500 rpm. The hydrodynamic voltammograms were recorded between 0.0-0.8 V at a scan rate of 10 mV/s. Electrochemical surface area (ESA) calculations were performed by using the area under the reduction part of the curve according to the equation given elsewhere [36]. All the experiments were performed at room temperature.

4. RESULTS AND DISCUSSION

4.1.Supports

The Figure 4.1 shows the desorption behavior of the γ-alumina support used in this study. The system was calibrated by purging the known amount of ammonia and calculating the corresponding peak area. The acidity was found as 0.491 mmol NH_3 / g catalysts which is a reasonable value regarding the acidity measurements of the γ-alumina in the literature. The unsymmetrical behavior of desorption peak can be ascribed to the faster ramp of the temperature program.

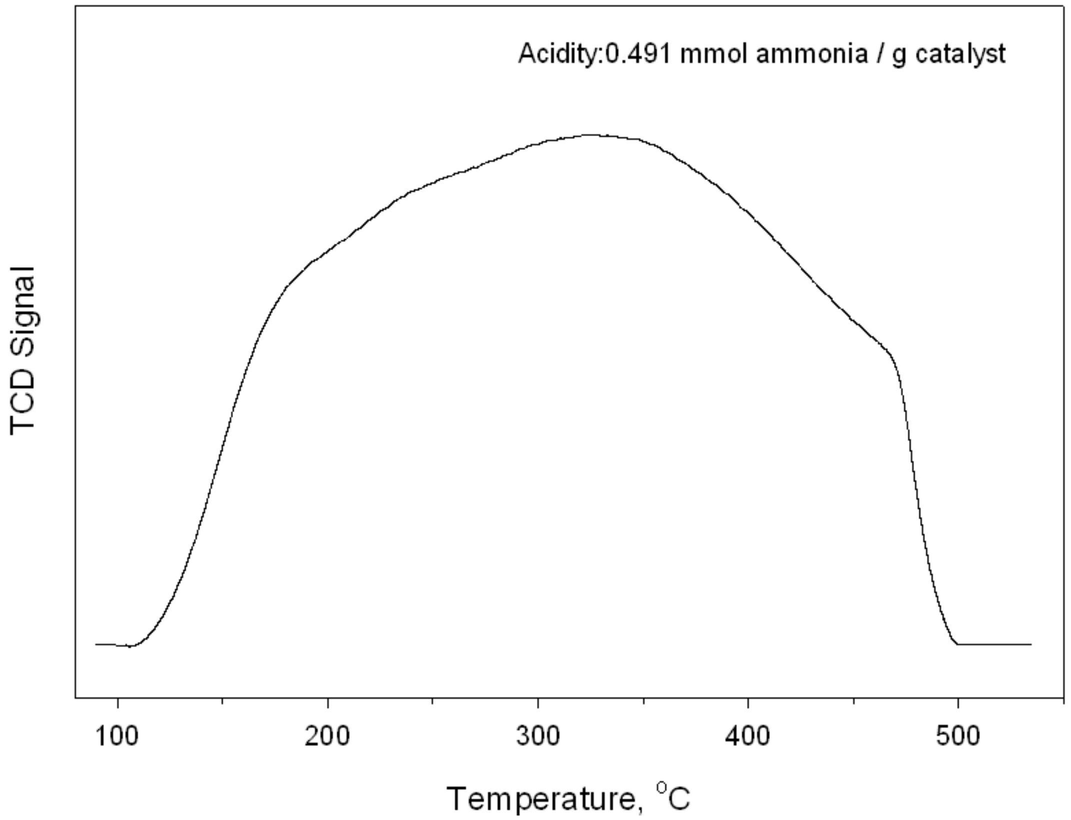

Figure 4.1: TPD of ammonia results of γ–alumina.

For support characterization, BET measurements were also carried out. CA support was found to have a surface area of 747 m^2/g, average pore diameter of 22 nm and pore volume of 4.1 cm^3/g. The Vulcan XC72R was found to have a surface area of 213 m^2/g, pore diameter of 6.4 nm and pore volume of 0.48 cm^3/g. As for γ–alumina support, the surface area of 260 m^2/g, pore diameter of 10 nm and pore volume of 0.83 cm^3/g were determined.

4.2. Supported Monometallic Ni and Bimetallic Pt-Ni Nanoparticles with Different Deposition Orders

By SCD method, supported monometallic nickel nanoparticles were successfully deposited on γ-alumina, Vulcan XC 72R, and CA supports. The supported bimetallic Pt-Ni nanoparticles were synthesized by a technique called sequential deposition. Firstly, supported monometallic Pt nanoparticles (Pt/support) were prepared and used as a support for the incorporation of nickel nanoparticles (PtNi/support). To investigate the effect of the deposition order of the metals on both morphology and activity of the nanocatalysts, the order of sequential deposition was switched for CA support. The CA supported monometallic nickel nanoparticles were synthesized and used as a support for the deposition of Pt nanoparticles (NiPt/CA). The details of the weight percentages of the prepared nanocatalysts are given in Table 4.1.

Table 4.1: Table displays the loading of the selected nanocatalysts

	γ-Alumina	**Vulcan XC 72R**	**CA**
Ni	3%	1.40%	3.50%
PtNi (Pt deposited first)	sample a 2.6%Pt + 1.5%Ni	sample a 8%Pt + 2%Ni sample b 1%Pt + 0.1%Ni	sample a 2.2%Pt + 1%Ni sample b 4%Pt + 0.2%Ni sample c 4%Pt + 2%Ni
PtNi (Ni deposited first)	not carried out	not carried out	sample d 3.5%Ni + 3.6%Pt

In this section, the results of the experiments will be presented in a way that supported monometallic and bimetallic catalysts' characterization results of γ-alumina is given first and this is followed by the results of Vulcan XC 72R and of carbon aerogel.

The Figure 4.2 shows the XRD spectra of the 3 % nickel nanoparticles supported on γ-alumina (Ni/ γ-alumina) together with the corresponding TEM images and EDXS results.

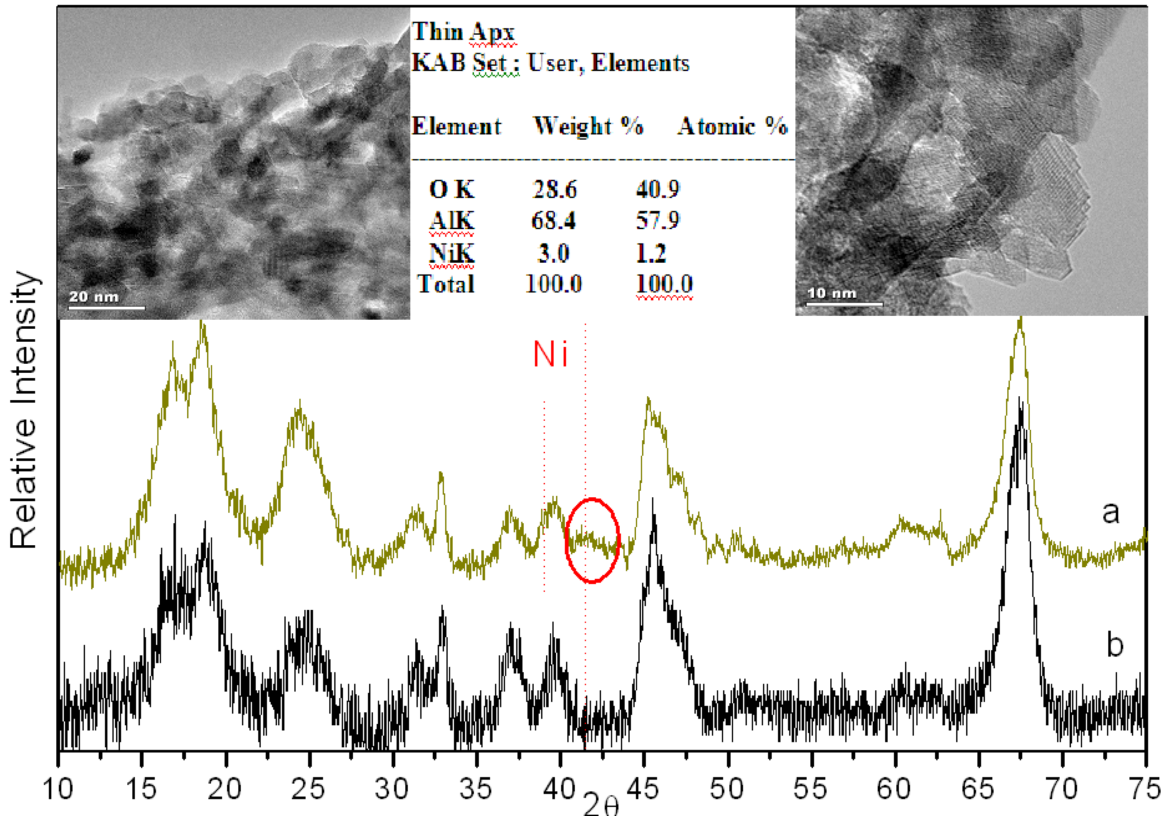

Thin Apx
KAB Set : User, Elements

Element	Weight %	Atomic %
O K	28.6	40.9
AlK	68.4	57.9
NiK	3.0	1.2
Total	100.0	100.0

Figure 4.2: The figure depicts the characterization results of the supported monometallic nickel nanoparticles on γ-alumina. (Top left and top right: TEM images; Top middle: Chemical Composition based on EDX results; XRD spectra a: 3% Ni on γ-alumina; XRD spectra b: pure γ-alumina)

Most intense XRD peak of metallic nickel is supposed to emerge at ~ 44.5^o followed by the peaks at 41.5^o and 39^o. However, it is shown in Figure 4.2 that the peaks of the polycrystalline γ-alumina collapse with the expected nickel peaks. Highly pronounced γ–alumina peak coming at ~45^o almost completely covers the expected nickel peak. On the other hand, small peak is observed at around 41.5^o which is so broad. This peak is missing on XRD of pure γ-alumina. It is so broad since the metal loading is low and particle size is at nanoscale. Moreover, symmetric γ-alumina peak at ~39.5^o is shown to become slightly asymmetric after nickel deposition which can be explained by the expected nickel peak at ~39^{o}.

For a better analysis of the morphology of the particles, TEM images of prepared Ni/γ-alumina samples are given separately on Figure 4.3.

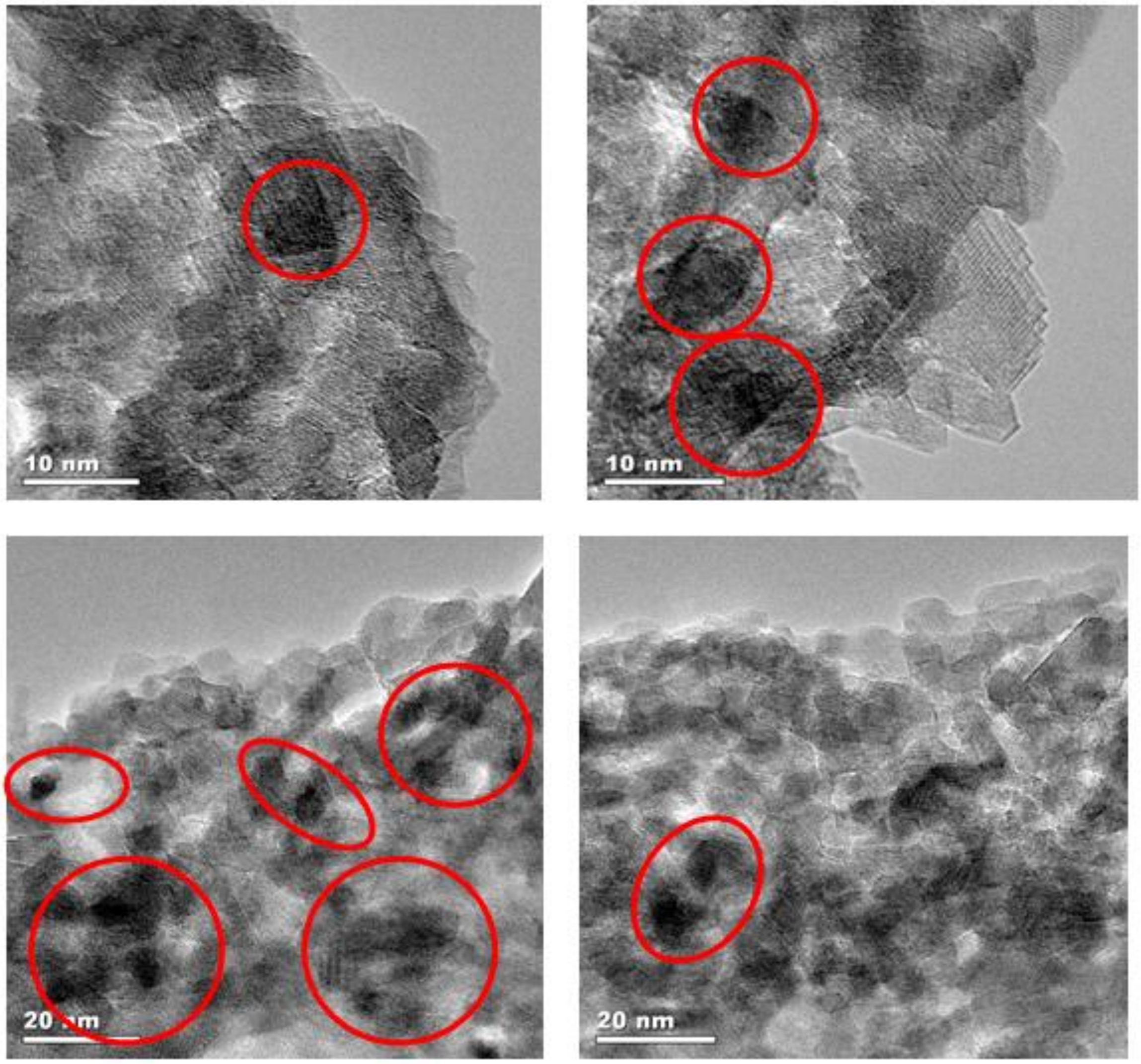

Figure 4.3: TEM images of monometallic nickel nanoparticles supported on γ-alumina.

Most of the supported nickel nanoparticles on γ-alumina are observed to be around ~6nm. Although the loading value and thereby the total number of the particles is low, the size distribution of the particles can be said to be narrow around 6nm.The shape of the particles are observed to be spherical.

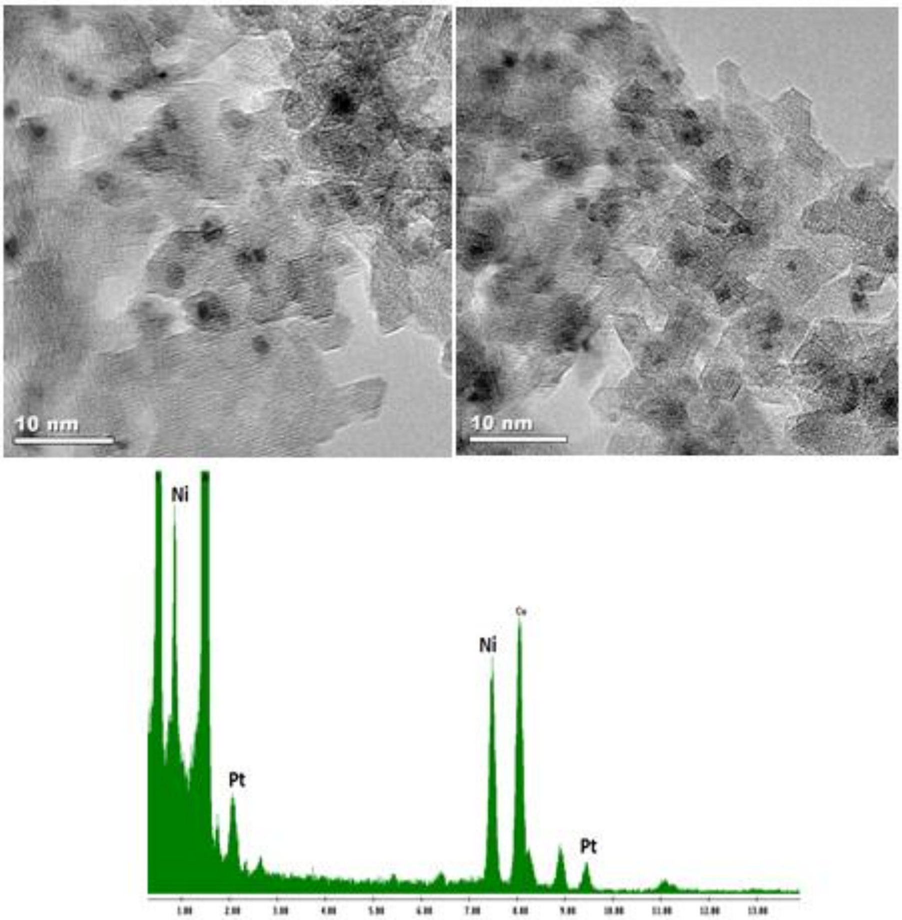

Figure 4.4. PtNi/ γ-alumina nanocatalysts. TEM image(top left& top right) and EDXS spectra (bottom).

TEM images and EDXS results of PtNi/ γ-alumina nanocatalysts are given in Figure 4.4. Supported nanoparticles of 1-3nm in size were observed with a narrow particle size distribution. It is interesting to note that size of the bimetallic Pt-Ni nanoparticles is smaller than the size of the monometallic Ni nanoparticles. The particle size distribution and shape of the bimetallic Pt-Ni nanoparticles are similar to the shape and size of the monometallic Pt nanoparticles on γ-alumina prepared by SCD [5]. This supports the argument stating that Ni nanoparticle formations occur with close contact to the Pt islands; therefore, instead of phase separation, bimetallic PtNi nanoparticles with homogeneous chemical compositions were obtained. Bayrakçeken et al studied Pt based bimetallic nanostructures by SCD and found that Pd agglomerate formations can be stabilized if there are pre-existing Pt islands on the surface but phase separation still occurred [49]. The findings of our study, on the other hand, states that Pt and Ni further interact with each other giving small composition variations in EDXS measurements indicating no phase separation.

As for the Vulcan XC 72R support, the supported monometallic nickel (Ni/Vulcan) and bimetallic (PtNi/Vulcan) nanoparticles by sequential deposition were successfully prepared. For the bimetallic nanocatalysts, the deposition of platinum nanoparticles was achieved first, and this was followed by the incorporation of nickel nanoparticles.

The XRD spectra of 1.4 % Ni on Vulcan XC 72R were inconclusive since the expected Ni peaks were close to those of carbon support, and the system studied here is so dilute with a loading of 1.4 %. In addition, as can be seen from the Figure 4.5, the synthesized supported metals were at nanoscale which makes the XRD peaks so broad. All of these make the detection of the corresponding XRD peaks of nickel nanoparticles quite difficult.

The Figure 4.5 displays the TEM images of the prepared Ni/Vulcan catalysts. It is shown that the SCFD technique enables the synthesis of monometallic nickel nanoparticles with a size of ~8nm. Because of the low loading, the population of the particles is observed to be low.

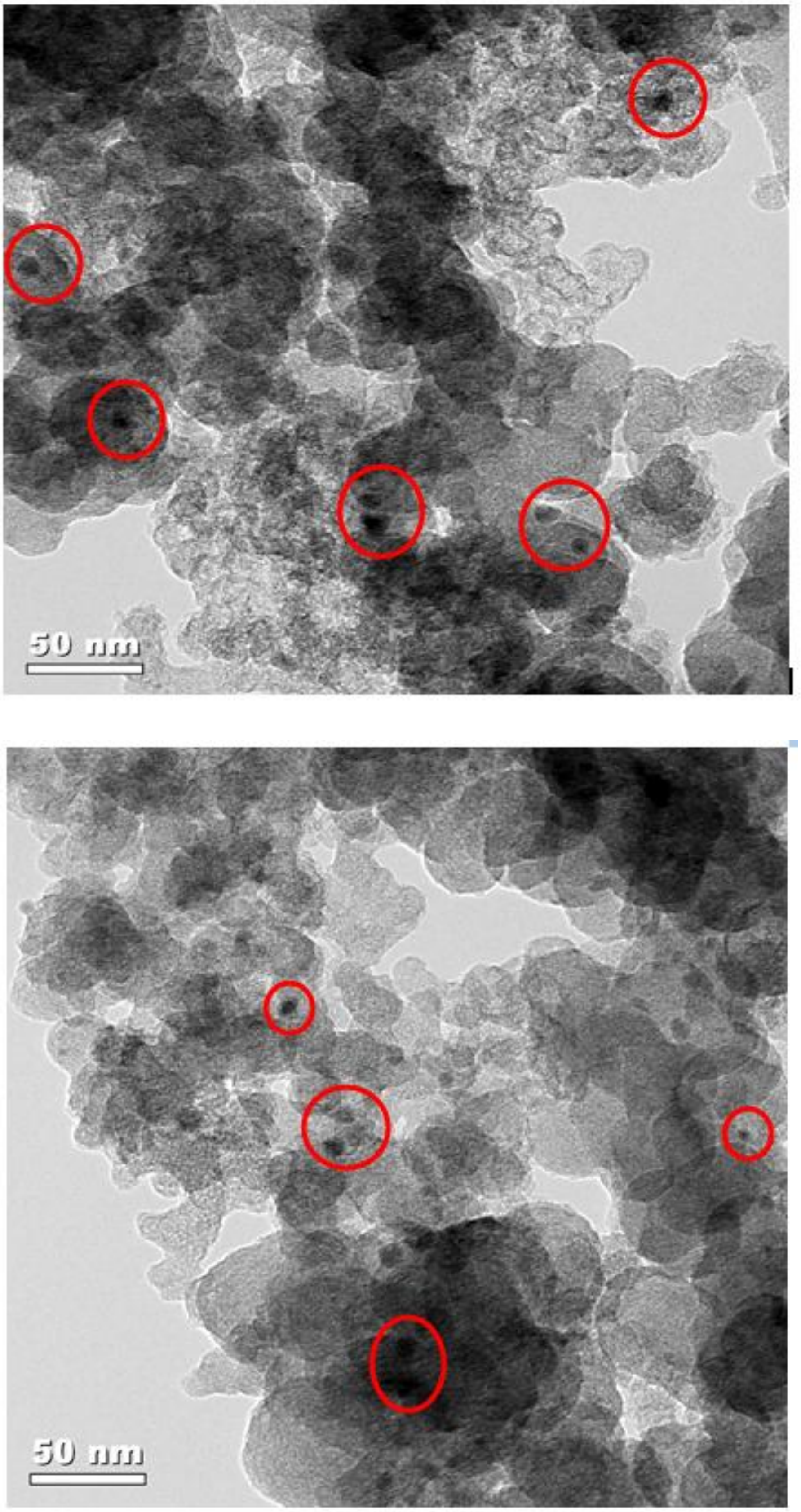

Figure 4.5: Large area TEM images of 1.4 Ni/Vulcan nanocatalysts with low population because of low loading value.

The Figure 4.6 below shows the chemical compositions of the deposited particles on TEM images of Ni/Vulcan nanocatalysts. EDXS spectrum on large area only displays the Ni metal peak, so all the particles in the TEM images are pure Ni.

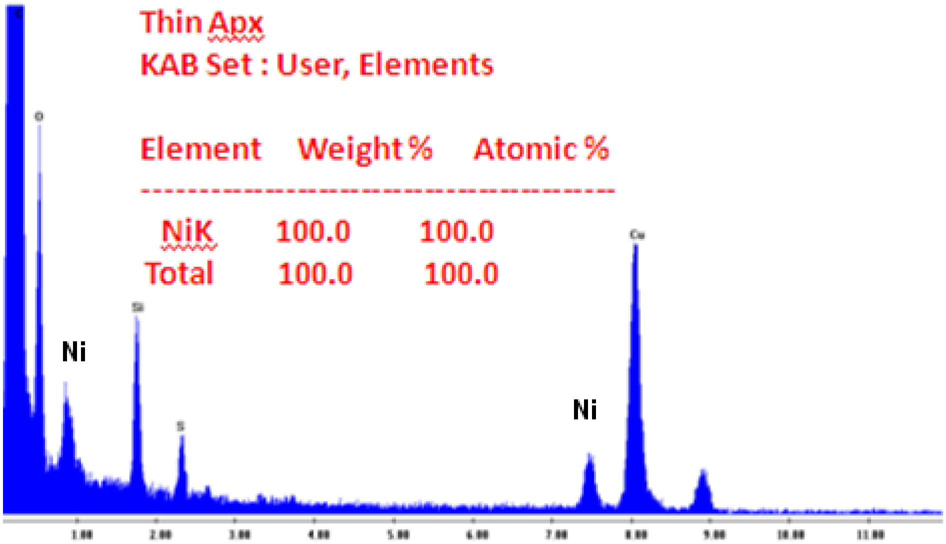

Figure 4.6: The EDXS spectrum of Ni/Vulcan nanocatalysts.

High magnification TEM images of Ni/Vulcan nanocatalysts are provided in Figure 4.7 for a better understanding of the morphology of the supported metal nanoparticles. Deposited particles with a size of ~8nm were observed to be spherical.

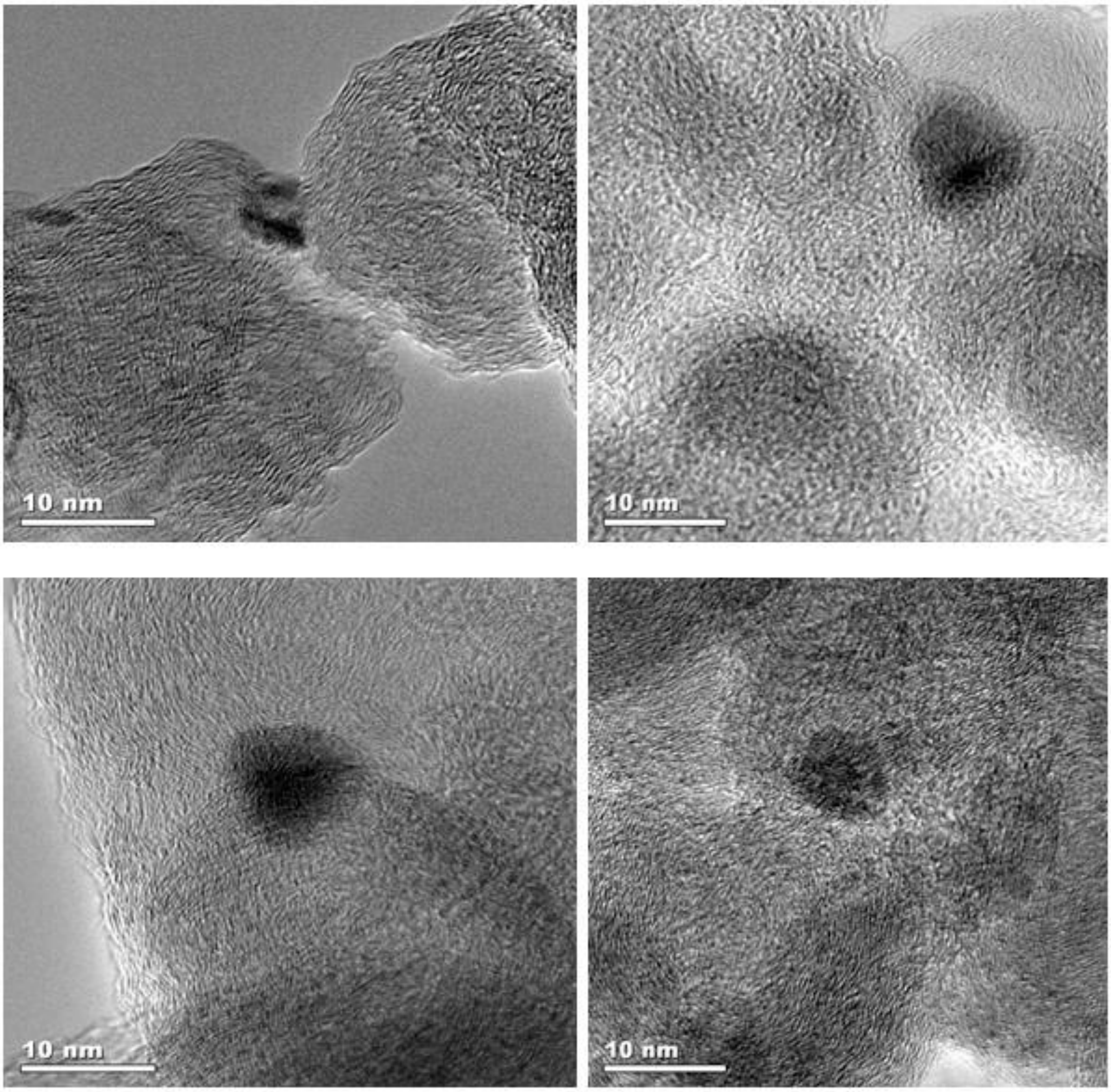

Figure 4.7: High magnification TEM images of 1.4 Ni/Vulcan nanocatalysts.

After the preparation of Ni/Vulcan nanocatalysts, sequential deposition technique was used to prepare two different PtNi/Vulcan nanocatalysts with different metal loading. As given in Table 4.1, the sample has a platinum loading of 8% and nickel loading of 2%. The corresponding XRD diffractogram is given in Figure 4.8 below.

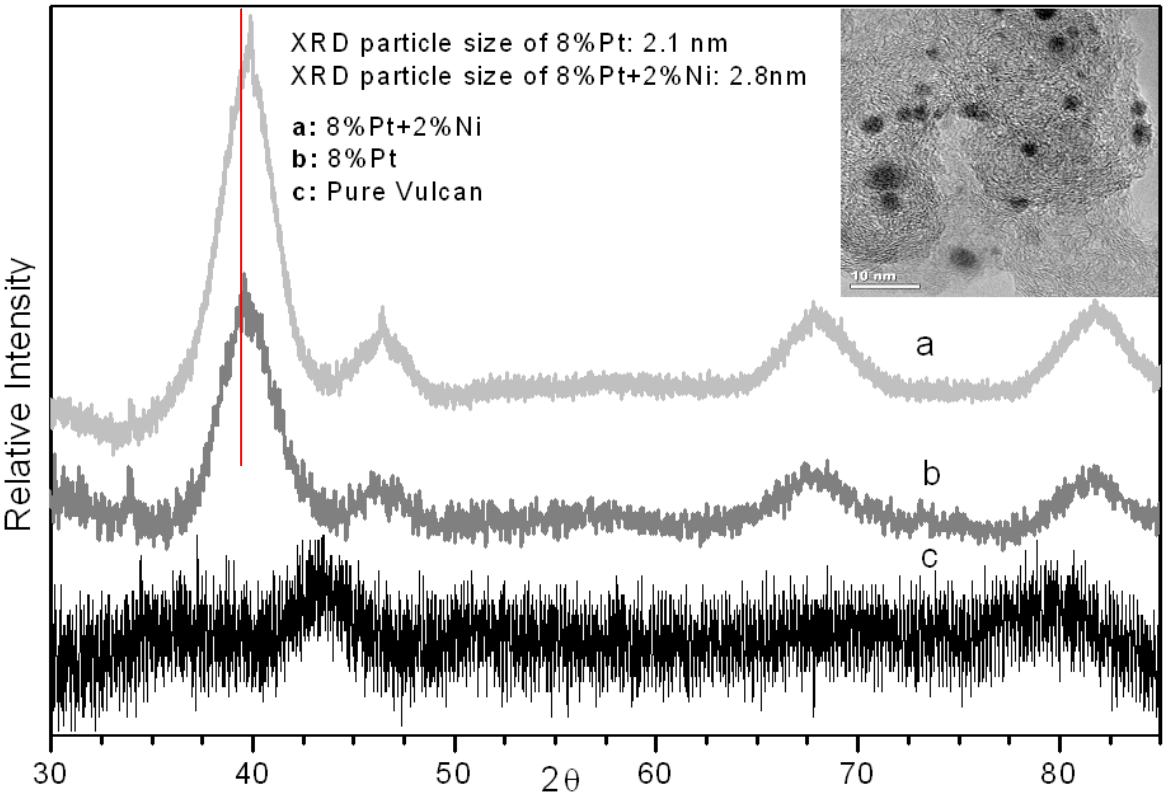

Figure 4.8: The figure shows the XRD diffractogram of pure Vulcan XC 72R (c), 8%Pt/Vulcan XC 72R (b), (8%Pt+2%Ni)/Vulcan XC 72R (a), particle size results calculated from (111) peak, and the corresponding TEM image of (8%Pt+2%Ni)/Vulcan XC 72R (top right-scale base is 10nm).

In Figure 4.8 the XRD diffractogram of pure Vulcan is also provided for a comparison and better analysis. (111), (200), (220) and (311) peaks belonging to the face centered cubic (fcc) crystal structure of Pt are shown on sample ‘b’ with 8% Pt loading at 2Θ angels of ~39^o, 46^o, 68^o, 80^o respectively. The symmetric peaks observed for sample ‘a’ with 2%Ni loading is important and may indicate the partial substitution of the Pt atoms from their lattice structure. The small shift in (111) peak towards higher 2Θ angles also supports this argument. Particle size was observed to increase from 2.1 nm (8 wt% Pt) to 2.8 nm (8 wt% Pt + 2 wt% Ni) after Ni deposition suggesting that Ni metal is not phase separated; instead Ni atoms grow on the previously deposited Pt islands. Moreover, the particle sizes of PtNi/Vulcan observed from TEM images and the values estimated from peak of (111) plane in XRD diffractogram by Scherer's Equations were close to each other (TEM with narrow size distribution: ~3nm; XRD: ~2.8nm). XRD provides information on the volume average based; on the other hand, information acquired by TEM images is specific to the area focused on the sample. These clearly indicate a quite narrow particle size distribution of PtNi/Vulcan XC72R nanocatalysts with a total metal loading of 10%.

The Figure 4.9 below shows the large area TEM images and corresponding EDXS results of (8%Pt+2%Ni)/Vulcan XC 72R nanocatalysts.

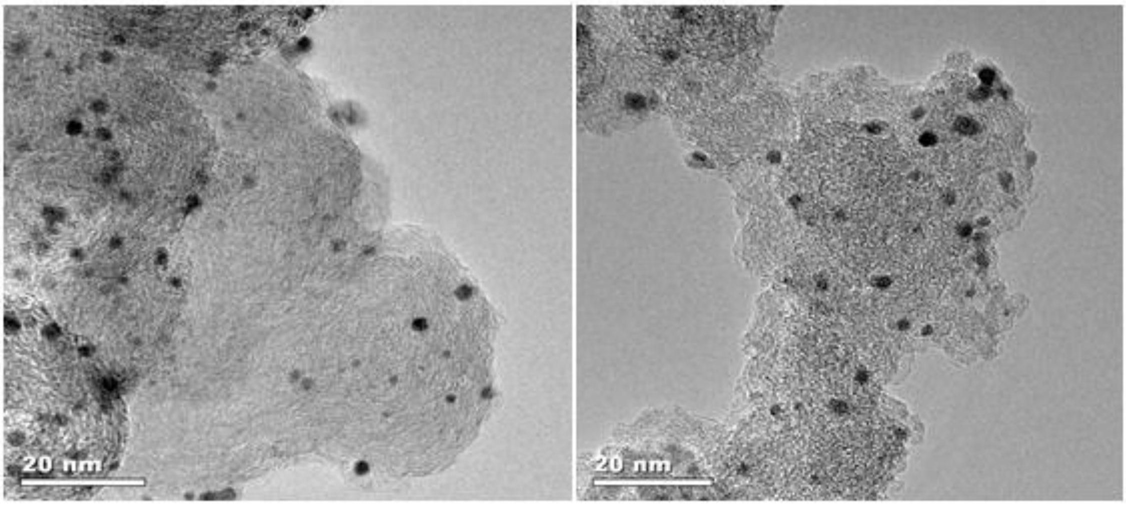

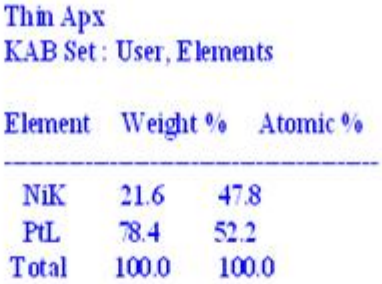

Thin Apx
KAB Set : User, Elements

Element	Weight %	Atomic %
NiK	21.6	47.8
PtL	78.4	52.2
Total	100.0	100.0

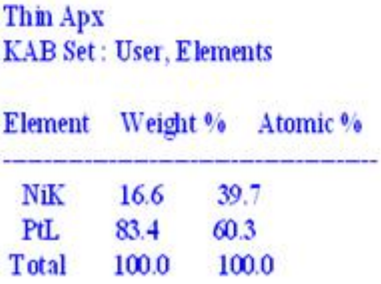

Thin Apx
KAB Set : User, Elements

Element	Weight %	Atomic %
NiK	16.6	39.7
PtL	83.4	60.3
Total	100.0	100.0

Figure 4.9: TEM images and corresponding EDX results of prepared (8%Pt+2%Ni)/Vulcan XC 72R nanocatalyst.

It was observed that the nickel to platinum ratios obtained from EDX analysis were slightly less than the ratios obtained from gravimetric analysis of the sequential deposition process. This is attributed to the weight losses occurring during the reduction of nickel precursor to metallic nickel. However, it is worth to note that the chemical composition results of the EDX spectrum both on the large area and the particle based do not differ too much when focused on different regions of the specimen prepared for TEM analysis. The fact that the particle based and large area based weight percentages are in agreement suggest that the metals are deposited over the catalyst surface uniformly. And this uniform distribution has several possible meanings: Either nanoalloys of platinum-nickel were successfully synthesized, or nickel incorporation occurred around the platinum nanoparticles resulting in a core-shell structure with platinum being in core and nickel at shell. At least, it can be stated that phase segregation of the platinum and nickel metals did not occur. In other words, the nickel nanoparticles did not grow on the support’s surface away from platinum islands. Instead, they either grow around the platinum nanoparticles to form the shell or the interaction further led them to form the nanoalloys. Alloying is still possible at the miscibility gap in which reduction temperatures and compositions are not enough for alloying, since alloying conditions of bimetallic structures deviates at nano scale from the conditions at bulk scale. In addition, alternative alloy structures may form such as fcc formation although hcp is expected at bulk compositions [57].

Other TEM images of the prepared (8%Pt+2%Ni)/Vulcan XC 72R sample are shown below in Figure 4.10.

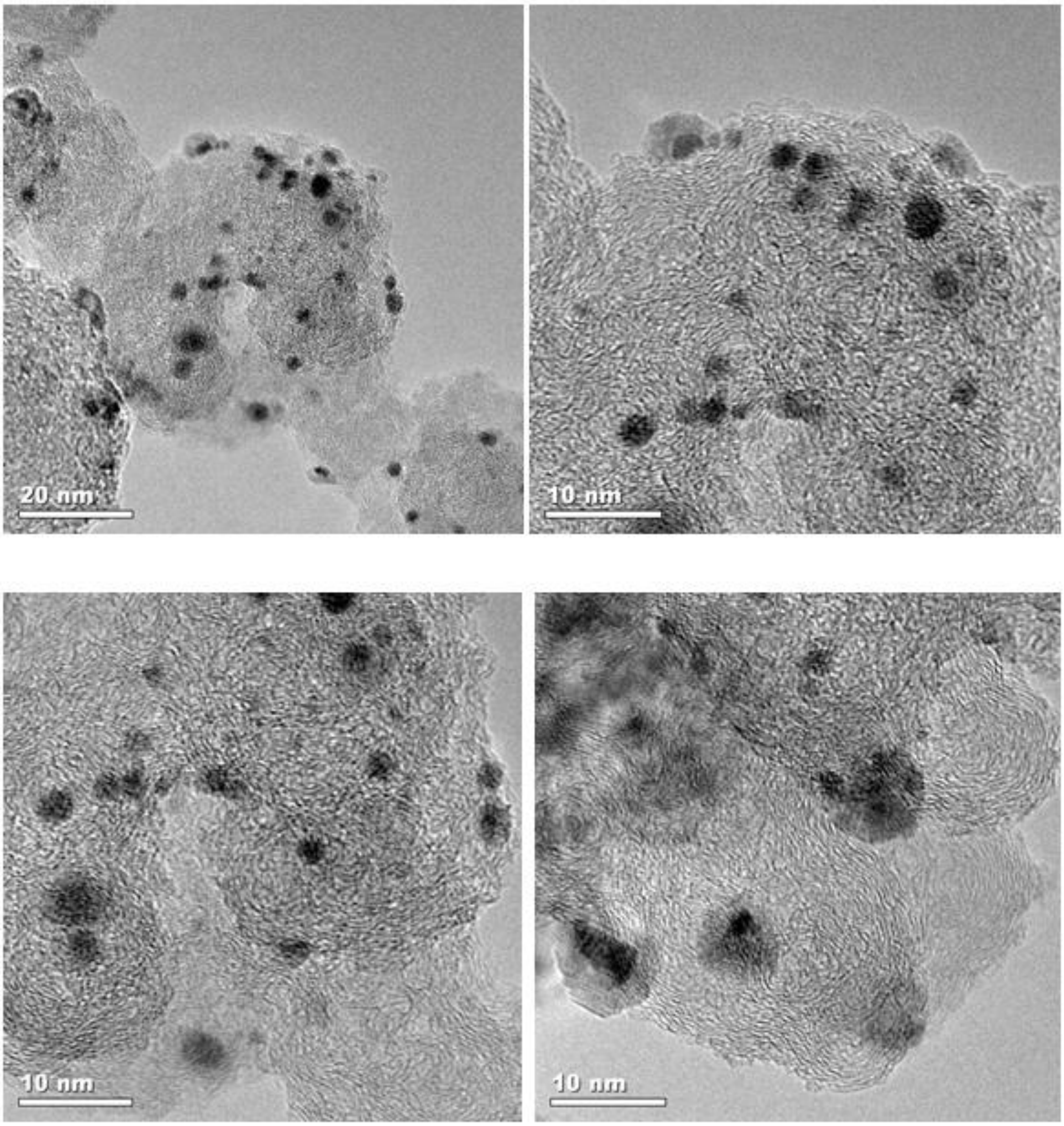

Figure 4.10: High magnification TEM images of (8%Pt+2%Ni)/Vulcan XC 72R nanocatalyst.

The interesting results are obtained on Vulcan sample regarding the particle size distribution of the prepared supported monometallic and bimetallic nanocatalysts. Although Ni/Vulcan sample has a lower nickel loading of 1.4% as compared to NiPt/Vulcan having a total metal loading of 10% and 2% of it is composed of nickel, smaller particles on TEM images for bimetallic Vulcan XC 72R supported catalyst are observed. Numerically, TEM images in Figures 4.5 and 4.7 displays monometallic nickel nanoparticles with a diameter of ~6nm. On the other hand, the Figures 4.9 and 4.10 reveals that Vulcan XC 72R supported bimetallic nanocatalysts with a total metal loading of 10% and nickel loading of 2% are comprised of metal particles with the diameter values mostly below 3 nm! Two important observations were made on monometallic and bimetallic nanocatalysts prepared over Vulcan XC 72R. Firstly, although bimetallic nanocatalyst has a higher nickel loading, the particle size of PtNi/Vulcan as compared to Ni/Vulcan was smaller. Secondly, the narrow particle size distribution on Vulcan XC 72R was achieved. These observations can possibly be explained by the platinum islands acting as a kind of 'stabilizer' for the growth of nickel nanoparticles. Therefore, the nucleation of the nickel particles does not happen over the available active sites on the surface of the carbon support away from the platinum particles; instead, they grow around the previously adsorbed platinum particles.

As for the sample 'b' in Table 4.1 prepared over the Vulcan XC 72R support, it has a total metal loading of 1.1% and 1% of it is composed of Pt and the remaining 0.1% is Ni. Unlike to the sample 'a' with a total metal loading of 10% which might have a promising electrochemical activity, this sample 'b' was synthesized with a quite low loading and presented here as a sign of the lower limits of our capability in utilizing the SCFD technique for the preparation of supported bimetallic nanoparticles.

The Figure 4.11 displays the EDXS spectrum of PtNi/Vulcan with a total metal loading of 1.1%. The expected platinum to nickel weight ratio, according to gravimetric analysis, should be 1:10 (Ni:Pt). However, it was found to be ~1:20 according to chemical composition results obtained from EDX spectrum. Probably, some portion of nickel precursor which was adsorbed on the surface of Pt/Vulcan nanocatalysts volatilized during the reduction process. Since the adsorbed amount of nickel precursor was already quite low, the amount lost during the reduction process brings a relatively big difference in Pt:Ni ratio.

For the analysis of the success in preparing bimetallic, uniformly distributed supported low loading nanometals, the corresponding TEM images of PtNi/Vulcan with a total metal loading of 1.1% are given in Figures 4.12 and 4.13 and 4.14.

Figure 4.12 shows the large area TEM images. Most of the particles are observed to be around ~1nm with quite narrow particle size distribution. As can be seen from Figure 4.13, the metal loading is not uniform. This is probably caused by the extremely low amount of metal precursor placed in to the vessel. Better analysis of the particle size distribution can be seen on Figure 4.14. Extremely small spherical nanoparticles are observed.

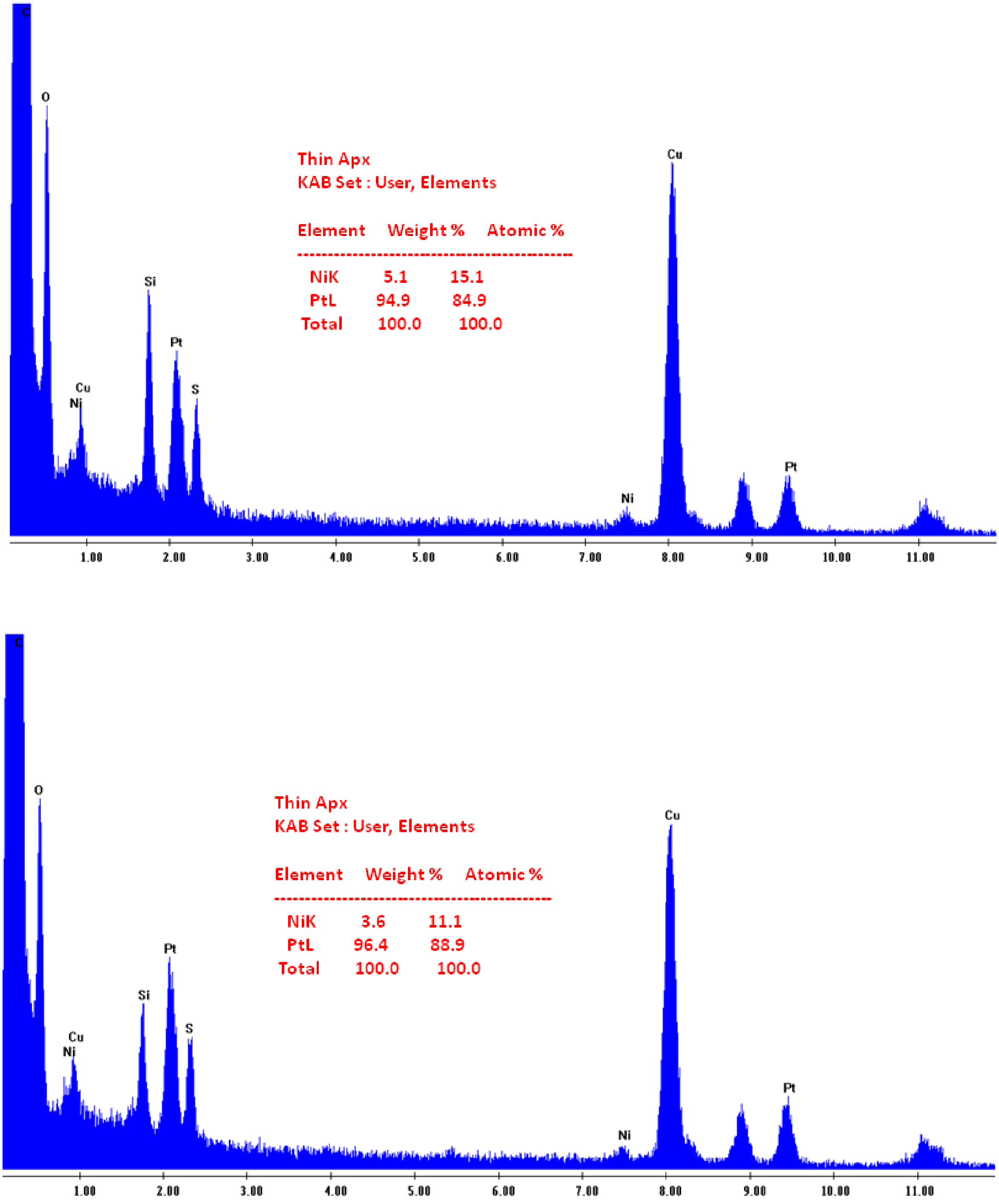

Thin Apx
KAB Set : User, Elements

Element	Weight %	Atomic %
NiK	5.1	15.1
PtL	94.9	84.9
Total	100.0	100.0

Thin Apx
KAB Set : User, Elements

Element	Weight %	Atomic %
NiK	3.6	11.1
PtL	96.4	88.9
Total	100.0	100.0

Figure 4.11 : The EDX spectrum of PtNi/Vulcan with a total metal loading of 1.1%

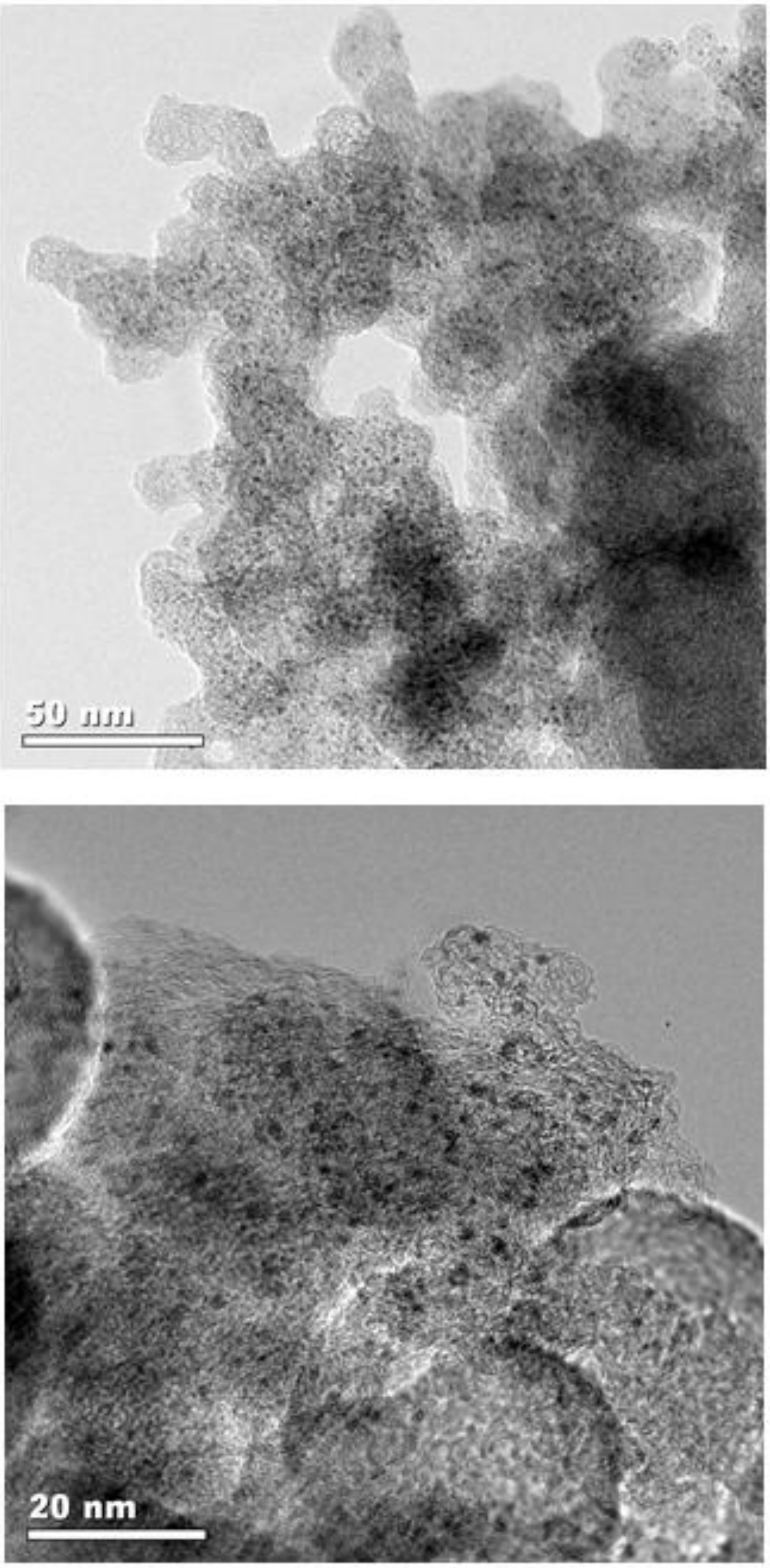

Figure 4.12: Large area TEM images of PtNi/Vulcan with a total metal loading of 1.1%

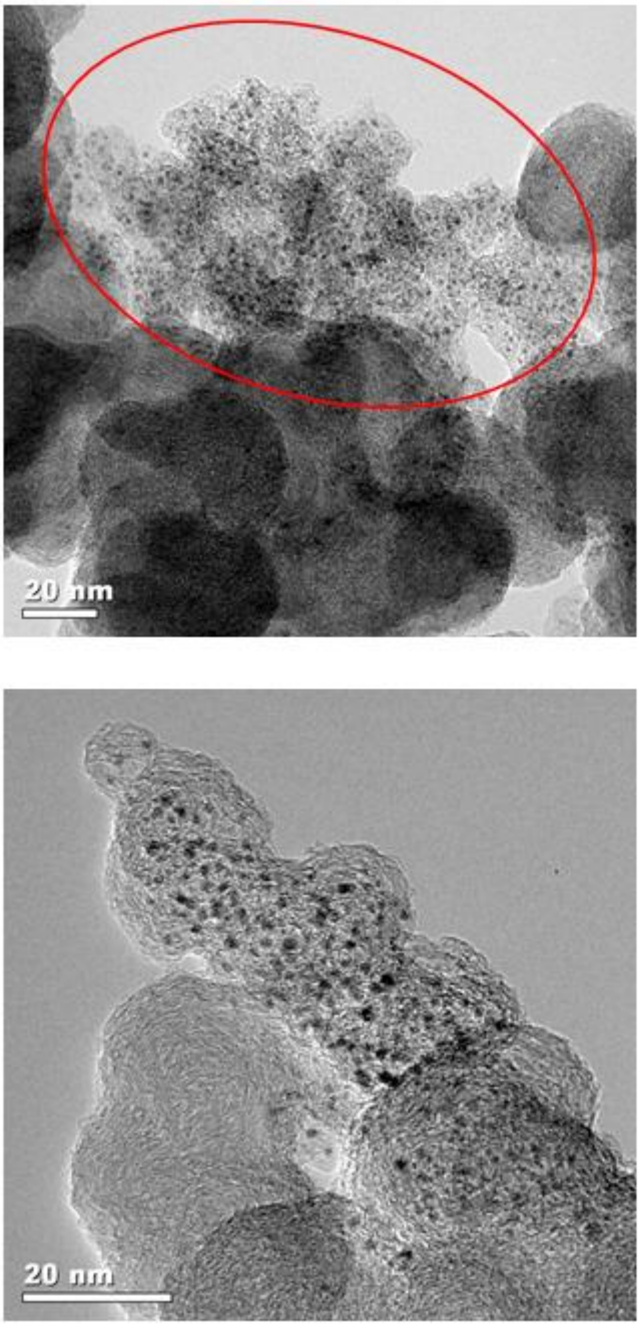

Figure 4.13: The figure shows the TEM images of PtNi/Vulcan with a total metal loading of 1.1% which are concentrated on support surface non-uniformly.

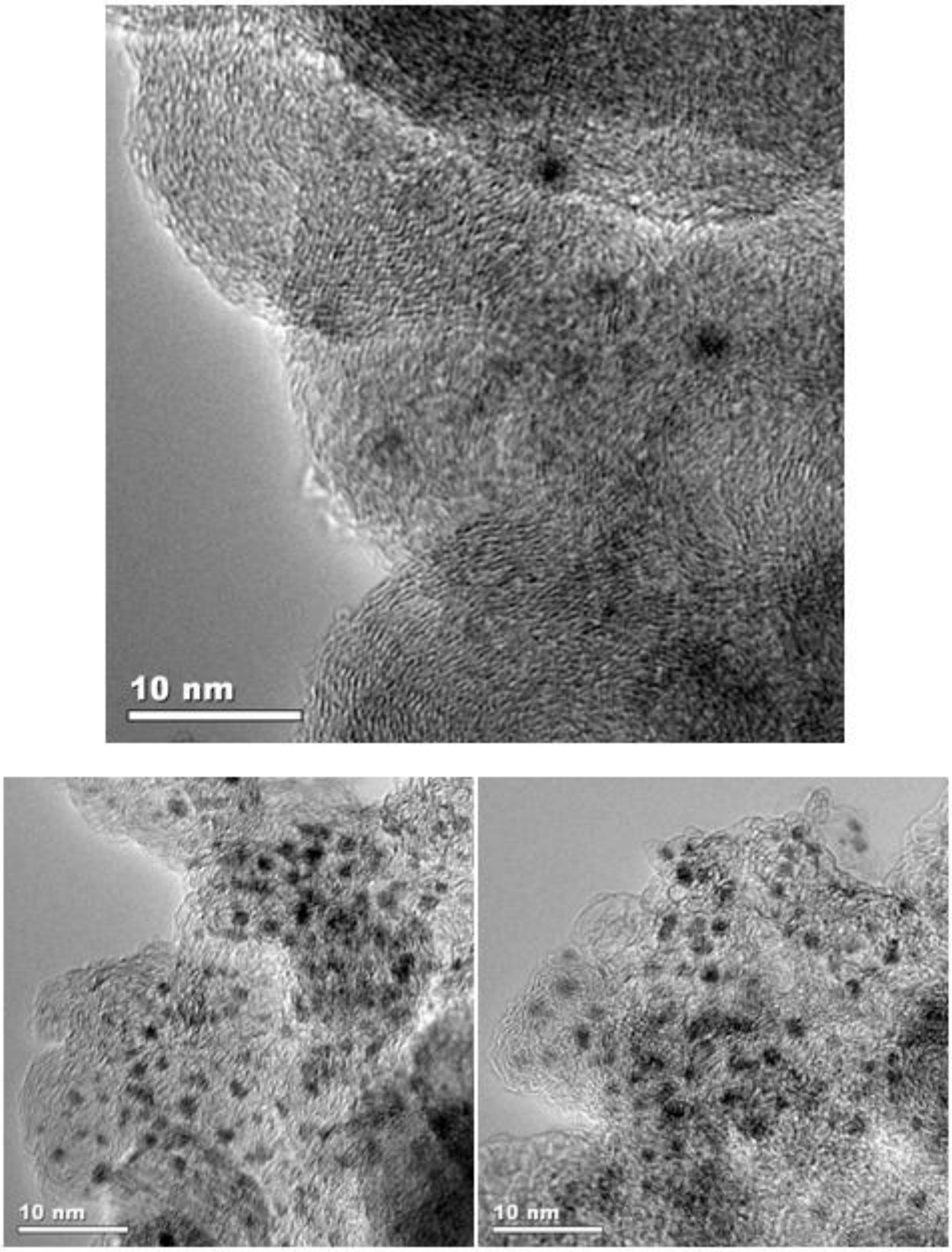

Figure 4.14: High magnification TEM images of PtNi/Vulcan with a total metal loading of 1.1%

Lastly, the third support, CA, was used for the preparation of supported monometallic and bimetallic nanocatalysts. The carbon aerogels with an average pore size of 22 nm were used. The TEM images of monometallic nickel nanoparticles are given in Figure 4.15

Large area and high magnification TEM images of Ni/CA in Figure 4.15 revealed that no big agglomerate formations were detected. Nanoparticles with a size less than 10 nm are observed which are analyzed to be pure nickel by EDXS measurements.

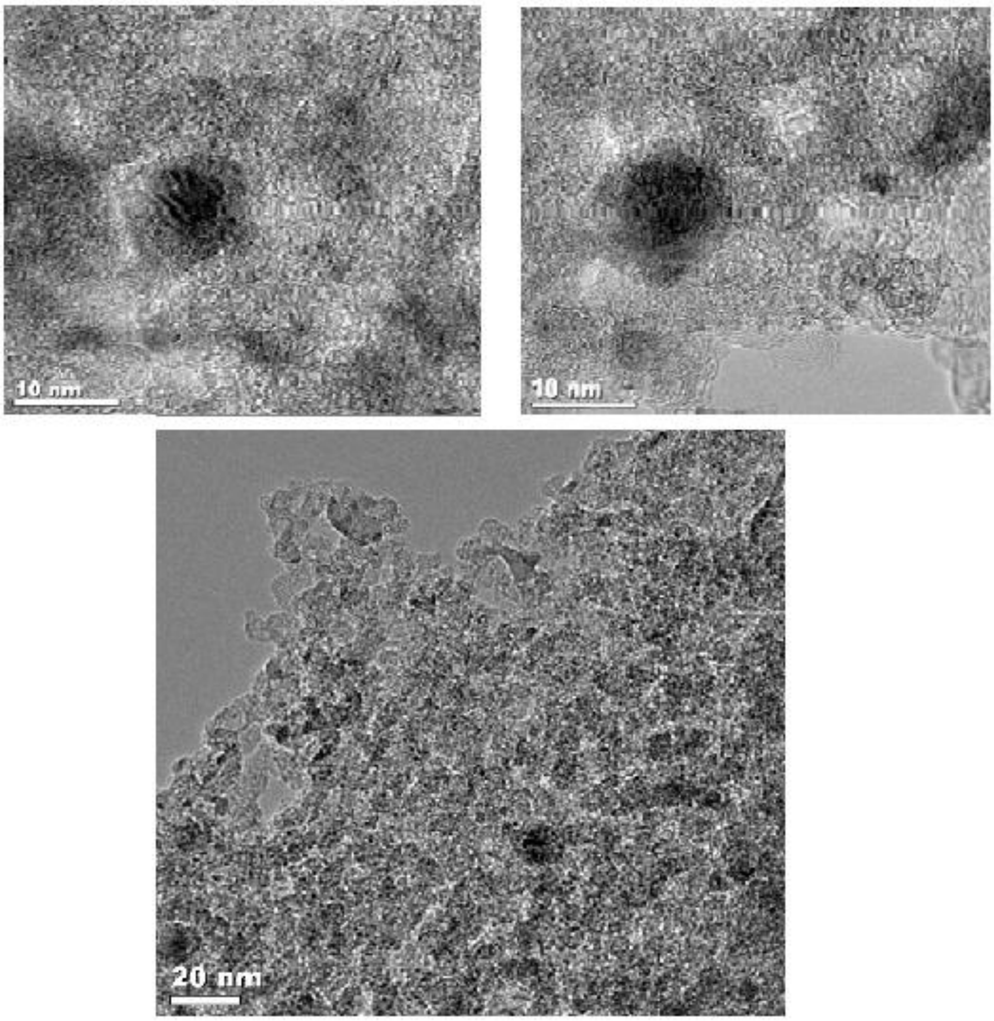

Figure 4.15: Large area and high magnification TEM images of Ni/CA nanocatalyst with a nickel loading of 3.5%

In addition to the monometallic Ni/CA samples, the bimetallic samples over CA support were prepared and the loading details are given in Table 4.1. The effect of the nickel incorporation into Pt/support composite and the effect of deposition order (sequential impregnations of Pt and Ni) on morphology and activity were studied. The samples'd' was prepared by changing the deposition order: supported nickel nanoparticles over CA support synthesized and this was followed by the incorporation of platinum.

It was found in Section 4.1 that, in this study, CA is the support with the highest total surface area, ~747 m^2/g. This is the most likely reason for XRD analysis to be inconclusive. The high available surface area of CA let the deposited particles to spread freely over the surface, instead of coming together and forming relatively bigger particles. Scherer's Equation states that as the particle size decreases, the expected XRD peaks should become broader. When this is combined with the background XRD spectra of quite amorphous CA, the detection of XRD peaks of either supported monometallic or bimetallic samples prepared over CA was not successful. Therefore, related understanding of the size distribution and morphology of the particles were acquired from corresponding TEM images.

The Figure 4.16 displays the EDXS spectrum of sample 'a' over CA with the metal loadings of 2.2%Pt and 1%Ni. It is worth to note that, similar to the PtNi/Vulcan with a metal loading of 8%Pt and 2%Ni, this sample 'a' on CA also shows small deviations in the chemical compositions for the large area measurements which was done by focusing on different areas of the specimen prepared for TEM analysis. This, again, implies homogenous distribution of nickel and platinum metals, instead of forming aggregates, at different areas, as separate platinum and nickel islands. Then, again, the two possible explanations are either nanoalloys of PtNi or core-shell structure with platinum being in core and nickel being in shell.

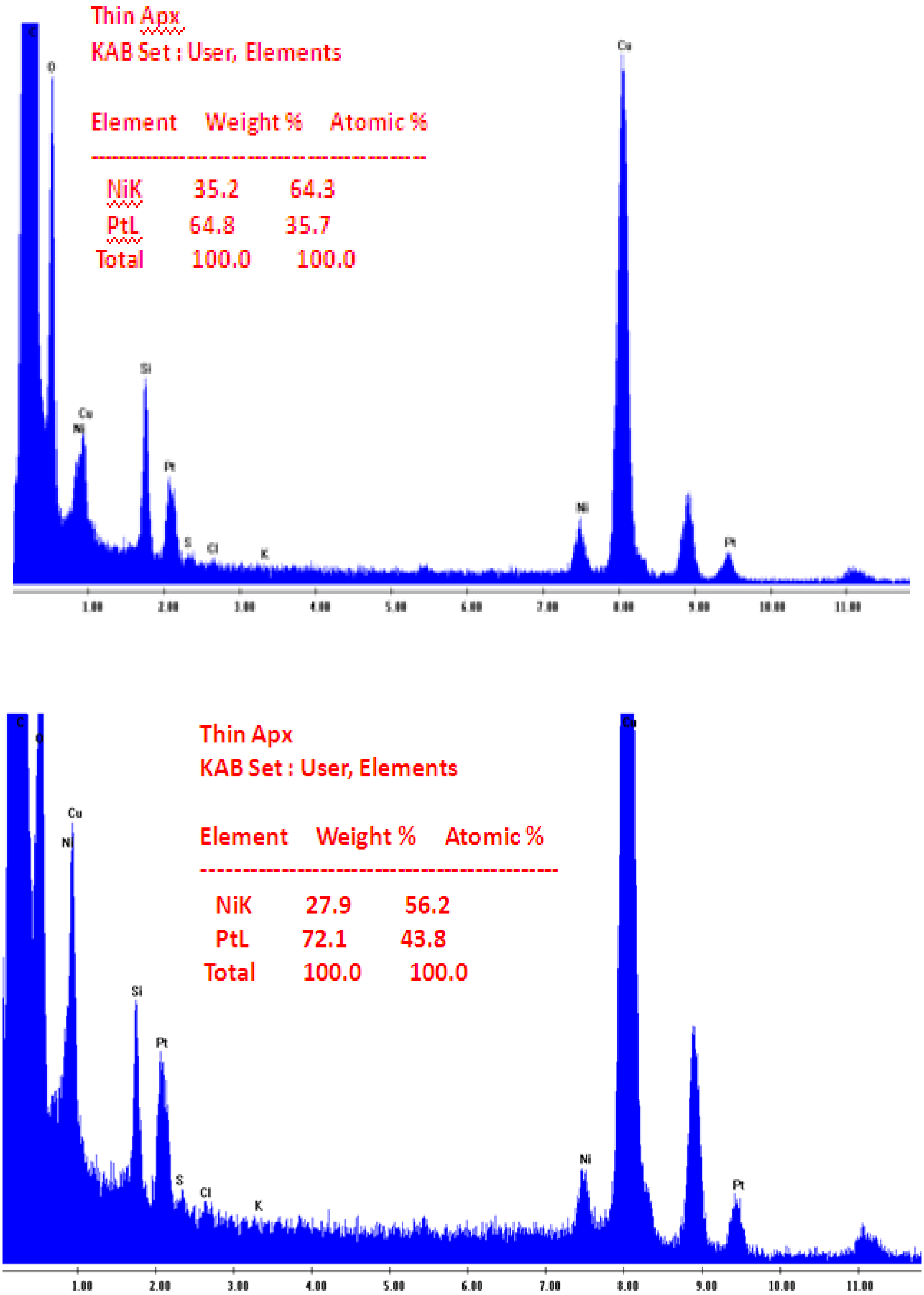

Thin Apx
KAB Set : User, Elements

Element	Weight %	Atomic %
NiK	35.2	64.3
PtL	64.8	35.7
Total	100.0	100.0

Thin Apx
KAB Set : User, Elements

Element	Weight %	Atomic %
NiK	27.9	56.2
PtL	72.1	43.8
Total	100.0	100.0

Figure 4.16: EDX spectrum and corresponding chemical composition results of PtNi/CA22 with the metal loadings of 2.2%Pt and 1%Ni with Pt deposition first.

The Figure 4.17 and 18 displays the TEM images of sample ‘a’ over CA with the metal loadings of 2.2%Pt and 1%Ni. The particle size is extremely small almost beyond the resolution limits of TEM (less than 1nm) but particle population is high with quite even distribution. When treated together, The EDX results and TEM results are quite interesting that extremely small supported nanoparticles are prepared with a high amount of nickel content in the bimetallic composites (at atomic base, approximately, 60% nickel and 40%platinum). This is a clear sign for the power of our abilities in utilizing SCFD for synthesize of supported homogeneous bimetallic nanoparticles.

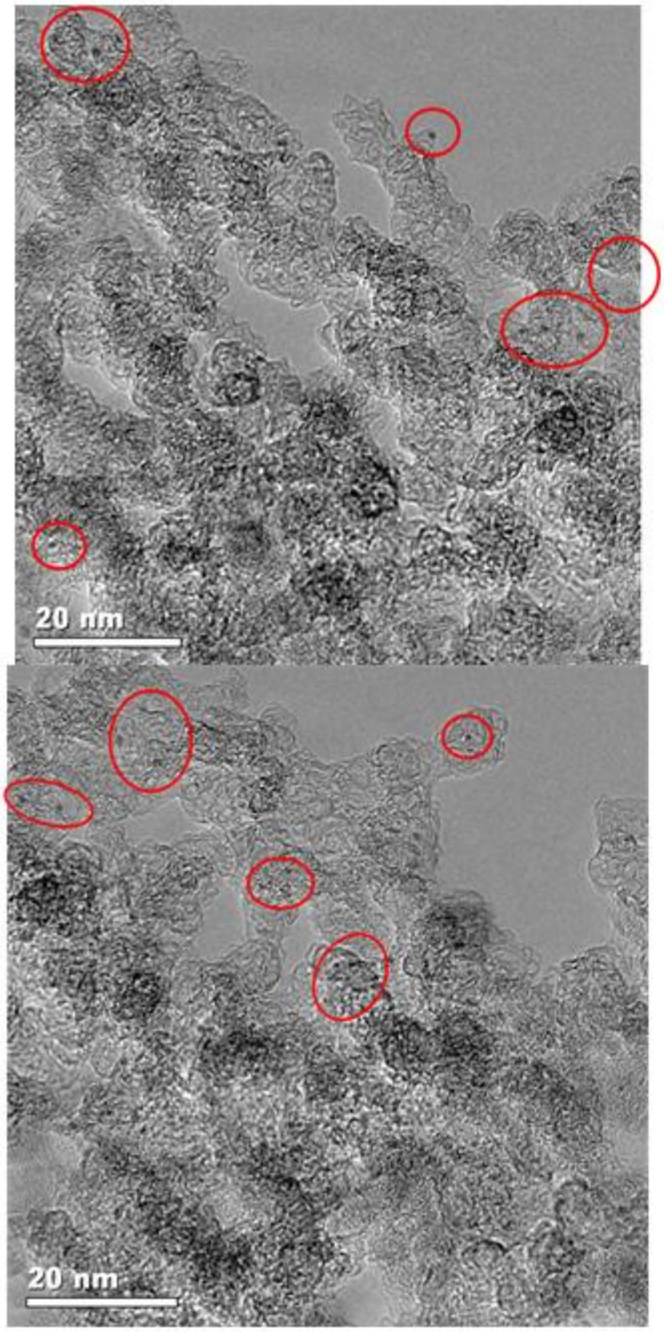

Figure 4.17: TEM images of PtNi/CA22 with the metal loadings of 2.2%Pt and 1%Ni with Pt deposition first.

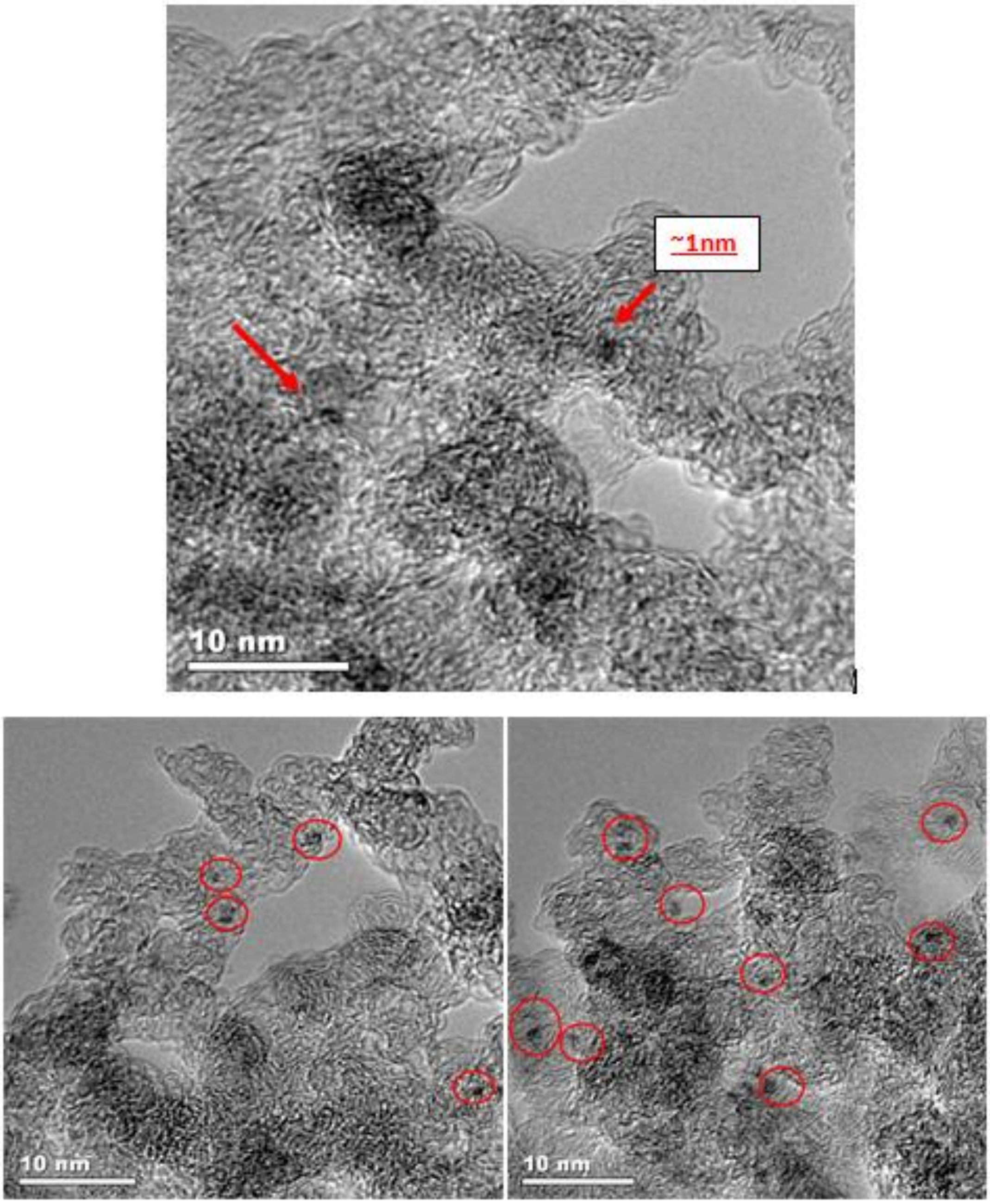

Figure 4.18: High magnification TEM images of PtNi/CA22 with the metal loadings of 2.2%Pt and 1%Ni with Pt deposition first.

Regarding the uniformly distributed metal content and narrow particle size distribution around ~1nm, similar results were obtained for the sample ‘b’ with the metal loadings of 4%Pt and 0.2%Ni over CA (See Figure 4.19). The nickel content of the prepared nanoparticles was found to be around 15% at atomic base, with a uniform distribution.

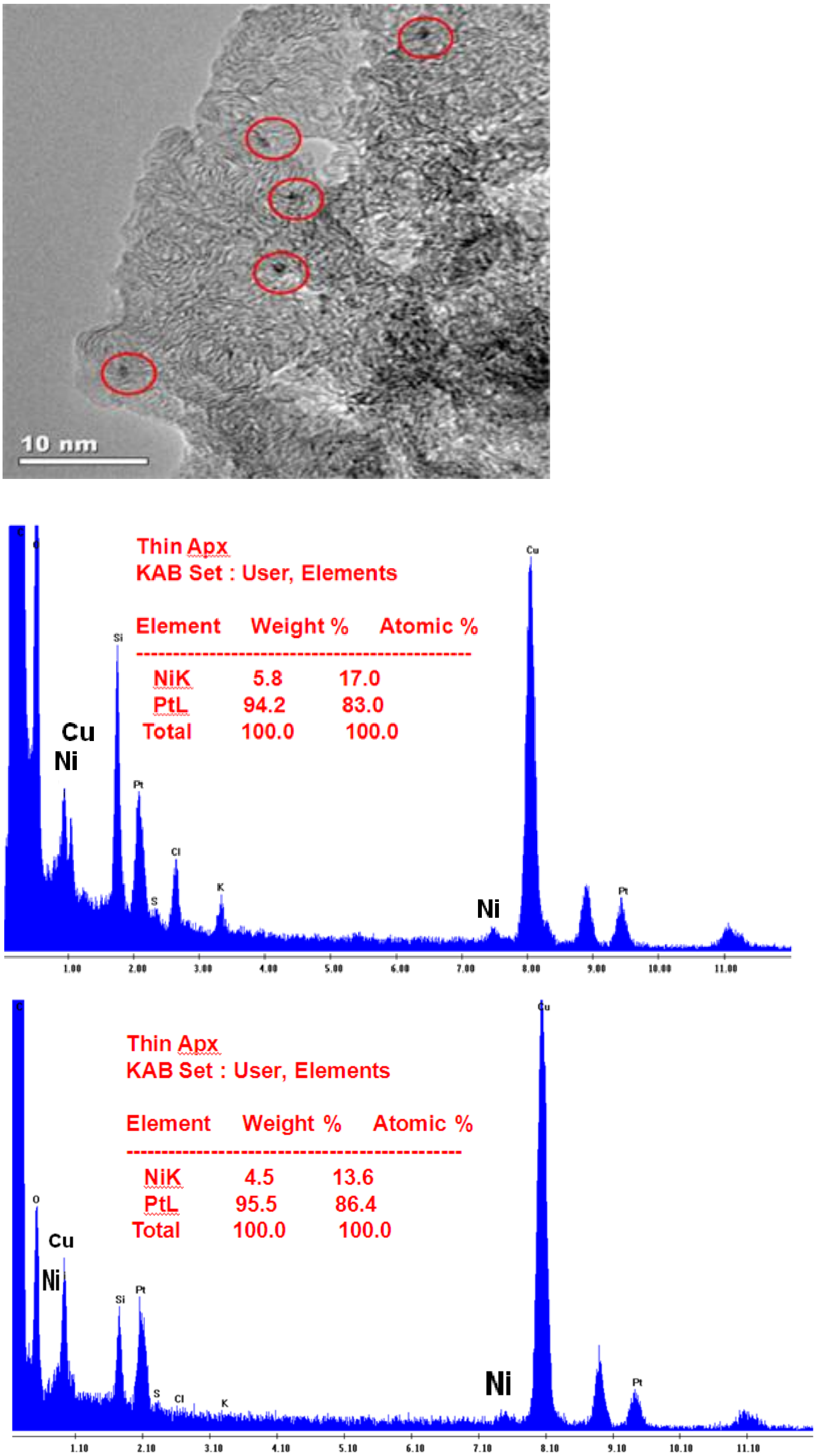

Element	Weight %	Atomic %
NiK	5.8	17.0
PtL	94.2	83.0
Total	100.0	100.0

Element	Weight %	Atomic %
NiK	4.5	13.6
PtL	95.5	86.4
Total	100.0	100.0

Figure 4.19: TEM image and EDX results for PtNi/CA with a metal loading of 4%Pt 0.2%Ni with Pt deposition first.

The Figure 4.20 below illustrates the TEM images and also EDXS results of PtNi/CA sample with a metal loading of 4%Pt 2%Ni with Pt deposition first. No big agglomerate formations were seen with narrow particle size distribution around 1-3 nm. Similar to the results obtained for bimetallic PtNi on Vulcan XC 72R and on alumina samples, PtNi/CA samples also exhibit a smaller particle size than monometallic Ni on CA. These observations strengthen the idea of possible stabilization effect of Pt on Ni atoms agglomeration.

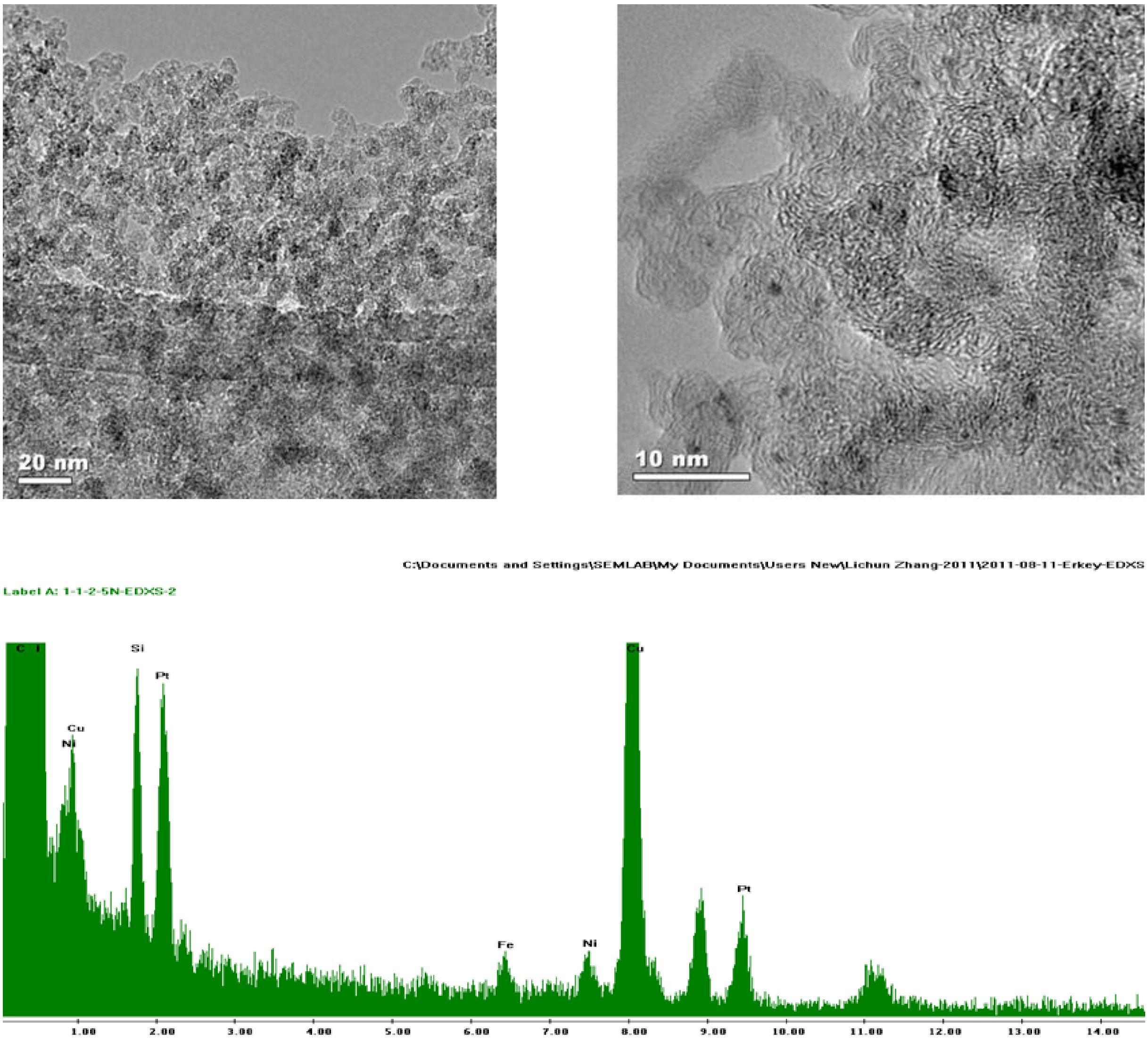

Figure 4.20: TEM image and EDX results for PtNi/CA with a metal loading of 4%Pt 2%Ni with Pt deposition first.

The following Figures of 4.21, 4.22 and 4.23 below shows the TEM images and EDXS results for bimetallic PtNi/CA nanocatalyst with a metal loading of 3.6%Pt 3.5%Ni with Ni deposition first. Quite interesting results are obtained. Some large particles with a size of 10-20 nm are confirmed to be pure Ni, while some small nanoparticles of 1-3 nm in size are also observed and confirmed to be bimetallic PtNi. It can possibly be suggested that since Ni deposition is achieved prior to the Pt addition, Ni atoms segregation were not inhibited this time. Slight portion of the Ni atoms interect with Pt and formed the bimetallic nanoparticles of 1-3 nm in size, but, mainly previously deposited Ni atoms are seen to form bigger agglomerates during the formation of Pt nanoparticles from Pt(COD)Me_2 which requires heat for the ligands removal. Actually, this portion of heat gives a further mobility to the previously deposited Ni nanoparticles and forced them to from 10-20 nm particles in size.

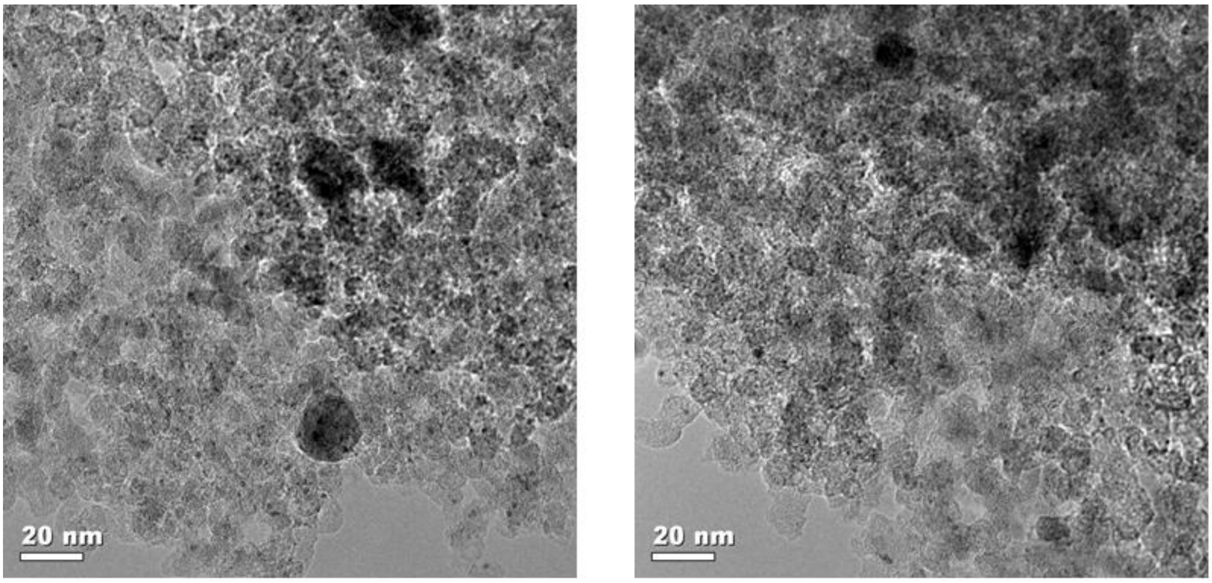

Figure 4.21: TEM images for bimetallic PtNi/CA nanocatalyst with a metal loading of 3.6%Pt and 3.5%Ni with Ni deposition first.

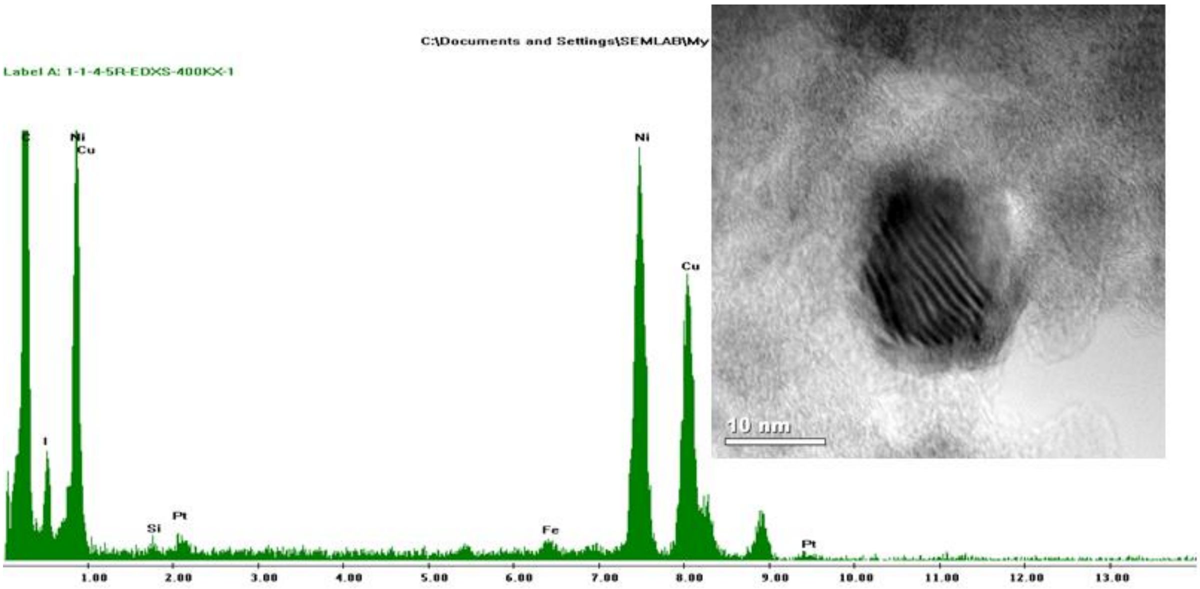

Figure 4.22: TEM image and EDX results for big particles (pure Ni) of bimetallic PtNi/CA nanocatalyst with a metal loading of 3.6%Pt 3.5%Ni with Ni deposition first.

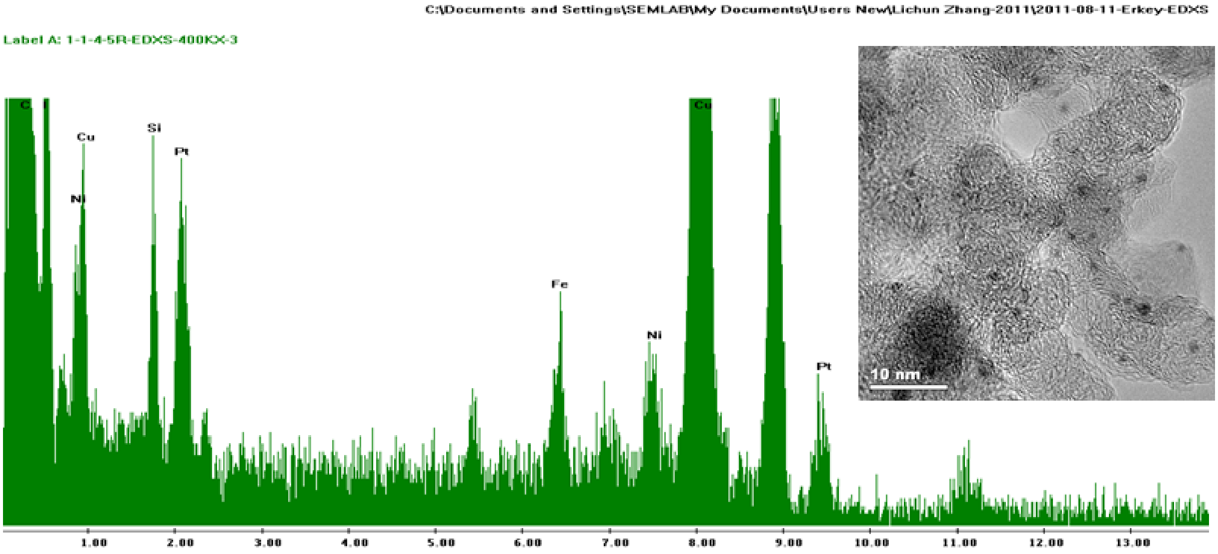

Figure 4.23: TEM image and EDX results for small particles of bimetallic PtNi/CA nanocatalyst with a metal loading of 3.6%Pt 3.5%Ni with Ni deposition first.

4.3. Electrochemical Activity Tests of Monometallic Pt and Bimetallic Pt-Ni Nanoparticles

Electrochemical activity tests of the prepared catalysts were studied by HOR and ORR measurements. Regarding the carbon supports, one of the objectives of this study is to synthesize electrochemically active nanosized supported bimetallic catalysts with a quite low loading which would make the fuel cell applications less expensive. Analysis of the systematically arranged electrochemical activity tests' results together with the comparison of the activities of the monometallic catalysts is provided.

Table 4.2 displays the total and electrochemically active surface area (ESA) of the deposited platinum nanoparticles. Total surface area was calculated based on the diameter of the particles observed from TEM images with a narrow size distribution. ESA values were calculated by using Equation (1) where A is the area under the reduction part including the double layer capacitance (DLC) part of the curve, $K=0.21 mCcm^{-2}Pt^{-1}$, S is set to be scan rate (50mV/s) and platinum loading on the electrode is designated by L.

$$ESA= A / (K.L.S) \qquad (1)$$

Normally, DLC part of the curve is to be excluded for such calculations, however, as can be seen from Figures 4.24 and 4.26, deposited Pt nanoparticles were found to be very active in oxidizing the surface groups on CA and thereby the huge increase in DLC part makes some portion of the hydrogen reduction curve invisible. In other words, while the metals on the surface of CA are so dilute, the surface is mainly populated by the oxygen containing species. The XPS spectrum for the confirmation of the oxygen containing surface groups on CA is given in Figure 4.24

Table 4.2: Electrochemical and the total surface of 4%Pt/CA catalyst.

Catalyst	**d_{TEM}(nm)**	**SA_{Pt} (m2/g)**	**ESA_{Pt}**	**%Pt utilization**
(4%Pt)/CA	~1nm	279	195	~70

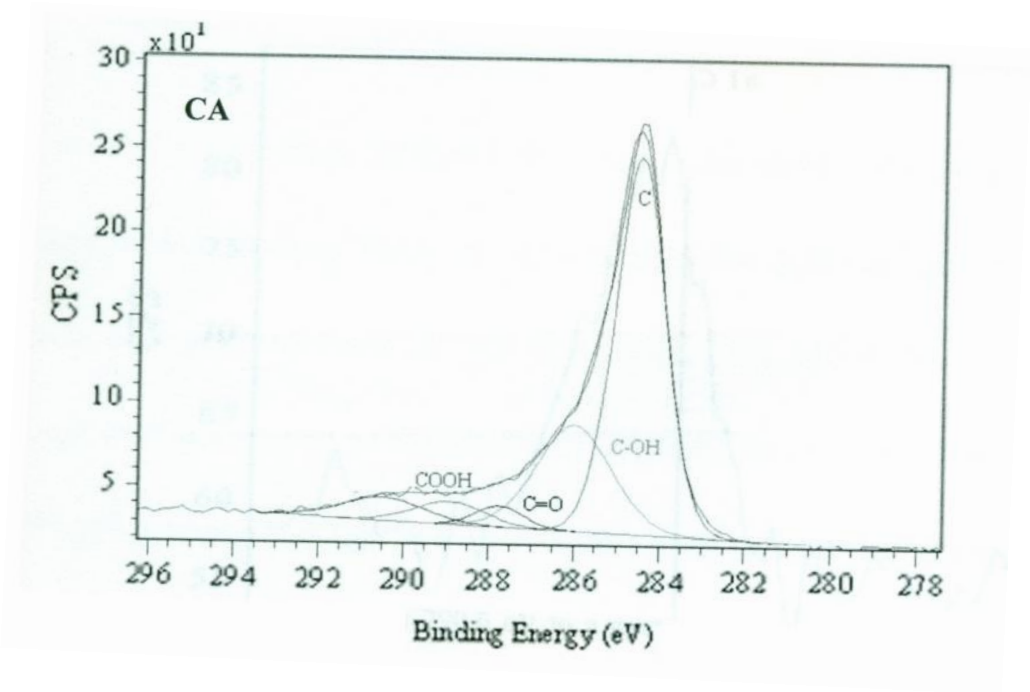

Figure 4.24: Curve fitting results of C1s spectra of CA, *adapted from* [66].

In Figure 4.24, sharp-asymmetric peak is observed around 284.5 eV. The shoulders making the peaks asymmetric are observed towards higher binding energy values and when combined with curve fitting results, this is an indication of the oxygen containing surface groups of CA.

The figure 4.26 shows the CV results at the first and fiftieth cycles of the monometallic Pt catalyst with 4% Pt loading and bimetallic PtNi catalyst with 2% Ni addition supported on CA. To see how Pt accelerates the increase in the DLC, corresponding CV results of pure CA is also provided. Hydrogen adsorption desorption peaks (H_2-ads/des) are observed around 0-0.2V. Similar to the results obtained in the literature, nickel addition decreases the ESA of the prepared catalysts [67] (See Figure 4.25 below).

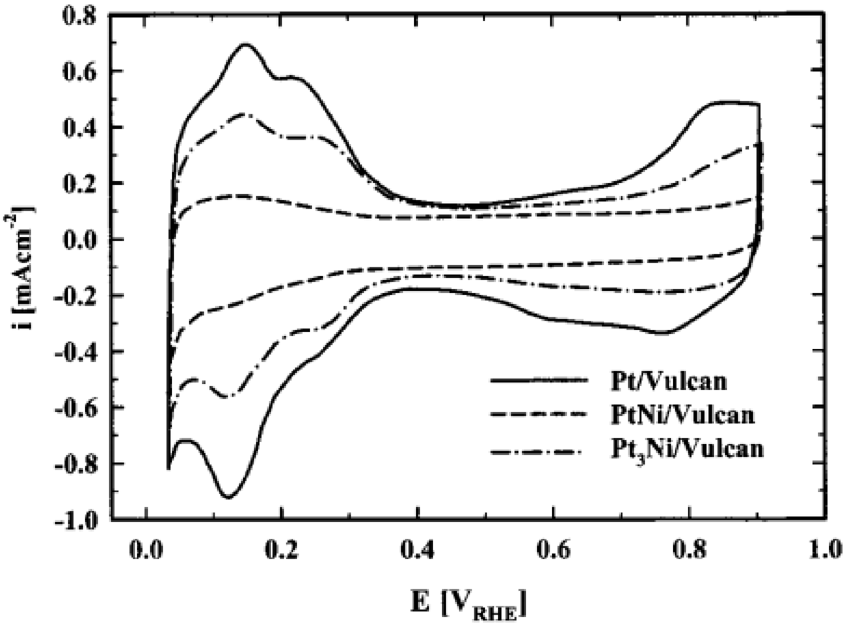

Figure 4.25: The Figure shows the decrease in the ESA value for increased amount of Ni in carbon supported PtNi alloy, *taken from* [67]

The oxidation of Pt should be visible after 50 cycle HOR treatment; however, this was not the case which is attributed to the huge DLC. The Figure 4.27 shows that as the number of the cycles increases, the CV of supported bimetallic PtNi catalyst starts to mimic the CV of supported monometallic Pt catalyst which is probably an indication of the dissolution of nickel.

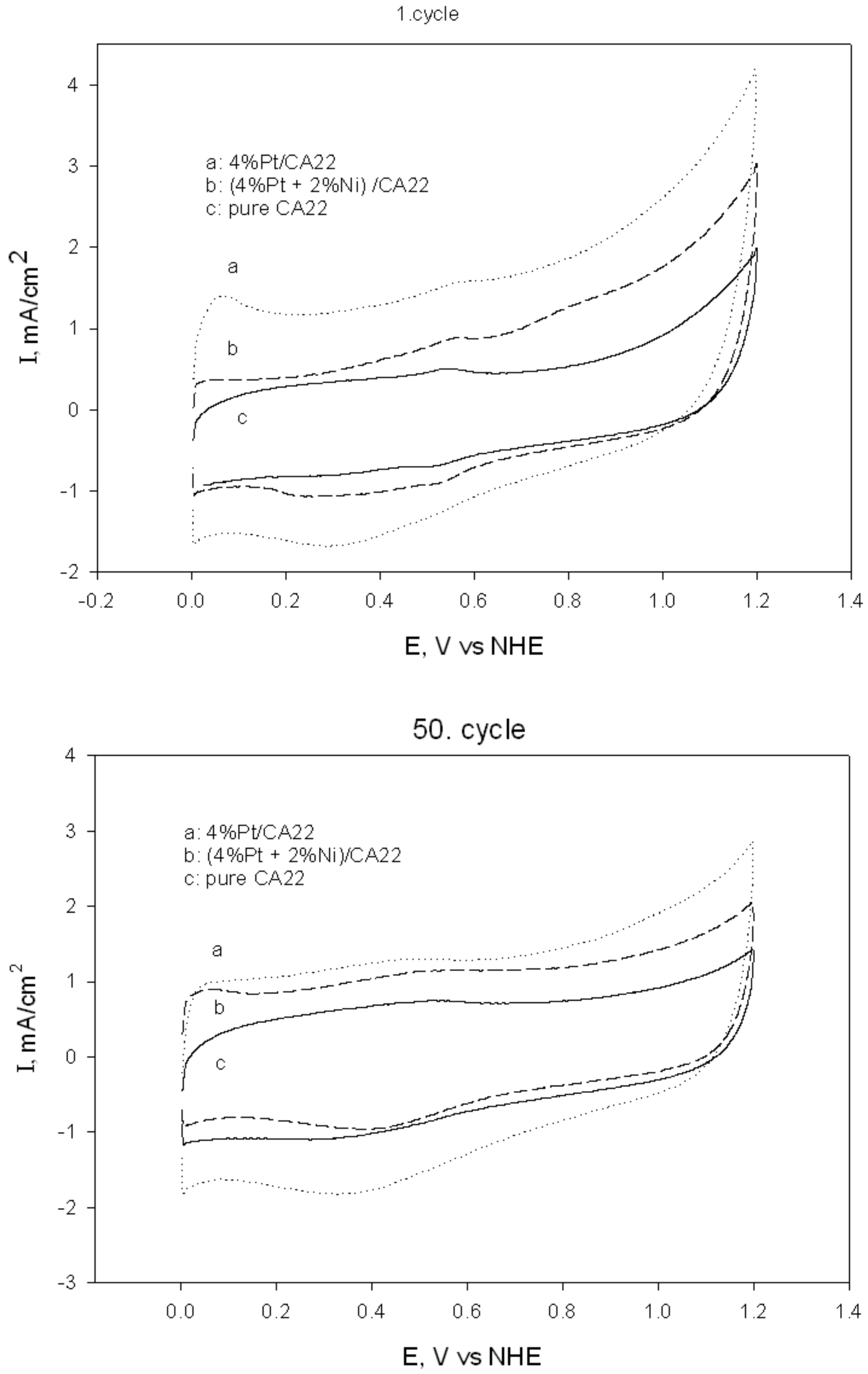

Figure 4.26: CV curves at first (top) and fiftieth (bottom) cycles for pure CA, (4%Pt)/CA, and (4%Pt + 2%Ni)/CA in 0.1MHClO$_4$ at a sweep rate of 50mV/s.

In Figure 4.27, CV results of (4%Pt+2%Ni)/CA for higher number of cycles are given. The increase in the ESA becomes more pronounced when the number of the cycles increased. When combined with the previous results, this may imply that previously deposited platinum nanoparticles were surrounded by the nickel metal resulting in a core-shell structure with platinum being at core and nickel at shell. One may suggest that increasing HOR cycles hinders the dissolution of nickel from the shell and resulting free sites of platinum become active sites for hydrogen adsorption. Subsequently, ESA is observed to increase with the increasing in the number of HOR cycles. However, it is still possible that the Pt-Ni alloys were formed and when the dissolution of the nickel from the bimetallic alloy occurred, higher ESA was obtained. Therefore a definite core-shell structure can't be suggested at this stage, without analyzing all the data presented on these samples.

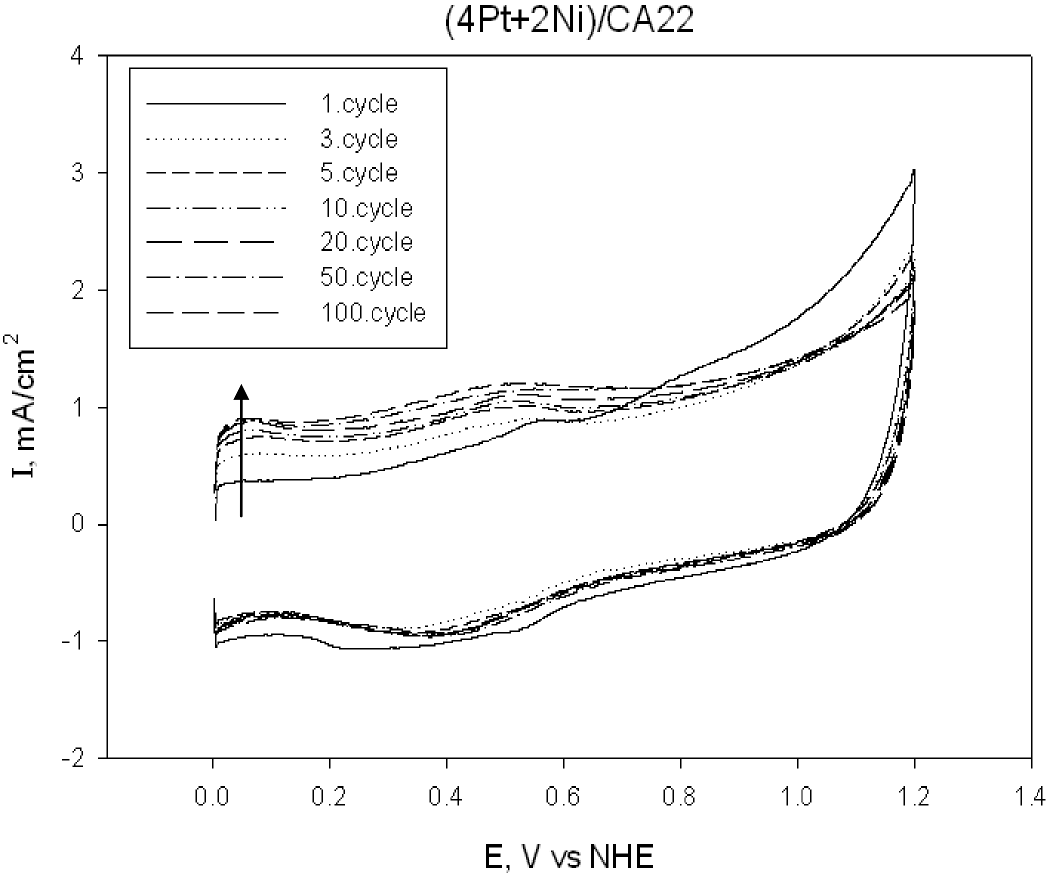

Figure 4.27: CV curves for (4%Pt + 2%Ni)/CA in 0.1MHCIO$_4$ at a sweep rate of 50mV/s. An arrow rises up with the increasing number of the cycles.

The Figure 4.28 displays the hydrodynamic voltammograms of positive scans for ORR of PtNi catalyst with a loading of 4%Pt and 2%Ni supported on CA. The rotation speeds studied are 100, 400, 900, 1600 and 2500 rpm at a sweep rate of 10mV/s. To clean the surface, firstly 10 HOR cycles was carried out and peroxide (H_2O_2) formation was detected based on the Koutecky-Levich plot. Then the same procedure was followed with only difference of 50 cycles of HOR surface treatment and H_2O_2 formation was still found. It was observed that if the surface was cleaned further by HOR cycles of more than 50, then the corresponding ORR activities were start to decrease. Therefore, prior to all ORR measurements in this study, the surface treatment was achieved by 50 HOR cycles.

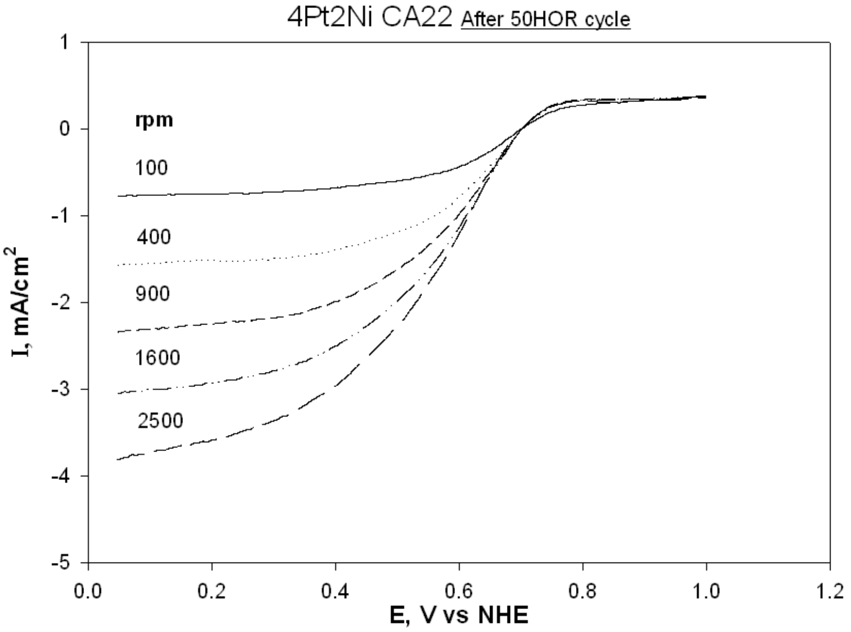

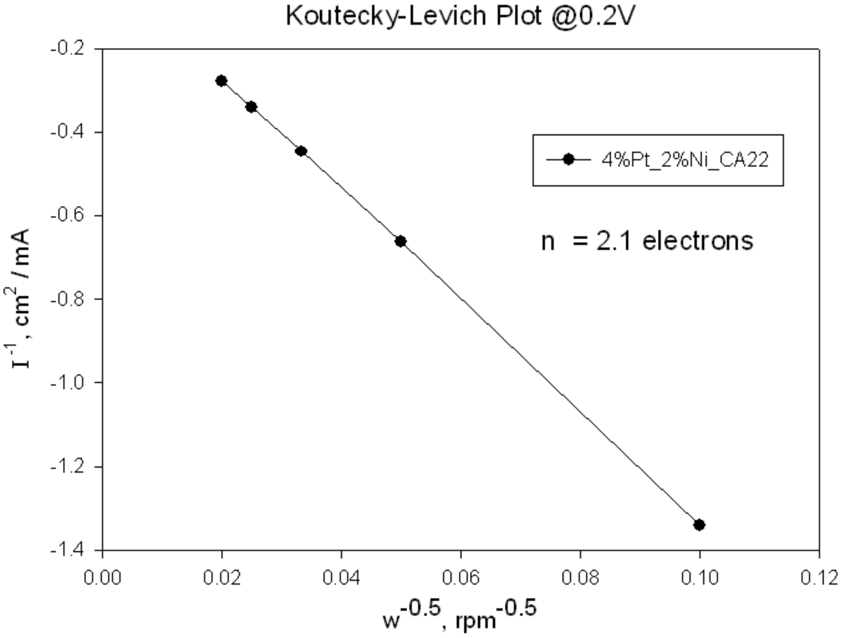

Figure 4.28: Hydrodynamic voltammograms of positive scans (top) and corresponding Koutecky-Levich plot (bottom) of (4%Pt + 2%Ni)/CA for O_2 reduction in O_2 saturated 0.1 M $HClO_4$.

It is shown that the limiting current increases with the increase in revolution speeds which is associated with the increase of the oxygen diffusion through the surface of an electrode. The little inclined behavior of the current plateau is explained by non-uniform distribution of the active sites [68]. This may be caused by the low metal loading which could not populate on the surface homogenously. Especially at low rpm values, the range of 0-0.3V is observed to be the diffusion controlled region. The region between 0.3-0.7V is the area that mixed diffusion-kinetic control with a function of the rotation speed becomes dominant. Finally, the values between 0.7-1.0V are the kinetics controlled range with an independency on rotation speeds. The diffusion controlled region for 2500 rpm is not shown which can be ascribed to the high rotation speed that hinders the oxygen diffusion up to the available limits and thereby overcoming the diffusion limitations. It is worth to note that the limiting current values obtained from the prepared catalysts are comparative with the state of the art catalysts and with the catalysts having a high metal content [69].

As for the explanation of H_2O_2 formation, it is possible that the oxygen containing surface species that dominates the CA surface change the reaction pathway severely in the mechanism of oxygen reduction reaction. Instead of 4-electron pathway (2), the peroxide pathway (3) was followed during the reaction:

$$O_2 + 4H^+ + 4e^- \rightarrow 2H_2O \qquad (2)$$

$$O_2 + 2H^+ + 2e^- \rightarrow H_2O_2 \qquad (3)$$

The reaction mechanism in ORR can be explained by Figure 4.29. Oxygen reduction can happen to form water directly with 4-electron pathway, with the rate constant of k1 or to form adsorbed peroxide, with the rate constant of k2. Then, the further reaction with the rate constant k3 may convert this adsorbed peroxide into water. Another possibility is the chemical decomposition with the rate constant k4. The adsorbed peroxide may also desorb from the surface towards the electrolyte solution of 0.1M $HClO_4$.

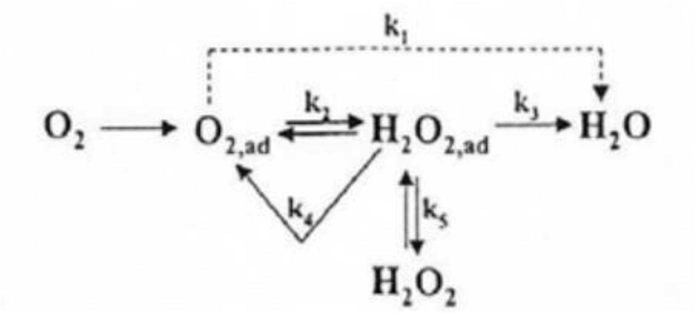

Figure 4.29: ORR mechanism on Pt, *reprinted from* [70]

In more details, ORR mechanism on Pt surface may happen by two different ways: dissociative or associative mechanisms [71]. On dissociative mechanism, adsorption of oxygen breaks O-O bonds. Therefore, adsorbed O_2 on Pt surface is not present which restricts the formation of H_2O_2. This cannot be the possible reaction scheme in our study.

$$1/2\ O_2 + * \rightarrow O* \tag{4}$$

$$O* + H^+ + e^- \rightarrow OH* \tag{5}$$

$$OH* + H^+ + e^- \rightarrow H_2O + * \tag{6}$$

The associative mechanism, on the other hand, enables the formation of H2O2. If the O-O bond of the adsorbed oxygen is not broken trough out the overall reaction mechanism, the formation of H_2O_2 is observed and if it is not reduced further to form H2O, then H2O2 is desorbed from the surface of the electrode as a final product which is the reaction shown with the rate constant of k5 in the Figure 4.29.

$$O_2 + * \rightarrow O_2* \tag{7}$$

$$O_2* + H^+ + e^- \rightarrow HO2* \tag{8}$$

$$HO_2* + H^+ + e^- \rightarrow H2O + O* \tag{9}$$

$$O* + H^+ + e^- \rightarrow OH* \tag{10}$$

$$OH^* + H^+ + e^- \rightarrow H_2O + * \quad (11)$$

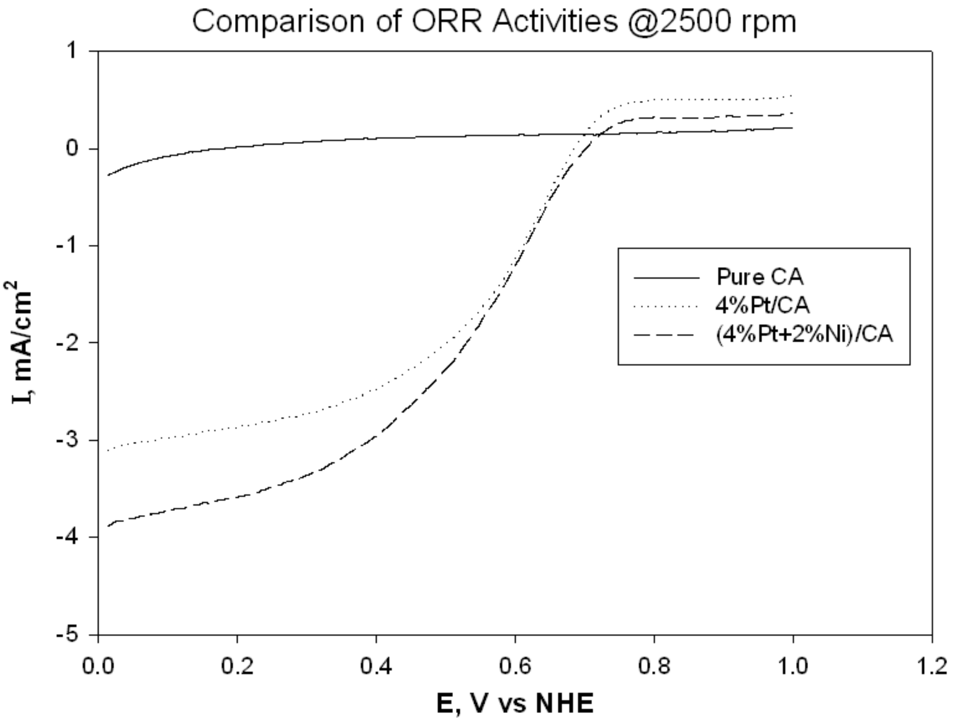

Figure 4.30: The figure comparatively shows the hydrodynamic voltammograms of positive scans of pure CA, (4%Pt)/CA, and (4%Pt + 2%Ni)/CA for O_2 reduction in O_2 saturated 0.1 M $HClO_4$.

To explain how Pt and Ni addition accelerates the ORR on CA, the Figure 4.30 is provided. As expected, almost no ORR occurs on pure CA. Small limiting current value probably belongs to the oxidation of the surface groups. It is clear that the deposition of Pt nanoparticles hinders ORR. In addition, the efforts to couple / alloy Pt with Ni are worth to study, since Ni addition is shown to increase the ORR activity of the prepared 4%Pt/CA catalyst by approximately 33%. Thereby, the so-called promotion effect is shown to be correct. Similar results were found in the literature [61, 72-74]. Paulus and co-workers stated that bimetallic Pt-Ni nanoparticles ~4nm display greater activity than monometallic Pt catalysts for ORR [69]. In more details, improvements in ORR activity achieved by bimetallic PtNi nanocatalysts as compared to the monometallic Pt can possibly be explained by the followings: the Pt electronic structure is modified together with modifications in its geometric structure; also static oxygen adsorbates are inhibited and also overpotential is reduced.

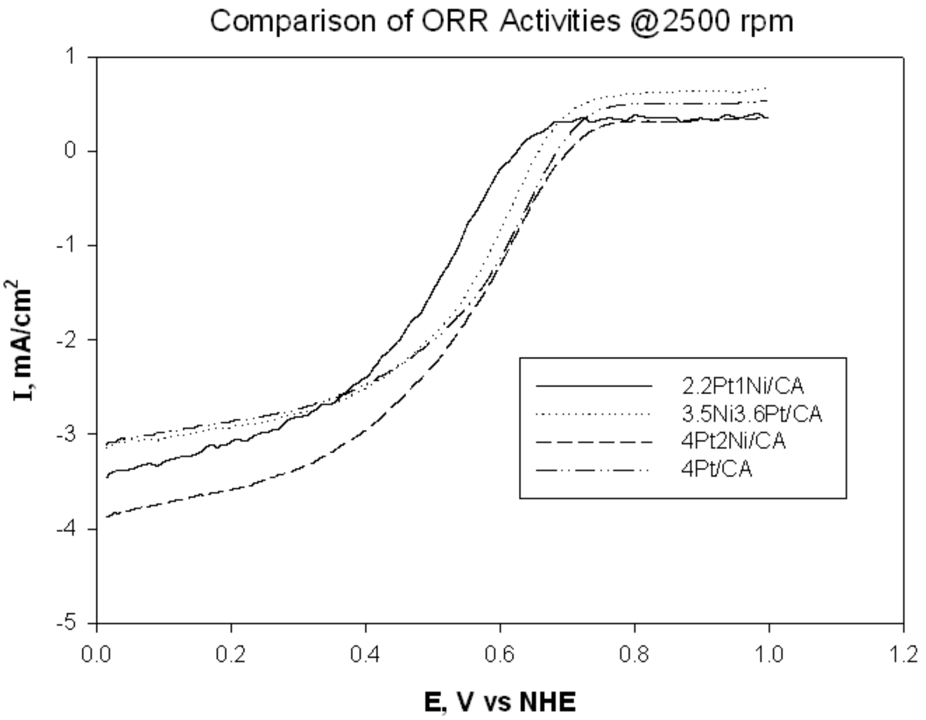

Figure 4.31: The figure comparatively shows the hydrodynamic voltammograms of positive scans of (2.2%Pt + 1%Ni)/CA, (4%Pt + 2%Ni)/CA, and (3.5%Ni + 3.6%Pt)/CA for O_2 reduction in O_2 saturated 0.1 M $HClO_4$.

Two important interpretations can be obtained from Figure 4.31 displaying the comparison of ORR activities of (2.2%Pt + 1%Ni)/CA, (4%Pt + 2%Ni)/CA, and (3.5%Ni + 3.6%Pt)/CA at 2500 rpm: possible core-shell structure of the prepared nanocatalysts, and the effects of the surface of CA on ORR activity. It is observed that the hydrodynamic voltammogram of (3.5%Ni+3.6%Pt)/CA catalyst highly resemble the hydrodynamic voltammogram of 4%Pt/CA. It can be suggested that since the nickel addition was followed by the incorporation of the platinum for (3.5%Ni+3.6%Pt)/CA catalyst, the core-shell structure with 3.6%Pt being at the shell occurred. The ORR activity of 4%Pt/CA which is very close to (3.5%Ni+3.6%Pt)/CA catalyst also supports this argument. It is interesting to note that the nickel metal which is loaded in the core brings almost no improvement to ORR activity. However, when combined with the corresponding TEM and EDXS results, core-shell is not the proposed structure (See Figures 4.21, 4.22, 4.23). Ni atoms do not stay at the core, instead they form separate pure Ni nanoparticles of 10-20 nm in size. Another important observation is the difference in the ORR activities of (2.2%Pt + 1%Ni)/CA and (4%Pt + 2%Ni)/CA catalysts which have almost the same Pt:Ni ratios. Recalling that the total metal loading on glassy carbon is fixed at 10μg/cm^2 and the Pt:Ni ratios of two catalysts are almost same, the difference in ORR activities of these two catalysts is not expected. Only difference in the preparation is the amount of the metal/support composite used in the ink, since the total metal loading values differ. Subsequently, the amount of the carbon in two inks is different, too. This can be the possible explanation of the differences in the ORR activities of (2.2%Pt + 1%Ni)/CA, (4%Pt + 2%Ni)/CA catalysts.

The Figure 4.32 is provided showing the CV results of (4%Pt + 2%Ni)/CA and (3.5%Ni + 3.6%Pt)/CA. Neither the total metal nor the platinum loading values differ too much for two different catalysts, but the difference in the corresponding ESA values is high. This figure can be related with the structure of the synthesized catalysts. The sample (3.5%Ni + 3.6%Pt)/CA was prepared by nickel addition on CA which was followed by platinum incorporation that may result in the core-shell structure with platinum being at the shell and thereby with higher ESA value. However, again, when combined with EDXS results, it is seen that core-shell structure is not the possible one, instead, pure Ni agglomerates are formed. As for the sample b in Figure 4.32, there are almost no H_2-ads/des curves appearing that can be explained by the nickel metal surrounding the previously deposited platinum islands and ceasing hydrogen adsorption on the prepared metal cluster. For this sample ‘b’, it is not clear enough whether nanoalloys have formed with certain degree of alloying or core-shell structures with Ni at the shell is formed. Possibly, segregation of small Ni atoms appears on previously deposited Pt islands and blocks ESA (See Figure 4.34, the second illustration from left). It is also observed that the increase in the DLC is higher for (3.5%Ni + 3.6%Pt)/CA catalyst in which more free Pt sites exist and oxidize the oxygen containing surface groups resulting in a huge increase DLC.

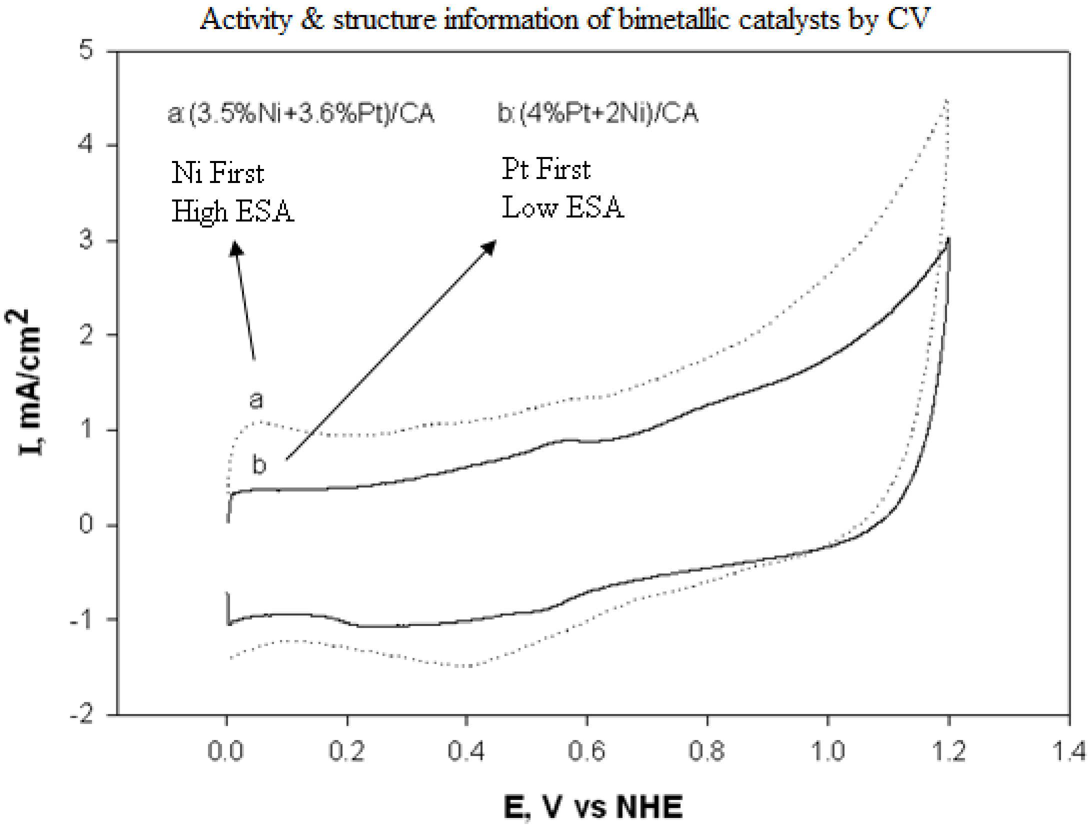

Figure 4.32: CV curves for (4%Pt + 2%Ni)/CA and (3.5%Ni + 3.6%Pt)/CA in 0.1MHClO$_4$ at a sweep rate of 50mV/s. Corresponding core-shell structures are given at the top left and top right for nickel at core and for platinum at core, respectively.

Regarding the activity results and structure information of the catalysts, if shell of nickel totally surrounds the Pt core, then an increase in ORR activity would not expected! Therefore, the bimetallic PtNi structure of **‘d’** given in Figure 4.33 is proposed with nickel atoms segregating on the Pt islands and thereby decreasing the ESA values but by the help of electronic effect, on the other hand, increasing the ORR activity. Since variation in EDX results were low, ‘a’ in Figure 4.33 (Pt atoms – Ni atoms phase separation) is not possible. And the configuration in ‘b’ (no phase separation but no close interaction between Pt-Ni atoms) would not decrease the ESA value since nickel atoms do not block the available Pt sites for this configuration. And the configuration ‘c’ does not allow the electrolyte to diffuse to the Pt-core which would obviously decrease the ORR activity. The fifth possibility which is not shown in Figure 4.34 is the alloying. For (4%Pt + 2%Ni)/CA sample, the temperature at which Pt and Ni interacted is 160^{o}C which is the reduction temperature of secondly deposited

Ni. The temperature at which Pt and Ni interact for the sample (3.5%Ni + 3.6%Pt)/CA, on the other hand, is 200°C which is the reduction temperature of secondly deposited Pt. If higher temperature value of 200°C caused the (3.5%Ni + 3.6%Pt) to form an alloy on CA, then based on the comparative ORR results in Figure 4.31 it can be stated that alloying dos not results in bimetallic catalysts with a higher activity. (Pay attention that neither the Pt nor the total metal loadings for (4%Pt + 2%Ni)/CA and (3.5%Ni + 3.6%Pt)/CA change a lot). However, alloying would result in a change in the electronic environment of Pt that should affect the activity of (4%Pt)/CA. Then, very close ORR activities of (3.5%Ni + 3.6%Pt)/CA and (4%Pt)/CA would not be possible for an alloying. These state that (3.5%Ni + 3.6%Pt)/CA sample is not alloyed.

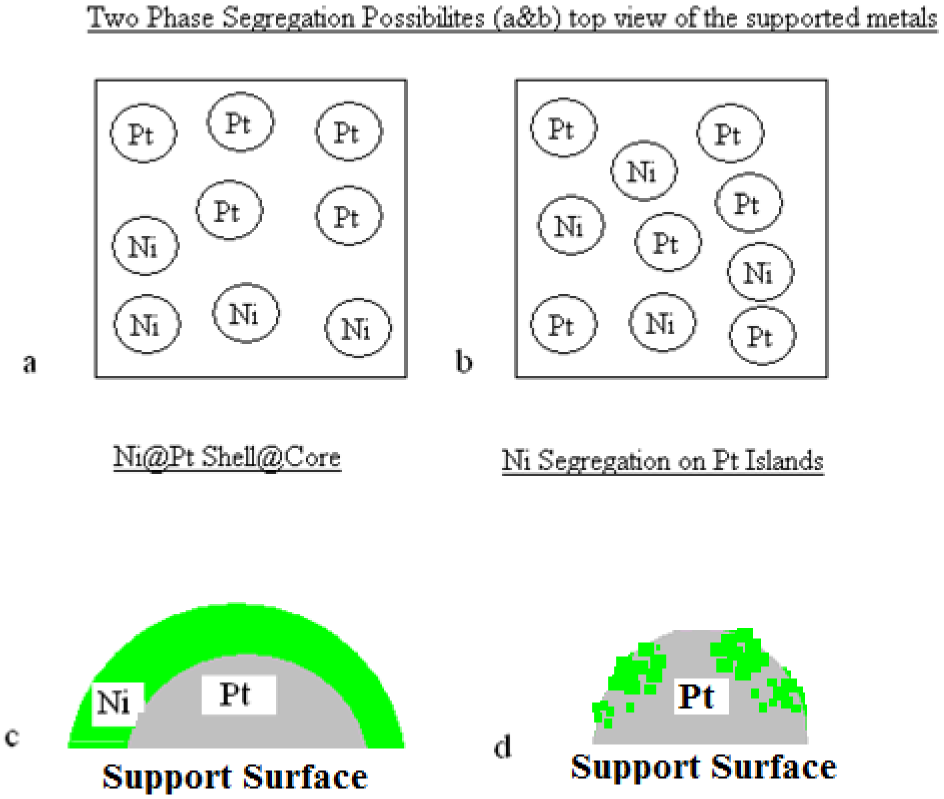

Figure 4.33: The Figure shows the possible structures of the prepared bimetallic PtNi composites supported by CA for the samples with Pt deposition followed by Ni incorporation.

This proposed structure is in harmony with the possible, idealized structures of the bimetallic compounds given in the literature [75]. (See Figure 4.34., the second configuration from the left: Partially alloyed with Ni atoms segregating on Pt islands)

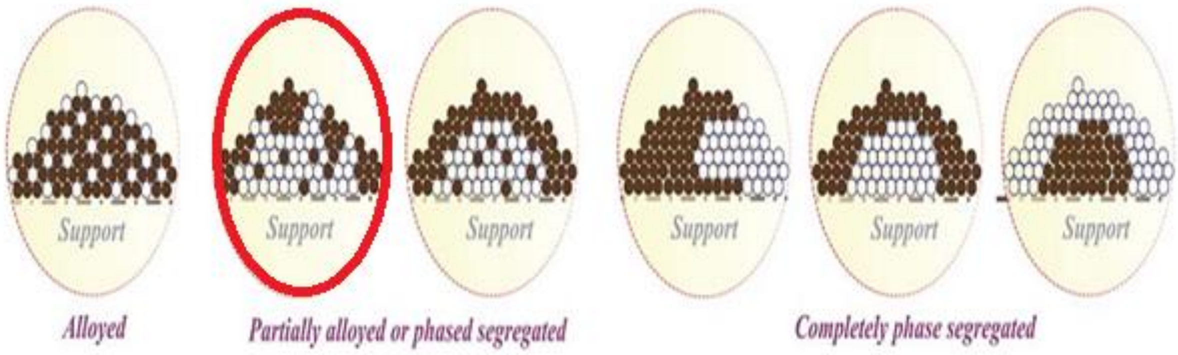

Figure 4.34: Idealized illustrations of the supported bimetallic nanoparticles which are alloyed, partially alloyed/partially phase-segregated, or completely phase-segregated, *taken from* [75]

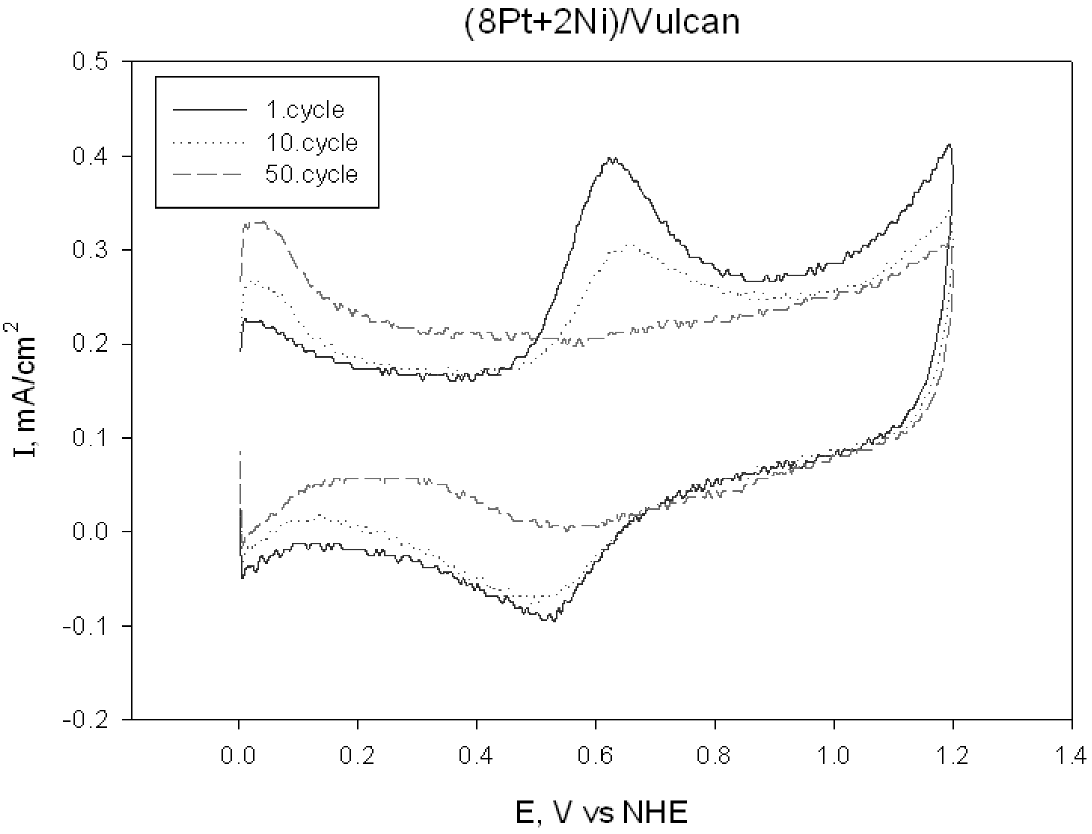

Figure 4.35: CV curves (8%Pt + 2%Ni)/Vulcan XC 72R in 0.1MHClO$_4$ at a sweep rate of 50mV/s.

Similar CV results were obtained for (8%Pt + 2%Ni)/Vulcan XC 72R catalyst on Figure 4.35. Almost, no ESA value was detected for the first cycle, on the other hand, the increasing number of the cycles resulted in a higher ESA value. Again, this may be an indication of the core-shell structure. However, unlike to the catalysts prepared on CA support, the catalysts on Vulcan XC 72R were prepared at higher reduction temperatures. (See Table 4.1) The higher temperatures might have forced the deposited platinum and nickel metals to interact further to form a nanoalloy with a certain degree of alloying. When the 'symmetric peaks' on the corresponding XRD spectra together with the 'shifts' of the expected peak positions towards higher 2Θ angles for bimetallic nanocatalysts is considered, one may suggest that (8%Pt + 2%Ni)/Vulcan XC 72R catalyst is a supported bimetallic nanoalloy. At this stage, the shift in XRD spectra was used in Vegard's Law to find the composition of Ni in the PtNi nanoalloy, according to the following formulas. Pt composition of 0.98 as compared to Ni composition of 0.02 was found which was so small and which was caused by the small shift! However, the corresponding EDX results suggest a Pt loading of ~0.55, at atomic base. Therefore, the possible structure of the Vulcan XC 72R supported bimetallic PtNi nanocatalysts is similar with those supported by CA and idealized illustration is provided in Figure 4.34., the second configuration from the left: Partially alloyed with Ni atoms segregating on Pt islands.

Pt_XNi_{1-X}

$$a_{alloy} = X \cdot a_{Pt} + (1-X) \cdot a_{Ni}$$

$$a = \lambda/(2 \cdot \sin\Theta) \cdot (h^2+k^2+l^2)^{1/2}$$

where X is the composition, a is the lattice constant, λ is the wavelength of the beam, h-k-l are the Miller indices….

The techniques used in this study do not enable us to make a crystal clear judgment on the definite structure of the bimetallic nanocatalysts supported by Vulcan XC 72R. In addition to the characterization results presented here, a better conclusion on the structure of Vulcan XC 72R supported nanocatalysts could be derived from the lattice spacing of the deposited nanoparticles (HRTEM). If nanoalloys were formed with a certain degree of alloying, then a lattice spacing value would be in the range between the values belonging to pure Pt and pure Ni. The lattice spacing values of supported bimetallic nanocatalysts can be revealed by closer TEM analysis.

As for the sharp peak appearing at ~0.6V in the cathodic region of the CV of (8%Pt + 2%Ni)/Vulcan XC 72R catalyst in Figure 4.35, the investigations in the literature reveal that it belongs to the surface oxide formations caused by hydroquinone-quinone (HQ-Q) redox couple [64, 76].

$$C=O + e^{-} + H^{+} \leftrightarrow C\text{-}OH$$

The hydrodynamic voltammograms of the Vulcan XC 72R supported catalyst is provided in Figure 4.36. Similar to the results obtained from CA supported catalysts, the limiting current increases with the increasing revolution speed since the increase in the revolution speed hinders the diffusion of the oxygen through the surface of an electrode. Up to ~0.3V, the diffusion limitations are observed to be more dominant. After 0.3V, the kinetic limitations are found to be more dominant as compared to the diffusion limitations.

In contrast to the Koutecky-Levich plots obtained from ORR on CA supported catalysts, ORR on (8%Pt + 2%Ni)/Vulcan XC 72R is found to produce the final product of water based on the total number of the electrons transferred during the overall ORR which is calculated to be ~4.

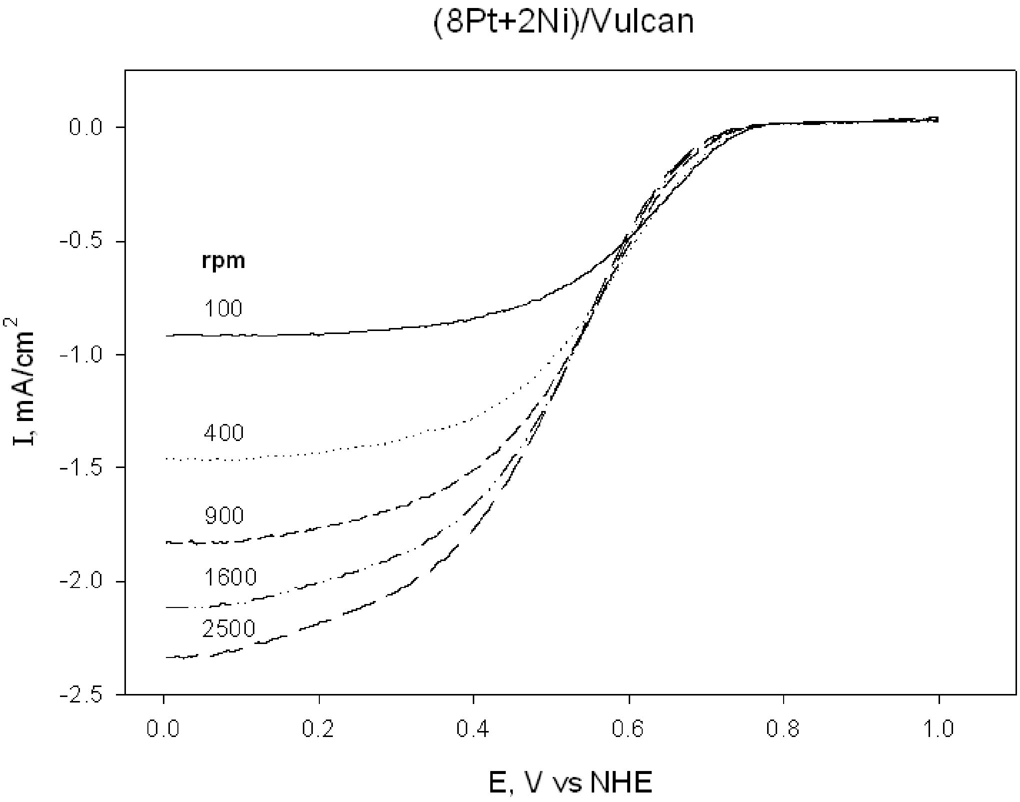

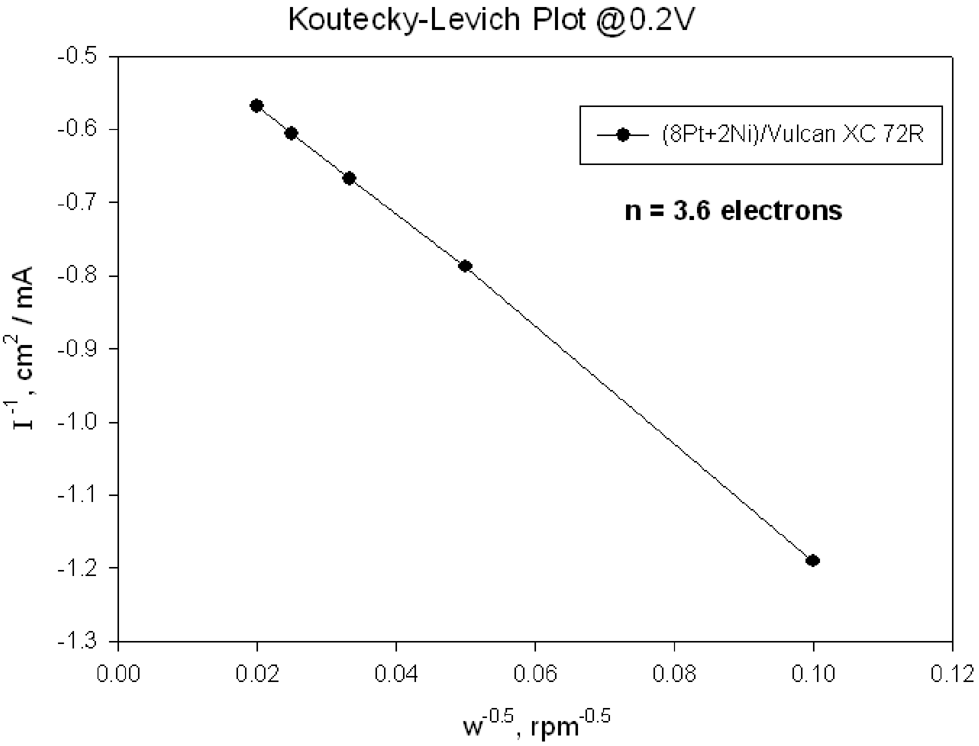

Figure 4.36: Hydrodynamic voltammograms of positive scans (top) and corresponding Koutecky-Levich plot (bottom) of (8%Pt + 2%Ni)/Vulcan XC 72R for O_2 reduction in O_2 saturated 0.1 M $HClO_4$

Alloying / coupling platinum nanoparticles supported on Vulcan XC 72R with a narrow particle size distribution and uniform chemical composition is important from the material science engineering point regarding the capability of our technique in utilizing the preparation of the supported bimetallic nanoparticles. However, it is also essential to check for any improvements in the catalytic activity achieved by the addition of the second metal, the promoter. The Figure 4.37 shows that limiting current values obtained from bimetallic catalysts with 2%Ni addition is higher by ~20%. After 0.4V, the ORR activity in the mixed diffusion-kinetic control region is independent of the second metal addition. Recalling that the ORR measurement were done after 50 HOR cycles, and that the data presented on Figure 4.37 is for 2500 rpm which was collected after the measurements taken at 100, 400, 900, and 1600 rpm, the dissolution of previously deposited nickel into the electrolyte is possible, too.

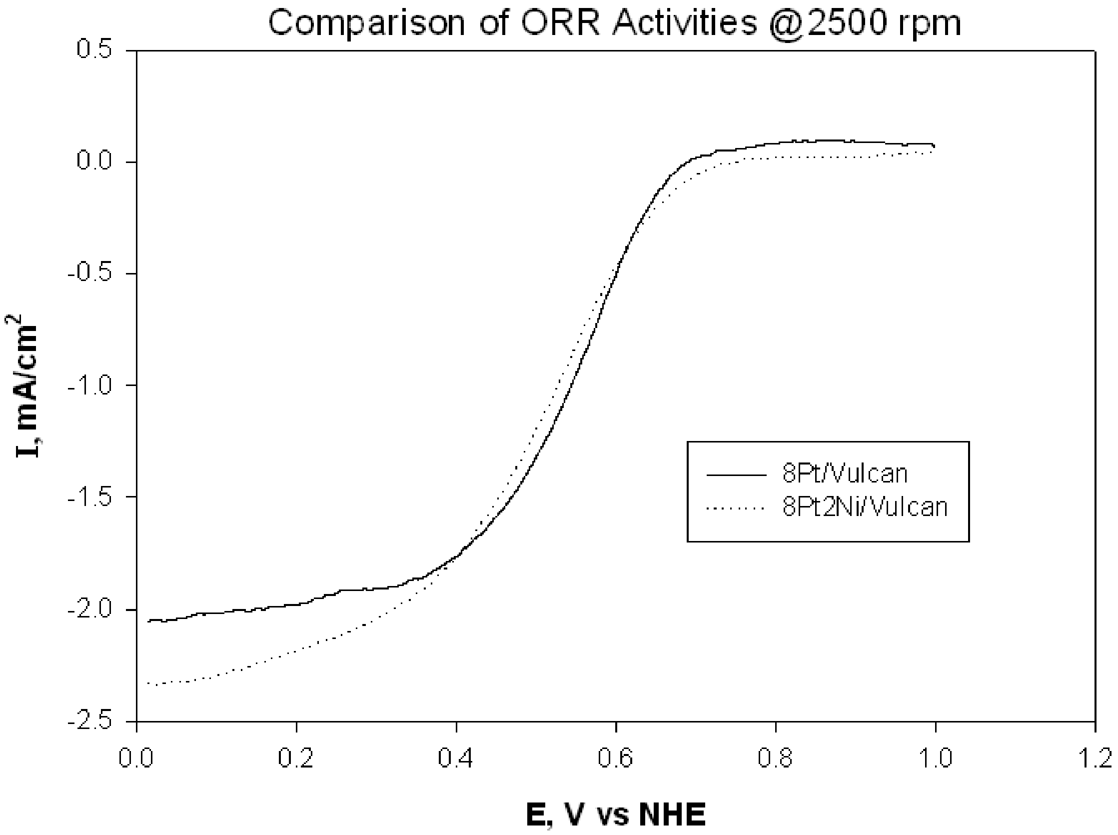

Figure 4.37: The figure comparatively shows the hydrodynamic voltammograms of positive scans of (8%Pt)/Vulcan XC 72R, and (8%Pt+2%Ni)/Vulcan XC 72R for O_2 reduction in O_2 saturated 0.1 M $HClO_4$.

5. CONCLUSIONS

Supported monometallic Ni and bimetallic PtNi nanocatalysts with different deposition sequences were prepared on γ-alumina, Vulcan XC72R and CA by SCD. It was found that Ni nanoparticle formation does not occur away from the previously deposited Pt islands which would results in a phase separation. Instead, Pt and Ni metals interacts with each other to form spherical bimetallic nanoparticles having homogeneous chemical compositions. However, Ni agglomerates were observed when Ni deposition was achieved prior to Pt deposition. This suggests that pre-existing Pt inhibits the Ni phase separation and agglomerate formation.

Activity tests were also performed. Higher activities were observed for bimetallic PtNi as compared to the monometallic Pt. As for the effect of impregnation sequence, two types of bimetallic PtNi nanocatalysts were prepared. One with Ni deposition and followed by the Pt addition and the other one with Pt deposition first and followed by Ni incorporation. It was found that the latter exhibits a higher electrochemical activity.

As compared to the ones in literature, high current densities with quite low amount of metal deposition were obtained indicating high utilization of the metal.

Regarding the definite structure of the extremely small synthesized nanoparticles, the characterization techniques in this study are not enough to make a crystal clear judgment for supported bimetallic PtNi nanocatalysts with homogeneous chemical compositions and with Pt deposition first followed by Ni incorporation. It is possible that nanoalloys are formed, or alternatively a structure that is partially alloyed with Ni atoms segregating on previously deposited Pt islands is possible. When combined with activity test results for both PtNi nanocatalysts with different deposition sequences, proposed structure is partially alloyed with Ni atoms growing on Pt islands for PtNi nanocatalysts with Pt deposition first and followed by Ni incorporation.

REFERENCES

1. Erkey, C., *Preparation of metallic supported nanoparticles and films using supercritical fluid deposition.* Journal of Supercritical Fluids, 2009. **47**(3): p. 517-522.
2. Du, H.D., et al., *Carbon aerogel supported Pt-Ru catalysts for using as the anode of direct methanol fuel cells.* Carbon, 2007. **45**(2): p. 429-435.
3. Rolison, D.R., *Catalytic nanoarchitectures - The importance of nothing and the unimportance of periodicity.* Science, 2003. **299**(5613): p. 1698-1701.
4. Park, G.G., et al., *Pore size effect of the DMFC catalyst supported on porous materials.* International Journal of Hydrogen Energy, 2003. **28**(6): p. 645-650.
5. Haji, S., et al., *Hydrodesulfurization of model diesel using Pt/Al2O3 catalysts prepared by supercritical deposition.* Catalysis Today, 2005. **99**(3-4): p. 365-373.
6. Seo, J.G., M.H. Youn, and I.K. Song, *Hydrogen production by steam reforming of liquefied natural gas (LNG) over nickel catalyst supported on mesoporous alumina prepared by a non-ionic surfactant-templating method.* International Journal of Hydrogen Energy, 2009. **34**(4): p. 1809-1817.
7. Mohanty, S., D. Kunzru, and D.N. Saraf, *Hydrocracking: a review.* Fuel, 1990. **69**(12): p. 1467-1473.
8. Huang, F., et al., *A new synthetic procedure for ordered mesoporous γ-alumina with a large surface area.* Scripta Materialia, 2010. **63**(3): p. 339-342.
9. Pekala, R.W., et al., *Aerogels Derived from Multifunctional Organic Monomers.* Journal of Non-Crystalline Solids, 1992. **145**(1-3): p. 90-98.
10. Krumpelt, M., R. Kumar, and K.M. Myles, *Fundamentals of Fuel-Cell System Integration.* Journal of Power Sources, 1994. **49**(1-3): p. 37-51.
11. Dicks, A.L., *The role of carbon in fuel cells.* Journal of Power Sources, 2006. **156**(2): p. 128-141.
12. Auer, E., et al., *Carbons as supports for industrial precious metal catalysts.* Applied Catalysis A: General, 1998. **173**(2): p. 259-271.
13. Taylor, A.D., et al., *Fuel cell performance and characterization of 1-D carbon-supported platinum nanocomposites synthesized in supercritical fluids.* Journal of Catalysis, 2008. **259**(1): p. 5-16.
14. Lin, Y., et al., *PtRu/Carbon Nanotube Nanocomposite Synthesized in Supercritical Fluid: A Novel Electrocatalyst for Direct Methanol Fuel Cells.* Langmuir, 2005. **21**(24): p. 11474-11479.
15. Yen, C.H., et al., *Chemical fluid deposition of pt-based bimetallic nanoparticles on multiwalled carbon nanotubes for direct methanol fuel cell application.* Energy & Fuels, 2007. **21**(4): p. 2268-2271.
16. Zhang, J., et al., *Preparation and characterization of Pt/C catalysts for PEMFC cathode: effect of different reduction methods.* Reaction Kinetics and Catalysis Letters, 2004. **83**(2): p. 229-236.
17. Colmati, F., et al., *Carbon monoxide oxidation on Pt-Ru electrocatalysts supported on high surface area carbon.* Journal of the Brazilian Chemical Society, 2002. **13**(4): p. 474-482.
18. King, W.D., et al., *Pt-Ru and Pt-Ru-P/carbon nanocomposites: Synthesis, characterization, and unexpected performance as direct methanol fuel cell (DMFC) anode catalysts.* Journal of Physical Chemistry B, 2003. **107**(23): p. 5467-5474.
19. Song, C., *Fuel processing for low-temperature and high-temperature fuel cells: Challenges, and opportunities for sustainable development in the 21st century.* Catalysis Today, 2002. **77**(1-2): p. 17-49.

20. Lin, L., et al., *Research and development of catalytic processes for petroleum and natural gas conversions in the Dalian Institute of Chemical Physics.* Catalysis Today, 1999. **51**(1): p. 59-72.
21. Guillaume, D., et al., *Relation Between Acid and Catalytic Properties of Chlorinated Gamma-Alumina. a 31p Mas Nmr and Ftir Investigation* Oil & Gas Science and Technology - Rev. IFP, 1999. **54**(4): p. 537-545.
22. Ali, M.A., T. Tatsumi, and T. Masuda, *Development of heavy oil hydrocracking catalysts using amorphous silica-alumina and zeolites as catalyst supports.* Applied Catalysis A: General, 2002. **233**(1–2): p. 77-90.
23. Karthikeyan, D., et al., *Hydroisomerization of n-Octane over Bifunctional Ni−Pd/HY Zeolite Catalysts.* Industrial & Engineering Chemistry Research, 2008. **47**(17): p. 6538-6546.
24. Gutberlet, L.C., R.J. Bertolacini, and S.G. Kukes, *Design of a nickel-tungsten hydrocracking catalyst.* Energy & Fuels, 1994. **8**(1): p. 227-233.
25. Hassan, A., et al., *A comparison between β- and USY-zeolite-based hydrocracking catalysts.* Applied Catalysis A: General, 2001. **220**(1–2): p. 59-68.
26. Blomsma, E., J.A. Martens, and P.A. Jacobs, *Isomerization and Hydrocracking of Heptane over Bimetallic Bifunctional PtPd/H-Beta and PtPd/USY Zeolite Catalysts.* Journal of Catalysis, 1997. **165**(2): p. 241-248.
27. Sie, S.T., *Miniaturization of hydroprocessing catalyst testing systems: Theory and practice.* AIChE Journal, 1996. **42**(12): p. 3498-3507.
28. Chu, C.F. and K.M. Ng, *Flow in packed tubes with a small tube to particle diameter ratio.* AIChE Journal, 1989. **35**(1): p. 148-158.
29. Kistler, S.S., *Coherent Expanded Aerogels and Jellies.* Nature, 1931. **127**(3211): p. 741.
30. Kistler, S.S., *Coherent Expanded-Aerogels.* The Journal of Physical Chemistry, 1931. **36**(1): p. 52-64.
31. Pekala, R.W., *Organic Aerogels from the Polycondensation of Resorcinol with Formaldehyde.* Journal of Materials Science, 1989. **24**(9): p. 3221-3227.
32. Pajonk, G.M., *Aerogel catalysts.* Applied Catalysis, 1991. **72**(2): p. 217-266.
33. Wang, J., et al., *Electrical Transport Properties of Carbon Aerogels.* Journal of Porous Materials, 2001. **8**(2): p. 167-170.
34. Petričević, R., M. Glora, and J. Fricke, *Planar fibre reinforced carbon aerogels for application in PEM fuel cells.* Carbon, 2001. **39**(6): p. 857-867.
35. Moreno-Castilla, C. and F.J. Maldonado-Hódar, *Carbon aerogels for catalysis applications: An overview.* Carbon, 2005. **43**(3): p. 455-465.
36. Smirnova, A., et al., *Novel carbon aerogel-supported catalysts for PEM fuel cell application.* International Journal of Hydrogen Energy, 2005. **30**(2): p. 149-158.
37. Ozkan, U.S., *Design of Heterogeneous Catalysts: New Approaches based on Synthesis, Characterization and Modeling*, 2009, WILEY-VCH: Weinheim. p. 195-196.
38. Mazurek, M., et al., *Binary mixtures of carbon supported Pt and Ru catalysts for PEM fuel cells.* Fuel Cells, 2006. **6**(3-4): p. 208-213.
39. Benfield, R.E., *Mean Coordination Numbers and the Nonmetal Metal Transition in Clusters.* Journal of the Chemical Society-Faraday Transactions, 1992. **88**(8): p. 1107-1110.
40. Lamy, C., et al., *Recent advances in the development of direct alcohol fuel cells (DAFC).* Journal of Power Sources, 2002. **105**(2): p. 283-296.
41. Sao-Joao, S., et al., *Structure and deformations of Pd-Ni core-shell nanoparticles.* Journal of Physical Chemistry B, 2005. **109**(1): p. 342-347.
42. Wang, G.F., et al., *Monte Carlo simulations of segregation in Pt-Ni catalyst nanoparticles.* Journal of Chemical Physics, 2005. **122**(2): p. -.
43. Waszczuk, P., et al., *Methanol Electrooxidation on Platinum/Ruthenium Nanoparticle Catalysts.* Journal of Catalysis, 2001. **203**(1): p. 1-6.
44. Duran Pachon, L., et al., *Palladium-coated nickel nanoclusters: new Hiyama cross-coupling catalysts.* Physical Chemistry Chemical Physics, 2006. **8**(1): p. 151-157.

45. Min, M.K., et al., *Particle size and alloying effects of Pt-based alloy catalysts for fuel cell applications.* Electrochimica Acta, 2000. **45**(25-26): p. 4211-4217.
46. Chan, K.Y., et al., *Supported mixed metal nanoparticles as electrocatalysts in low temperature fuel cells.* Journal of Materials Chemistry, 2004. **14**(4): p. 505-516.
47. Zhang, Y. and C. Erkey, *Preparation of supported metallic nanoparticles using supercritical fluids: A review.* Journal of Supercritical Fluids, 2006. **38**(2): p. 252-267.
48. Leitner, W., *Supercritical carbon dioxide as a green reaction medium for catalysis.* Accounts of Chemical Research, 2002. **35**(9): p. 746-756.
49. Bayrakceken, A., et al., *PtPd/BP2000 electrocatalysts prepared by sequential supercritical carbon dioxide deposition.* International Journal of Hydrogen Energy, 2010. **35**(21): p. 11669-11680.
50. Saquing, C.D., et al., *Investigation of the supercritical deposition of platinum nanoparticles into carbon aerogels.* Microporous and Mesoporous Materials, 2005. **80**(1-3): p. 11-23.
51. Bayrakceken, A., et al., *Vulcan-Supported Pt Electrocatalysts for PEMFCs Prepared using Supercritical Carbon Dioxide Deposition.* Chemical Engineering Communications, 2009. **196**(1-2): p. 194-203.
52. Dhepe, P.L., A. Fukuoka, and M. Ichikawa, *Novel fabrication and catalysis of nano-structured Rh and RhPt alloy particles occluded in ordered mesoporous silica templates using supercritical carbon dioxide.* Physical Chemistry Chemical Physics, 2003. **5**(24): p. 5565-5573.
53. Wakayama, H. and Y. Fukushima, *Supercritical CO2 for making nanoscale materials.* Industrial & Engineering Chemistry Research, 2006. **45**(10): p. 3328-3331.
54. Cangul, B., et al., *Preparation of carbon black supported Pd, Pt and Pd-Pt nanoparticles using supercritical CO2 deposition.* Journal of Supercritical Fluids, 2009. **50**(1): p. 82-90.
55. Libuda, J. and H.J. Freund, *Molecular beam experiments on model catalysts.* Surface Science Reports, 2005. **57**(7-8): p. 157-298.
56. Luo, J., et al., *Phase properties of carbon-supported gold-platinum nanoparticles with different bimetallic compositions.* Chemistry of Materials, 2005. **17**(12): p. 3086-3091.
57. Nashner, M.S., et al., *Structural Characterization of Carbon-Supported Platinum−Ruthenium Nanoparticles from the Molecular Cluster Precursor PtRu5C(CO)16.* Journal of the American Chemical Society, 1997. **119**(33): p. 7760-7771.
58. I. Chorkendorff, J.W.N., *Concepts of Modern Catalysis and Kinetics*, 2003, WILEY-VCH: Weinheim. p. 129.
59. Niemantsverdiret, J.W., *Spectroscopy in Catalysis, An Introduction*2000, Weinheim: Wiley-VCH.
60. Klug, H.P.A., L. E. , in *X-ray diffraction procedures for polycrystalline and amorphous materials, second ed.*1974: New York. p. 562.
61. Yang, H., et al., *Structure and electrocatalytic activity of carbon-supported Pt-Ni alloy nanoparticles toward the oxygen reduction reaction.* Journal of Physical Chemistry B, 2004. **108**(30): p. 11024-11034.
62. Bozbag, S.E., et al., *Adsorption of Pt(cod)me2 onto organic aerogels from supercritical solutions for the synthesis of supported platinum nanoparticles.* The Journal of Supercritical Fluids, 2011. **56**(1): p. 105-113.
63. Chen, Y., et al., *Solvent-free aerobic oxidation of benzyl alcohol over Pd monometallic and Au–Pd bimetallic catalysts supported on SBA-16 mesoporous molecular sieves.* Applied Catalysis A: General, 2010. **380**(1–2): p. 55-65.
64. Bayrakçeken, A., et al., *PtPd/BP2000 electrocatalysts prepared by sequential supercritical carbon dioxide deposition.* International Journal of Hydrogen Energy, 2010. **35**(21): p. 11669-11680.
65. Allen J. Bard, L.R.F., *Electrochemical Methods: Fundamentals and Applications*. 2 nd ed2001: John Wiley & Sons Inc.
66. Zhang, Y., *Preparation of supported ruthenium and platinum nanoparticles by supercritical incorporation methods* 2006, University of Connecticut p. 152.

67. Paulus, U.A., et al., *Oxygen reduction on carbon-supported Pt-Ni and Pt-Co alloy catalysts.* Journal of Physical Chemistry B, 2002. **106**(16): p. 4181-4191.
68. Suárez-Alcántara, K., et al., *RuxCrySez electrocatalyst for oxygen reduction in a polymer electrolyte membrane fuel cell.* Journal of Power Sources, 2006. **157**(1): p. 114-120.
69. Paulus, U.A., et al., *Oxygen Reduction on Carbon-Supported Pt−Ni and Pt−Co Alloy Catalysts.* The Journal of Physical Chemistry B, 2002. **106**(16): p. 4181-4191.
70. Marković, N.M. and P.N. Ross Jr, *Surface science studies of model fuel cell electrocatalysts.* Surface Science Reports, 2002. **45**(4–6): p. 117-229.
71. Yu, L., et al., *Oxygen reduction reaction mechanism on nitrogen-doped graphene: A density functional theory study.* Journal of Catalysis, 2011. **282**(1): p. 183-190.
72. Stamenkovic, V.R., et al., *Improved oxygen reduction activity on Pt3Ni(111) via increased surface site availability.* Science, 2007. **315**(5811): p. 493-497.
73. Zignani, S.C., E. Antolini, and E.R. Gonzalez, *Stability of Pt-Ni/C (1:1) and Pt/C electrocatalysts as cathode materials for polymer electrolyte fuel cells: Effect of ageing tests.* Journal of Power Sources, 2009. **191**(2): p. 344-350.
74. Yang, H., et al., *Methanol tolerant oxygen reduction on carbon-supported Pt-Ni alloy nanoparticles.* Journal of Electroanalytical Chemistry, 2005. **576**(2): p. 305-313.
75. Wanjala, B.N., et al., *Gold-platinum nanoparticles: alloying and phase segregation.* Journal of Materials Chemistry, 2011. **21**(12): p. 4012-4020.
76. Wang, J.J., et al., *Effect of carbon black support corrosion on the durability of Pt/C catalyst.* Journal of Power Sources, 2007. **171**(2): p. 331-339.